

UNIVERSITY OF FRIBOURG (SWITZERLAND))

# **Sustaining cryosphere-fed irrigation networks with ice reservoirs**

by

Suryanarayanan Balasubramanian

A thesis submitted in partial fulfillment for the  
degree of Doctor of Philosophy

in the  
Department of Geosciences

June 2022

# **Declaration of Authorship**

I, Suryanarayanan Balasubramanian, declare that this thesis titled, ‘Ice Reservoirs’ and the work presented in it are my own. I confirm that:

- This work was done wholly or mainly while in candidature for a research degree at this University.
- Where any part of this thesis has previously been submitted for a degree or any other qualification at this University or any other institution, this has been clearly stated.
- Where I have consulted the published work of others, this is always clearly attributed.
- Where I have quoted from the work of others, the source is always given. With the exception of such quotations, this thesis is entirely my own work.
- I have acknowledged all main sources of help.
- Where the thesis is based on work done by myself jointly with others, I have made clear exactly what was done by others and what I have contributed myself.

Signed:

---

Date:

---

*“Write a funny quote here.”*

If the quote is taken from someone, their name goes here

UNIVERSITY OF FRIBOURG (SWITZERLAND))

*Abstract*

Faculty Name  
Department of Geosciences  
Doctor of Philosophy

by Suryanarayanan Balasubramanian

The Thesis Abstract is written here (and usually kept to just this page). The page is kept centered vertically so can expand into the blank space above the title too...

# Contents

<b>Declaration of Authorship</b>	<b>i</b>
<b>Abstract</b>	<b>iii</b>
<b>1 Ice Reservoirs</b>	<b>1</b>
1.1 Introduction . . . . .	1
1.2 Nomenclature and Classification . . . . .	3
1.3 Objectives . . . . .	4
1.4 Structure . . . . .	4
<b>2 Religion of ice reservoirs</b>	<b>5</b>
2.1 An old history . . . . .	5
2.2 The marriages of glaciers . . . . .	5
2.3 From folklore to science . . . . .	7
<b>3 Science of ice reservoirs</b>	<b>8</b>
3.1 Study sites and data . . . . .	8
3.1.1 Study sites . . . . .	8
3.1.2 Meteorological data . . . . .	10
3.1.3 Fountain observations . . . . .	10
3.1.4 Drone flights . . . . .	11
3.2 AIR Model . . . . .	11
3.2.1 Surface area calculation . . . . .	11
3.2.2 Energy balance calculation . . . . .	13
3.2.2.1 Net Shortwave Radiation $q_{SW}$ . . . . .	14
3.2.2.2 Net Longwave Radiation $q_{LW}$ . . . . .	15
3.2.2.3 Turbulent fluxes . . . . .	16
3.2.2.4 Fountain discharge heat flux $q_F$ . . . . .	17
3.2.2.5 Rain heat flux $q_R$ . . . . .	17
3.2.2.6 Bulk Icestupa heat flux $q_G$ . . . . .	18
3.2.2.7 Phase changes . . . . .	18
3.2.3 Mass balance calculation . . . . .	19
3.3 Model extensions . . . . .	21
3.3.1 Discharge rate scheduler . . . . .	21
3.3.2 Location classifier . . . . .	22

3.3.2.1	Model configuration . . . . .	23
3.3.2.2	Advantages . . . . .	23
3.4	Suggestions . . . . .	24
3.4.1	Model development . . . . .	24
3.4.2	Further Data acquisition . . . . .	24
3.4.2.1	Meltwater quantities . . . . .	24
3.4.2.2	Fountain characteristics . . . . .	24
3.4.2.3	Drone flight analysis . . . . .	24
3.4.3	Improvement of model algorithm . . . . .	24
3.4.3.1	Initialisation of model . . . . .	24
3.4.3.2	Better model parametrisations . . . . .	24
<b>4</b>	<b>Habitat of ice reservoirs</b>	<b>25</b>
4.1	Requirements for AIR construction . . . . .	25
4.1.1	Checklist to identify AIR construction regions . . . . .	26
4.1.2	Metrics to rank sites within the same region . . . . .	26
<b>5</b>	<b>Technology of ice reservoirs</b>	<b>28</b>
5.1	Ice terraces . . . . .	28
5.1.1	Construction strategy . . . . .	28
5.1.2	Application . . . . .	29
5.1.3	Drawbacks . . . . .	30
5.2	Ice stupas . . . . .	30
5.2.1	Construction strategy . . . . .	31
5.2.2	Application . . . . .	32
5.2.3	Drawbacks . . . . .	32
5.3	Improvement of construction strategies through weather-sensitive automation systems . . . . .	32
<b>6</b>	<b>Heritage of ice reservoirs</b>	<b>33</b>
6.1	Summary . . . . .	33
6.2	Conclusions . . . . .	34
6.3	Discussion . . . . .	35
6.4	Recommendations . . . . .	35
6.5	Suggestions for future research . . . . .	35
6.6	Final thoughts . . . . .	35
<b>Paper I</b>		<b>36</b>
<b>Paper II</b>		<b>43</b>
<b>Paper III</b>		<b>61</b>
<b>Symbols</b>		<b>84</b>
<b>List of Figures</b>		<b>85</b>

<b>List of Tables</b>	<b>86</b>
<b>Abbreviations</b>	<b>87</b>
<b>Physical Constants</b>	<b>88</b>
<b>Acknowledgements</b>	<b>89</b>
 <b>Bibliography</b>	 <b>90</b>

*For/Dedicated to/To my...*

# Chapter 1

## Ice Reservoirs

### 1.1 Introduction

Cryosphere-fed irrigation networks in arid mountain regions are completely dependent on timely availability of meltwater from glaciers, snow and permafrost [2–4]. With the accelerated decline of glaciers due to climate change [1], these regions are experiencing water scarcity particularly during the spring season [5, 6] (see Fig. 1.1). This seasonal water scarcity makes it essential to provide supplementary irrigation in order to sustain agricultural output and take advantage of the complete growing season [1, 7].

To cope with this recurrent water scarcity, villagers in the region of Ladakh have developed two types of artificial ice reservoirs (AIRs): ice stupas and ice terraces. All these types of ice reservoirs capture water in the autumn and winter, allowing it to freeze, and hold it until spring, when it melts and flows down to fields [8–11]. In this way, they retain a previously unused portion of the annual flow and facilitate its use to supplement the decreased flow in the following spring (see Fig. 1.1). This study focuses on the form of AIRs locally called as ice stupas.

Over the past decade, several ice stupas have been built to supplement irrigation water supply of mountain villages in India [12–14], Kyrgyzstan [15] and Chile [16]. Despite this widespread adoption, only a few publications examine the role of AIRs in the water resource management of these regions. None of these publications study AIRs outside Ladakh. Moreover, the published quantifications of the water storage capacity of AIRs just in Ladakh also vary widely between these studies [5, 17].

Quantifying the water storage capacity of AIRs is not straightforward since the formative processes of AIRs are complex. These processes are controlled by local topography, meteorology and construction strategies used. However, methodologies used to quantify

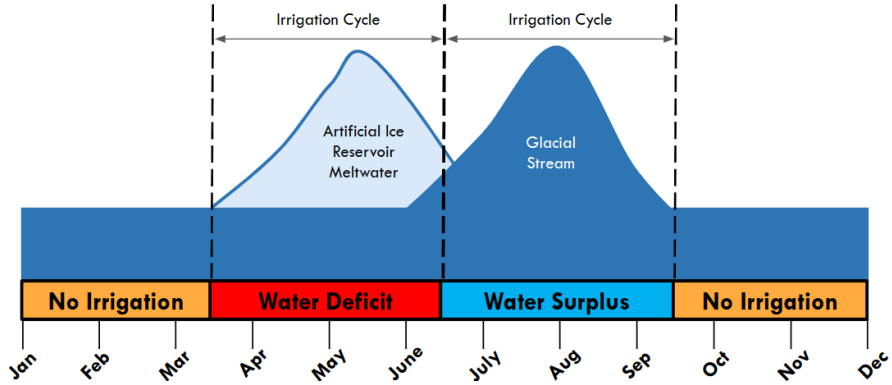


FIGURE 1.1: Seasonal variation in the availability of irrigation water. The graph highlights the crucial role of AIRs in bridging the critical gap in water availability.

Adapted from: [1]

meteorological influences on glaciers may also be applicable on these ice reservoirs since their surface processes are similar. But due to their limited size, and comparatively more variable surface area, this assessment requires a modelling approach which is optimally constrained with comprehensive data from in-situ field measurements.

A spirit of improvisation guides the construction strategies of AIRs. This has resulted in ice reservoirs exhibiting significant volume variations despite experiencing similar meteorological conditions. For example, ice terraces have attained volumes upto 30 times larger than ice stupas built in Ladakh, India [11]. However, the processes driving these differences can only be resolved if the complete methodology of the construction strategy used is available.

This thesis fulfills both of these requirements as it provides a new set of AIR-specific volume and area measurements from drone flights along with meteorological data during the construction period. All these datasets were produced through construction strategies using fountain systems that are quantified via in-situ observations of the fountain characteristics and discharge rate measurements. In a first step, this thesis attempts to formulate a one-dimensional AIR model in order to calibrate and validate it with the AIR datasets. In a second step, it attempts to use this model as a tool to propose a construction strategy designed to produce AIRs efficiently and effortlessly. While this thesis reviews published AIR research and presents a comprehensive quantitative study of their water storage potential, we acknowledge that substantial additional knowledge is held by farming communities building these structures since mid-1800s.

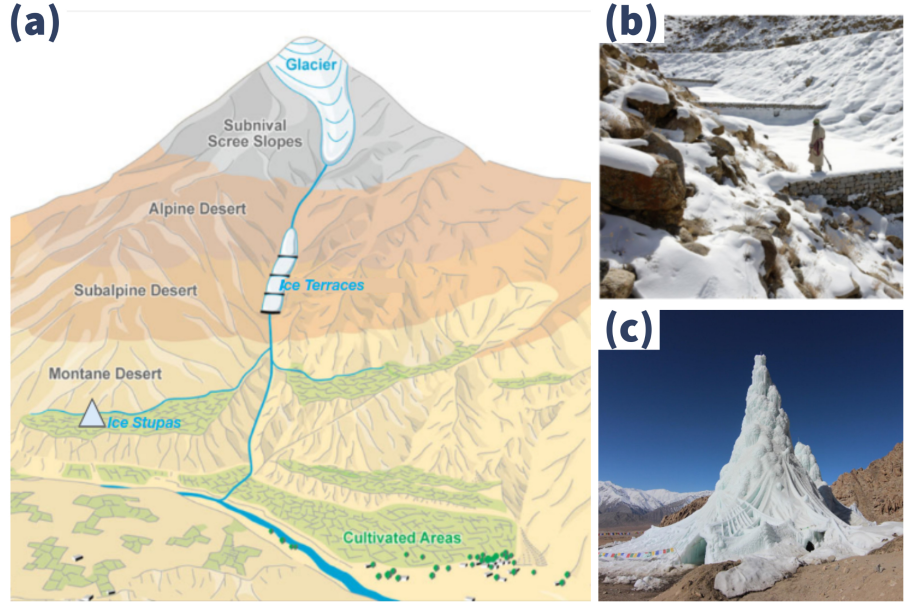


FIGURE 1.2: (a) Schematic overview of the position of artificial ice reservoirs. These constructions are located at altitudes between the glaciers and the irrigation networks in the cultivated areas. (b) Ice terraces at 3900 m, located above the village of Nang, Ladakh. The cascade is composed of a series of loose masonry walls ranging in height from 2 to 3 m, which help freeze water for storage. (c) Ice stupas at 3600 m, located above the village of Phyang, Ladakh. They are made using fountain systems. Adapted from: [1]

## 1.2 Nomenclature and Classification

In spite of the popularity of the term "artificial glacier", we deliberately use the term "ice reservoir" since it conveys character and function of these structures more accurately [11]. Man-made ice structures typically have a lifetime in the order of months and a size million times smaller than typical glaciers. Therefore, any comparison between these ice structures can be misleading. Since glaciers are considered as natural ice reservoirs, we use the terminology artificial ice reservoirs (AIRs) to distinguish man-made ice structures described in this thesis.

A spirit of improvisation guides the construction strategy of AIRs making it difficult to classify them. However, it has been found that construction strategies using fountain systems form AIRs which tend towards a conical shape and those without form flat sheets of ice. Therefore, this thesis classifies all the AIRs produced based on whether or not they use fountain systems. AIRs using fountain systems are called "ice stupas" and those without are called "ice terraces" since this terminology denotes the resulting shape of the respective AIRs appropriately.

### 1.3 Objectives

The main objective of this thesis is to quantify the water storage potential of AIRs based on the construction site and fountain chosen.

An integrated study approach including field measurements and modelling is applied to answer the following research questions:

1. What is the influence of construction location and fountain characteristics on AIR volume evolution?
2. How can ice stupa fountain systems be engineered to reduce water loss and maintenance of AIRs?

An energy and mass balance model for artificial ice reservoirs was set up to answer the first research question (paper I and II). Since in-situ measurements were required to run this model, a measurement campaign was executed in Switzerland and India during the past 4 winters. These datasets provided the necessary input, calibration and validation data to model the evolution of AIRs and study their sensitivity to meteorological conditions and fountain characteristics (paper II).

Two weather-sensitive construction strategies were developed to answer the second research question. These construction strategies employed fountains whose discharge rate was regulated by automation system using the AIR model developed before. Their advantages over traditional construction strategy are quantified in paper III.

### 1.4 Structure

Chapter 1 introduces the motivation of this work and provides a summary of the state of knowledge about AIRs prior to this thesis. Chapter 2 describes the origins of this technology as a religious practice. Chapter 3 gives an overview about the study sites and introduces the different field techniques applied. The influence of the construction location through its meteorological and topographical conditions are presented in Chapter 4. The engineering design of AIR technologies are showcased in Chapter 5 along with suggestions for their improvement. Chapter 6 concludes the thesis with a synthesis and future outlook. Papers I, II and III are included in the Appendix.

## Chapter 2

# Religion of ice reservoirs

For centuries, in the Himalayan mountain ranges, local cultures have believed that glaciers are alive. And what's more, that certain glaciers can have different genders including male and female. These people 'breed' new glaciers by grafting together—or marrying—fragments of ice from male and female glaciers, then covering them with charcoal, wheat husks, cloths, or willow branches so they can reproduce in privacy. These glacierets transform into fully active glaciers that grow each year with additional snowfall. Those then serve as lasting reserves of water that farmers can use to irrigate their crops. Over the years, these practices have inspired other cultures, where people are creating their own artificial ice reservoirs (AIRs) and applying them to solve serious modern challenges around water supplies.

### 2.1 An old history

According to legend, when the people of Baltistan learnt of the Mongol army advancing towards them from the north in the early 13th century, they came up with an ingenious way to stop them. As the inhabited valleys were only accessible through narrow passes, they decided to block the entry way by building a glacier. This successfully prevented the Mongol invasion and, crucially, it also solved the locals' other big problem: water scarcity.

### 2.2 The marriages of glaciers

The people of Gilgit Baltistan believe that glaciers are living entities. That's why a combination of female and male ice was absolutely necessary. The male glacier – called

'po gang' locally – gives off little water and moves slowly, while a 'female glacier' – or 'mo gang' – is a growing glacier that gives off a lot of water.

The glaciers that people help to grow are the fruit of the sacred union between a mother glacier and a father glacier. They get married and have offspring. The selection of an appropriate site for this marriage is of utmost importance, and a suitable spot must fulfil a list of conditions. It should be located at an altitude of at least 4000 or 5000 metres above sea level; it should be on a gentle slope, where it should have minimal exposure to sunlight, thus a north-facing mountain side is preferable. For most of the expert glacier grafters, the presence of permafrost or ice on the site is another key requirement.

Once a suitable spot is selected, the expedition can be planned. The bride and the groom – the female and the male glacier, preferably from different villages – are chosen and the marriage can be planned. The glacier grafting usually takes place in November, when the local temperatures oscillate around zero. A 12-man party carries the pieces of female ice in woven baskets, another 12 men carry the male ice, the water drawn from the Indus river is carried traditionally in 12 gourd bottles, but sometimes clay pots or goatskins are also required, as well as charcoal and wheat husks or sawdust, which act as insulators for the ice. The last ingredient is salt, which, according to some glacier grafters, helps protect the new glacier from impurities. The bride and groom party walk from different sites and meet in a certain spot to climb together to the glacier growing site, but no greetings are exchanged, as the people involved in the ceremony must remain silent until the ice is deposited in its new home. They walk continuously without having a break, but if the distance is too much and rest is required, they do not put their loads on the ground, instead hanging the baskets on trees, or on walking sticks if nothing else is available. Each man has to carry around 15 to 25 kilograms of ice, walking in cold air, silently up the mountains, for a day or more. Once they reach the glacier growing site, they deposit their valuable loads. The ice lumps and water bottles are placed in between the boulders, or in a small cave, or sometimes in a specially dug pit, and covered with layers of salt, charcoal and sawdust. The silence is broken as religious leaders recite verses of the Quran and say prayers for the success of the glacier marriage and for protection from the djinns. Once the male and female glaciers are placed in their new home and covered, a man from the party of glacier grafters stands up and offers his life for the success of the process. His symbolic sacrifice is matched by the actual sacrifice of a goat – its meat is distributed to a charity, because prayers are more likely to be answered if accompanied by an act of charity. They will not visit the place for at least three years, so as not to disturb the glacier. It is said that a person who disturbs the glacier before its maturation will die. The celebrations continue in the village with traditional songs and prayers, alongside festive food and the joy of the accomplished mission.

### 2.3 From folklore to science

Myths, legends and superstitions are ways of knowing. But they need to be translated to the language of science. However, when it comes to past projects, there is only anecdotal evidence available.

According to Ingvar Tveiten, a researcher from Norway, the account of the glacier development process presented by a glacier grafter from Balghar bears a strong resemblance to the definition of the formation of rock glaciers. According to a description by a Balghar local: “First the ice slips down into the rocks where it grows roots. Then it starts to break the rocks bringing them up. Then the glacier comes forward. This has happened where they did the glacier growing.” Tveiten, who conducted field research in Baltistan, concludes that “glacier growing is typically performed [...] in a terrain that is conducive to the accumulation of snow by avalanching and snow slips. The presence of permafrost at these locations is likely to contribute to ice accumulating [...] Thus, glacier growing is conducted at locations which are already very prone to ice accumulation, and may explain why glacier growing is perceived to work.” Here it is, traditional knowledge translated into the language of science.

Even the choice of the glacier grafting site suggests that the technique was developed as a result of the local people’s deep understanding of local environmental processes. The view of glaciers as animate implies that humans can influence on the lives of glaciers, just as glaciers can influence on the lives of people.

# Chapter 3

## Science of ice reservoirs

This chapter provides the methodology used to estimate the ice volume evolution and water-use efficiency of AIRs. The equations governing the mass and energy balance of vertical AIRs (or Icestupas) is explained along with the associated datasets required for forcing, calibration and validation of this AIR model.

The influence of the chosen location and fountain used was quantified by feeding weather and fountain data to an energy balance model and validating the ice volume estimates produced with volume observations from drone flights. Therefore, weather observations and fountain characteristics were required to force the AIR model and ice volume observations were required to calibrate and validate the model.

### 3.1 Study sites and data

#### 3.1.1 Study sites

We chose two villages in the Swiss Alps and the Indian Himalayas called Guttannen and Gangles to collect the required datasets described above. These two locations exhibit drastically different ice volume evolution (see Fig. 4.1) owing to their latitude, longitude and altitude differences. The corresponding datasets were categorised based on the construction strategy used, prefix of the country and the suffix of the winter season. The construction strategies are distinguished based on whether they used weather-sensitive approaches to regulate water supply. Those that did were codenamed automated construction strategy whereas the rest were codenamed traditional construction strategy. In total, five AIRs were studied in these two locations across three winters (see Table).



FIGURE 3.1: The Swiss and Indian AIRs were 5 *m* and 13 *m* tall on January 9 and March 3, 2021 respectively. Picture credits: Daniel Buerki (left) and Thinles Norboo (right)

Only one was built in Gangles. The rest were built in Guttannen. All except one construction campaign used traditional construction strategies. Therefore, traditional AIRs are referred to without explicitly specifying their construction strategy henceforth.

The Guttannen site ( $46.66 N, 8.29E$ ) is situated in the Berne region, Switzerland and has an altitude of 1047 *m* a.s.l. In the winter (Oct-Apr), mean daily minimum and maximum air temperatures vary between -13 and 15 . Clear skies are rare, averaging around 7 days during winter. Daily winter precipitation can sometimes be as high as 100 *mm*. These values are based on 30 years of hourly historical weather data measurements [18]. Several AIRs were constructed by the Guttannen Bewegt Association, the University of Fribourg and the Lucerne University of Applied Sciences and Arts during the winters of 2020-22.

The Gangles site ( $34.22 N, 77.61E$ ) is located around 20 km north of Leh city in the Ladakh region, lying at 4025 *m* a.s.l.. The mean annual temperature is 5.6 , and the thermal range is characterized by high seasonal variation. During January, the coldest month, the mean temperature drops to -7.2 . During August, the warmest month, the mean temperature rises to 17.5 [19]. Because of the rain shadow effect of the Himalayan Range, the mean annual precipitation in Leh totals less than 100 *mm*, and there is high interannual variability. Whereas the average summer rainfall between July and September reaches 37.5 *mm*, the average winter precipitation between January and March amounts to 27.3 *mm* and falls almost entirely as snow. AIRs were constructed here as part of the Ice Stupa Competition by the Himalayan Institute of Alternatives, Ladakh (HIAL).

TABLE 3.1: Summary of the weather observations for AIRs built during the 2020-21 winter season. The expiry date refers to the date when all of the ice of the AIR completely disappeared and only the dome volume remains. The weather measurements are shown using their mean ( $\mu$ ) and standard deviation ( $\sigma$ ) during the study period as  $\mu \pm \sigma$ .

Name	Symbol	IN21	CH21	Units
Air temperature	$T_a$	$0 \pm 7$	$2 \pm 6$	
Relative humidity	$RH$	$35 \pm 20$	$79 \pm 18$	%
Wind speed	$v_a$	$3 \pm 1$	$2 \pm 2$	$m/s$
Direct Shortwave	$SW_{direct}$	$246 \pm 333$	$80 \pm 156$	$W m^{-2}$
Diffuse Shortwave	$SW_{diffuse}$	$0 \pm 0$	$58 \pm 87$	$W m^{-2}$
Hourly Precipitation	$ppt$	$0 \pm 0$	$139 \pm 457$	$mm$
Pressure	$p_a$	$623 \pm 3$	$794 \pm 9$	$hPa$
Start Date		Jan 18 2021	Nov 22 2020	
Expiry Date		June 20 2021	May 10 2021	

### 3.1.2 Meteorological data

Air temperature, relative humidity, wind speed, pressure, longwave and global shortwave radiation are required to calculate the surface energy balance of an AIR. The study period starts when the fountain was first switched on and ends when the respective AIR melted completely. These two dates are denoted as start and expiry dates henceforth. Each AIR is abbreviated based on the country code of the study site with the year of its expiry date. The resulting dataset highlights the difference in meteorological influences driving ice volume evolution in the two study sites (see Table 3.1).

### 3.1.3 Fountain observations

The fountain consists of a pipeline and a nozzle. The pipeline has three attributes, namely : discharge rate ( $Q$ ), height ( $h$ ) and water temperature ( $T_F$ ). Discharge rate represents the discharge rate of the water in the fountain pipeline. Height denotes the height of the fountain pipeline installed. Fountain water temperature is the temperature of water droplets produced by the fountain.

The fountain nozzle has three characteristics, namely : the aperture diameter ( $dia$ ), the spray radius ( $r$ ) and pressure loss ( $P$ ) . Spray radius denotes the observed ice radius formed from the fountain water droplets. Pressure loss denotes the loss of water head caused due to the fountain nozzle.

TABLE 3.2: List of all the studied AIRs

Name	Start Date	Expiry Date	No. of flights	Spray radius
Traditional CH20			2	
Traditional CH21	Nov 22 2020	May 10 2021	8	6.9 m
Traditional IN21	Jan 18 2021	June 20 2021	6	10.2 m
Traditional CH22	Dec 8 2021	April 12 2022	8	
Automated CH22	Dec 8 2021	April 12 2022	6	

### 3.1.4 Drone flights

Several photogrammetric surveys were conducted for each of the AIRs. The details of these surveys and the methodology used to produce the corresponding outputs are explained in [20]. The digital elevation models (DEMs) generated from the obtained imagery were analysed to document the ice radius, the surface area and the volume of the ice structures. Ice radius measurements of drone flights which observed either an increase in AIR circumference or volume were averaged to determine the fountain's spray radius. The number of drone surveys conducted for the traditional and the automated AIRs were 8 and 6, respectively (see Table ??).

## 3.2 AIR Model

A bulk energy and mass balance model is used to calculate the amounts of ice, meltwater, water vapour and wastewater of the AIR. In each hourly time step, the model uses the AIR surface area, energy balance and mass balance calculations to estimate its ice volume, surface temperature and wastewater as shown in Fig. 3.2 .

### 3.2.1 Surface area calculation

The model assumes the AIR shape to be a cone and assigns the following shape attributes:

$$A_{cone}^i = \pi \cdot r_{cone}^i \cdot \sqrt{(r_{cone}^i)^2 + (h_{cone}^i)^2} \quad (3.1a)$$

$$V_{cone}^i = \pi/3 \cdot (r_{cone}^i)^2 \cdot h_{cone}^i \quad (3.1b)$$

$$j_{cone}^i = \frac{\Delta M_{ice}^i}{\rho_{water} * A_{cone}^i} \quad (3.1c)$$

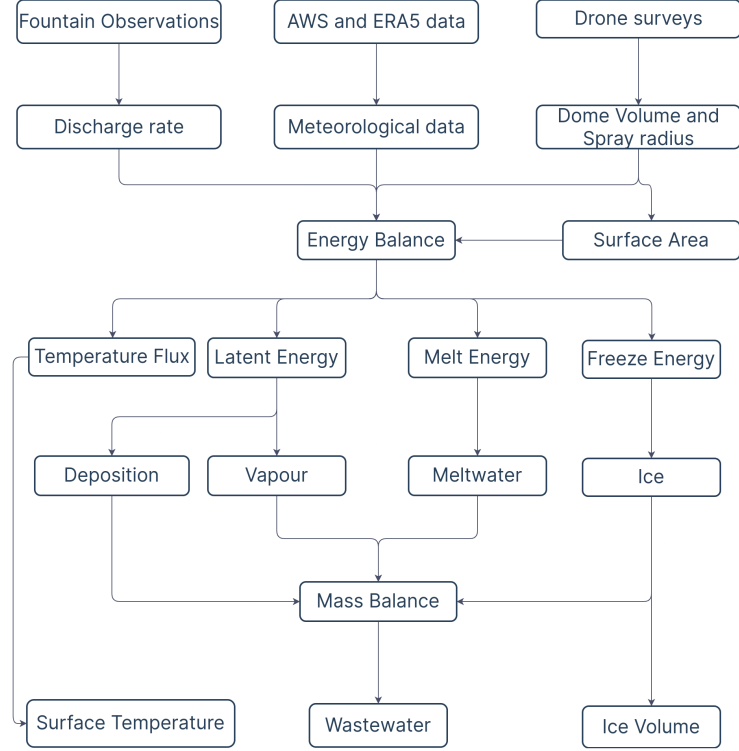


FIGURE 3.2: Model schematic showing the workflow used in the model at every time step.

where  $i$  denotes the model time step,  $r_{cone}^i$  is the radius;  $h_{cone}^i$  is the height;  $A_{cone}^i$  is the surface area;  $V_{cone}^i$  is the volume and  $j_{cone}^i$  is the AIR surface normal thickness change as shown in Fig. 3.3.  $M_{ice}^i$  is the mass of the AIR and  $\Delta M_{ice}^i = M_{ice}^{i-1} - M_{ice}^{i-2}$ . Henceforth, the equations used display the model time step superscript  $i$  only if it is different from the current time step.

AIR density can be defined as:

$$\rho_{cone} = \frac{M_F + M_{dep} + M_{ppt}}{(M_F + M_{dep})/\rho_{ice} + M_{ppt}/\rho_{snow}} \quad (3.2)$$

where  $M_F$  is the cumulative mass of the fountain discharge;  $M_{ppt}$  is the cumulative precipitation;  $M_{dep}$  is the cumulative accumulation through water vapour deposition;  $\rho_{ice}$  is the ice density ( $917 \text{ kg m}^{-3}$ ) and  $\rho_{snow}$  is the density of wet snow ( $300 \text{ kg m}^{-3}$ ) taken from [21].

AIR volume can also be expressed as:

$$V_{cone} = \frac{M_{ice}}{\rho_{cone}} \quad (3.3)$$

The initial radius of the AIR is assumed to be  $r_F$ . The initial height  $h_0$  depends on the dome volume  $V_{dome}$  used to construct the AIR as follows:

$$h_0 = \Delta x + \frac{3 \cdot V_{dome}}{\pi \cdot (r_F)^2} \quad (3.4)$$

where  $\Delta x$  is the surface layer thickness (defined in Section 3.2.2)

During the subsequent time steps, the dimensions of the AIR evolve assuming a uniform thickness change ( $j_{cone}$ ) across its surface area with an invariant slope  $s_{cone} = \frac{h_{cone}}{r_{cone}}$ . During these time steps, the volume is parameterised using Eqn. 3.1b as:

$$V_{cone} = \frac{\pi \cdot (r_{cone})^3 \cdot s_{cone}}{3} \quad (3.5)$$

We define the Icestupa boundary through its spray radius, i.e. we assume ice formation is negligible when  $r_{cone} > r_F$ . Combining Eqns. 3.1b, 3.3, 3.4 and 3.5, the geometric evolution of the Icestupa at each time step  $i$  can be determined by considering the following rules:

$$(r_{cone}, h_{cone}) = \begin{cases} (r_F, h_0) & \text{if } i = 0 \\ (r_{cone}^{i-1}, \frac{3 \cdot M_{ice}}{\pi \cdot \rho_{ice} \cdot (r_{cone}^{i-1})^2}) & \text{if } r_{cone}^{i-1} \geq r_F \text{ and } \Delta M_{ice} > 0 \\ (\frac{3 \cdot M_{ice}}{\pi \cdot \rho_{ice} \cdot s_{cone}})^{1/3} \cdot (1, s_{cone}) & \text{otherwise} \end{cases} \quad (3.6)$$

### 3.2.2 Energy balance calculation

We approximate the energy balance at the surface of an AIR by a one-dimensional description of energy fluxes into and out of a (thin) layer with thickness  $\Delta x$ :

$$\rho_{cone} \cdot c_{ice} \cdot \frac{\Delta T}{\Delta t} \cdot \Delta x = q_{SW} + q_{LW} + q_L + q_S + q_F + q_R + q_G \quad (3.7)$$

Upward and downward fluxes relative to the ice surface are positive and negative, respectively. The first term is the energy change of the surface layer, which can be translated into a phase change energy should phase changes occur.  $q_{SW}$  is the net shortwave radiation;  $q_{LW}$  is the net longwave radiation;  $q_L$  and  $q_S$  are the turbulent latent and sensible heat fluxes.  $q_F$  and  $q_R$  represent the heat exchange of the fountain water droplets and rain droplets with the AIR ice surface respectively.  $q_G$  represents ground heat flux between the AIR surface and its interior.

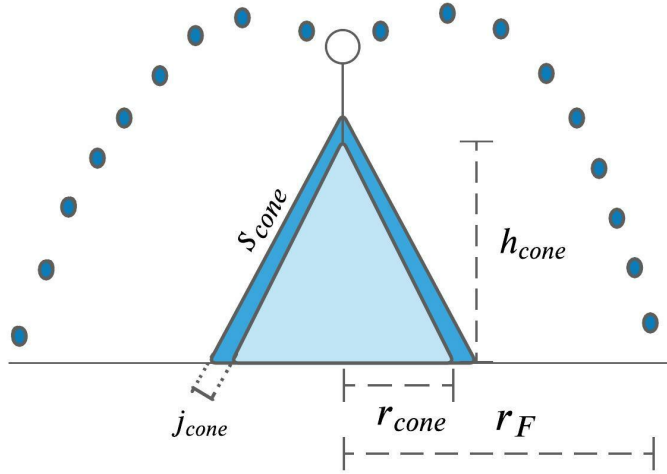


FIGURE 3.3: Shape variables of the AIR.  $r_{cone}$  is the radius,  $h_{cone}$  is the height,  $j_{cone}$  is the thickness change and  $s_{cone}$  is the slope of the ice cone.  $r_F$  is the spray radius of the fountain.

The density of the AIR  $\rho_{cone}$  was parameterised as follows:

$$\rho_{cone} = \frac{M_F + M_{dep} + M_{ppt}}{(M_F + M_{dep})/\rho_{ice} + M_{ppt}/\rho_{snow}} \quad (3.8)$$

where  $M_F$  is the cumulative mass of the fountain discharge;  $M_{ppt}$  is the cumulative precipitation;  $M_{dep}$  is the cumulative accumulation through water vapour deposition;  $\rho_{ice}$  is the ice density ( $917 \text{ kg m}^{-3}$ ) and  $\rho_{snow}$  is the density of wet snow ( $300 \text{ kg m}^{-3}$ ) taken from [21].

The energy flux acts upon the AIR surface layer, which has an upper and lower boundary defined by the atmosphere and the ice body of the AIR, respectively. Here, we define the surface temperature  $T_{ice}$  to be the modelled average temperature of the icestupa surface layer.

### 3.2.2.1 Net Shortwave Radiation $q_{SW}$

The net shortwave radiation  $q_{SW}$  is computed as follows:

$$q_{SW} = (1 - \alpha) \cdot (SW_{direct} \cdot f_{cone} + SW_{diffuse}) \quad (3.9)$$

where  $SW_{direct}$  and  $SW_{diffuse}$  are the direct and diffuse shortwave radiation,  $\alpha$  is the modelled albedo and  $f_{cone}$  is the area fraction of the ice structure exposed to the direct shortwave radiation.

The albedo varies depending on the water source that formed the current AIR surface layer. During the fountain runtime, the albedo assumes a constant value corresponding to ice albedo. However, after the fountain is switched off, the albedo can reset to snow albedo during snowfall events and then decay back to ice albedo. We use the scheme described in [22] to model this process. The scheme records the decay of albedo with time after fresh snow is deposited on the surface.  $\delta t$  records the number of time steps after the last snowfall event. After snowfall, albedo changes over a time step,  $\delta t$ , as

$$\alpha = \alpha_{ice} + (\alpha_{snow} - \alpha_{ice}) \cdot e^{(-\delta t)/\tau} \quad (3.10)$$

where  $\alpha_{ice}$  is the bare ice albedo value (0.25),  $\alpha_{snow}$  is the fresh snow albedo value (0.85) and  $\tau$  is a decay rate (16 days), which determines how fast the albedo of the ageing snow recedes back to ice albedo. Discharge events decrease the decay rate by a factor of  $\alpha_{ice}/\alpha_{snow}$ .

The solar area fraction  $f_{cone}$  of the ice structure exposed to the direct shortwave radiation depends on the shape considered. Using the solar elevation angle  $\theta_{sun}$ , the solar beam can be considered to have a vertical component, impinging on the horizontal surface (semicircular base of the AIR), and a horizontal component impinging on the vertical cross section (a triangle). The solar elevation angle  $\theta_{sun}$  used is modelled using the parametrisation proposed by [23]. Accordingly,  $f_{cone}$  is determined as follows:

$$f_{cone} = \frac{(0.5 \cdot r_{cone} \cdot h_{cone}) \cdot \cos\theta_{sun} + (\pi \cdot (r_{cone})^2/2) \cdot \sin\theta_{sun}}{\pi \cdot r_{cone} \cdot ((r_{cone})^2 + (h_{cone})^2)^{1/2}} \quad (3.11)$$

The diffuse shortwave radiation is assumed to impact the conical AIR surface uniformly.

### 3.2.2.2 Net Longwave Radiation $q_{LW}$

The net longwave radiation  $q_{LW}$  is determined as follows:

$$q_{LW} = LW_{in} - \sigma \cdot \epsilon_{ice} \cdot (T_{ice} + 273.15)^4 \quad (3.12)$$

where  $T_{ice}$  is the modelled surface temperature given in [],  $\sigma = 5.67 \cdot 10^{-8} J m^{-2} s^{-1} K^{-4}$  is the Stefan-Boltzmann constant,  $LW_{in}$  denotes the incoming longwave radiation and  $\epsilon_{ice}$  is the corresponding emissivity value for the Icestupa surface (0.97).

The incoming longwave radiation  $LW_{in}$  for the Indian site, where no direct measurements were available, is determined as follows:

$$LW_{in} = \sigma \cdot \epsilon_a \cdot (T_a + 273.15)^4 \quad (3.13)$$

here  $T_a$  represents the measured air temperature and  $\epsilon_a$  denotes the atmospheric emissivity. We approximate the atmospheric emissivity  $\epsilon_a$  using the equation suggested by [24], considering air temperature and vapor pressure (Eqn. 3.14). The vapor pressure of air over water and ice was obtained using Eqn. 3.17. The expression defined in [25] for clear skies (first term in equation 3.14) is extended with the correction for cloudy skies after [24] as follows:

$$\epsilon_a = 1.24 \cdot \left( \frac{p_{v,w}}{(T_a + 273.15)} \right)^{1/7} \cdot (1 + 0.22 \cdot cld^2) \quad (3.14)$$

with a cloudiness index  $cld$ , ranging from 0 for clear skies to 1 for complete overcast skies. For the Indian site, we assume cloudiness to be negligible.

### 3.2.2.3 Turbulent fluxes

The turbulent sensible  $q_S$  and latent heat  $q_L$  fluxes are computed with the following expressions proposed by [26]:

$$q_S = \mu_{cone} \cdot c_a \cdot \rho_a \cdot p_a / p_{0,a} \cdot \frac{\kappa^2 \cdot v_a \cdot (T_a - T_{ice})}{\left( \ln \frac{h_{AWS}}{z_0} \right)^2} \quad (3.15)$$

$$q_L = \mu_{cone} \cdot 0.623 \cdot L_s \cdot \rho_a / p_{0,a} \cdot \frac{\kappa^2 \cdot v_a (p_{v,w} - p_{v,ice})}{\left( \ln \frac{h_{AWS}}{z_0} \right)^2} \quad (3.16)$$

where  $h_{AWS}$  is the measurement height above the ground surface of the AWS (around 2 m for all sites),  $v_a$  is the wind speed in [ $m s^{-1}$ ],  $c_a$  is the specific heat of air at constant pressure ( $1010 J kg^{-1} K^{-1}$ ),  $\rho_a$  is the air density at standard sea level ( $1.29 kg m^{-3}$ ),  $p_{0,a}$  is the air pressure at standard sea level (1013 hPa),  $p_a$  is the measured air pressure,  $\kappa$  is the von Karman constant (0.4),  $z_0$  is the surface roughness (3 mm) and  $L_s$  is the heat

of sublimation ( $2848 \text{ kJ kg}^{-1}$ ). The vapor pressure of air with respect to water ( $p_{v,w}$ ) and with respect to ice ( $p_{v,ice}$ ) was obtained using the formulation given in [27] :

$$\begin{aligned} p_{v,w} &= e^{\frac{(34.494 - \frac{4924.99}{T_a + 237.1})}{(T_a + 105)^{1.57 \cdot 100}}} \cdot \frac{RH}{100} \\ p_{v,ice} &= e^{\frac{(43.494 - \frac{6545.89}{T_{ice} + 278})}{(T_{ice} + 868)^{2 \cdot 100}}} \end{aligned} \quad (3.17)$$

The dimensionless parameter  $\mu_{cone}$  is an exposure parameter that deals with the fact that AIR has a rough appearance and forms an obstacle to the wind regime. This factor accounts for the larger turbulent fluxes due to the roughness of the surface [28], and is a function of the AIR slope as follows:

$$\mu_{cone} = 1 + \frac{s_{cone}}{2} \quad (3.18)$$

A possible source of error is the fact that wind measurements from the horizontal plane at the AWS are used, which might be different from those on a slope. However, without detailed datasets from the AIR surface, we retain this assumption.

### 3.2.2.4 Fountain discharge heat flux $q_F$

The fountain water temperature  $T_F$  is assumed to cool to 0 after contact with the ice surface.  $T_F$  is equal to the measured source water temperature. But during time periods when the ambient temperature is subzero,  $T_F$  is assumed to be 0. Thus, the heat flux caused by this process is:

$$q_F = \begin{cases} \frac{\Delta M_F \cdot c_{water} \cdot T_F}{\Delta t \cdot A_{cone}} & \text{if } T_{temp} > 0 \\ 0 & \text{otherwise} \end{cases} \quad (3.19)$$

with  $c_{water}$  as the specific heat of water ( $4186 \text{ J kg}^{-1} K^{-1}$ ).

### 3.2.2.5 Rain heat flux $q_R$

The influence of rain events on the albedo and the energy balance was assumed to be similar to that of discharge events. However, the water temperature of a rain event was assumed to equal to the air temeperature. Accordingly, the heat flux generated due to a rain event was equal to:

$$q_R = \frac{\Delta M_{ppt} \cdot c_{water} \cdot T_a}{\Delta t \cdot A_{cone}} \quad (3.20)$$

### 3.2.2.6 Bulk Icestupa heat flux $q_G$

The bulk Icestupa heat flux  $q_G$  corresponds to the ground heat flux in normal soils and is caused by the temperature gradient between the surface layer ( $T_{ice}$ ) and the ice body ( $T_{bulk}$ ). It is expressed by using the heat conduction equation as follows:

$$q_G = k_{ice} \cdot (T_{bulk} - T_{ice}^{i-1}) / l_{cone} \quad (3.21)$$

where  $k_{ice}$  is the thermal conductivity of ice ( $2.123 \text{ W m}^{-1} \text{ K}^{-1}$ ),  $T_{bulk}$  is the mean temperature of the ice body within the icestupa and  $l_{cone}$  is the average distance of any point in the surface to any other point in the ice body.  $T_{bulk}$  is initialised as 0 and later determined from Eqn. 3.21 as follows:

$$T_{bulk}^{i+1} = T_{bulk} - (q_G \cdot A \cdot \Delta t) / (M_{ice} \cdot c_{ice}) \quad (3.22)$$

Since AIRs typically have conical shapes with  $r_{cone} > h_{cone}$ , we assume that the center of mass of the cone body is near the base of the fountain. Thus, the distance of every point in the AIR surface layer from the cone body's center of mass is between  $h_{cone}$  and  $r_{cone}$ . Therefore, we calculate  $q_G$  assuming  $l_{cone} = (r_{cone} + h_{cone})/2$ .

### 3.2.2.7 Phase changes

In this section, the numerical procedures to model phase changes at the surface layer are explained. Let  $T_{temp}$  be the calculated surface temperature. Therefore, Eqn. 3.7 can be rewritten as:

$$q_{total} = \rho_{ice} \cdot c_{ice} \cdot \frac{(T_{temp} - T_{ice})}{\Delta t} \cdot \Delta x$$

where  $q_{total}$  represents the total energy available to be redistributed. Even if the numerical heat transfer solution produces temperatures which are  $T_{temp} > 0$ , say from intense shortwave radiation, the ice temperature must remain at  $T_{temp} = 0$ . The “excess” energy is used to drive the melting process. Moreover, the energy input is used to melt the surface ice layer, and not to raise the surface temperature to some unphysical value. Similarly, for freezing to occur, three conditions are required. Firstly, fountain water is

present ( $\Delta M_F > 0$ ) and secondly the calculated temperature of the ice,  $T_{temp}$ , is below 0. However, these two conditions are not sufficient as the latent heat turbulent fluxes can only contribute to temperature fluctuations. Therefore, an additional condition, namely,  $(q_{total} - q_L) < 0$ , is required. Depending on the above conditions, the total energy  $q_{total}$  can be redistributed for the melting ( $q_{melt}$ ), freezing ( $q_{freeze}$ ) and surface temperature change ( $q_T$ ) processes as follows:

$$q_{total} = \begin{cases} q_{freeze} + q_T & \text{if } \Delta M_F > 0 \text{ and } T_{temp} < 0 \text{ and } (q_{total} - q_L) < 0 \\ q_{melt} + q_T & \text{otherwise} \end{cases} \quad (3.23)$$

Henceforth, time steps when the the total energy is redistributed to the freezing energy are called freezing events and the rest of the time steps are called melting events.

During a freezing event, the AIR surface is assumed to warm to 0. The available energy ( $q_{total} - q_L$ ) is further increased due to this change in surface temperature represented by the energy flux:

$$q_0 = \frac{\rho_{ice} \cdot \Delta x \cdot c_{ice} \cdot T_{ice}^{i-1}}{\Delta t}$$

The available fountain discharge ( $\Delta M_F$ ) may not be sufficient to utilize all the freezing energy. At such times, the additional freezing energy further cools down the surface temperature. Accordingly, the surface energy flux distribution during a freezing event can be represented as:

$$(q_{freeze}, q_T) = \begin{cases} \left( \frac{\Delta M_F \cdot L_f}{A_{cone} \cdot \Delta t}, q_{total} + \frac{\Delta M_F \cdot L_f}{A_{cone} \cdot \Delta t} \right) & \text{if } \Delta M_F \text{ insufficient} \\ (q_{total} - q_L + q_0, q_L - q_0) & \text{otherwise} \end{cases} \quad (3.24)$$

If  $T_{temp} > 0$ , then energy is reallocated from  $q_T$  to  $q_{melt}$  to maintain surface temperature at melting point. The total energy flux distribution during a melting event can be represented as:

$$(q_{melt}, q_T) = \begin{cases} (0, q_{total}) & \text{if } T_{temp} \leq 0 \\ \left( \frac{T_{temp} \cdot \rho_{ice} \cdot c_{ice} \cdot \Delta x}{\Delta t}, q_{total} - \frac{T_{temp} \cdot \rho_{ice} \cdot c_{ice} \cdot \Delta x}{\Delta t} \right) & \text{if } T_{temp} > 0 \end{cases} \quad (3.25)$$

### 3.2.3 Mass balance calculation

The mass balance equation for an AIR is represented as:

$$\frac{\Delta M_F + \Delta M_{ppt} + \Delta M_{dep}}{\Delta t} = \frac{\Delta M_{ice} + \Delta M_{water} + \Delta M_{sub} + \Delta M_{waste}}{\Delta t} \quad (3.26)$$

where  $M_F$  is the cumulative mass of the fountain discharge;  $M_{ppt}$  is the cumulative precipitation;  $M_{dep}$  is the cumulative accumulation through water vapour deposition;  $M_{ice}$  is the cumulative mass of ice;  $M_{water}$  is the cumulative mass of melt water;  $M_{sub}$  represents the cumulative water vapor loss by sublimation and  $M_{waste}$  represents the fountain wastewater that did not interact with the AIR. The left hand side of equation 3.26 represents the rate of mass input and the right hand side represents the rate of mass output for an AIR.

Precipitation input is calculated as shown in equation 3.27b where  $\rho_w$  is the density of water ( $1000 \text{ kg m}^{-3}$ ),  $\Delta ppt/\Delta t$  is the measured precipitation rate in [ $\text{m s}^{-1}$ ] and  $T_{ppt}$  is the temperature threshold below which precipitation falls as snow. Here, snowfall events were identified using  $T_{ppt}$  as 1. Snow mass input is calculated by assuming a uniform deposition over the entire circular footprint of the AIR.

The latent heat flux is used to estimate either the evaporation and condensation processes or sublimation and deposition processes as shown in equation 3.27c. During the time steps at which the surface temperature is below 0 only sublimation and deposition can occur, but if the surface temperature reaches 0, evaporation and condensation can also occur. As the differentiation between evaporation and sublimation (and condensation and deposition) when the air temperature reaches 0 is challenging, we assume that negative (positive) latent heat fluxes correspond only to sublimation (deposition), i.e. no evaporation (condensation) is calculated.

Since we have categorized every time step as a freezing or melting event, we can determine the melting/freezing rates and the corresponding meltwater/ice quantities as shown in equations 3.27e, 3.27d and 3.27f. Having calculated all other mass components, the fountain wastewater generated every time step can be calculated using Eqn. 3.26.

$$\frac{\Delta M_F}{\Delta t} = \begin{cases} \frac{60}{\rho_w \cdot \Delta t} \cdot d_F & \text{if fountain is on} \\ 0 & \text{otherwise} \end{cases} \quad (3.27a)$$

$$\frac{\Delta M_{ppt}}{\Delta t} = \begin{cases} \pi \cdot (r_{cone})^2 \cdot \rho_w \cdot \frac{\Delta ppt}{\Delta t} & \text{if } T_a < T_{ppt} \\ 0 & \text{if } T_a \geq T_{ppt} \end{cases} \quad (3.27b)$$

$$\left( \frac{\Delta M_{dep}}{\Delta t}, \frac{\Delta M_{sub}}{\Delta t} \right) = \begin{cases} \frac{q_L \cdot A_{cone}}{L_s} \cdot (1, 0) & \text{if } q_L \geq 0 \\ \frac{q_L \cdot A_{cone}}{L_s} \cdot (0, -1) & \text{if } q_L < 0 \end{cases} \quad (3.27c)$$

$$\frac{\Delta M_{water}}{\Delta t} = \frac{q_{melt} \cdot A_{cone}}{L_f} \quad (3.27d)$$

$$\frac{\Delta M_{freeze/melt}}{\Delta t} = \frac{q_{freeze/melt} \cdot A_{cone}}{L_f} \quad (3.27e)$$

$$\frac{\Delta M_{ice}}{\Delta t} = \frac{q_{freeze} \cdot A_{cone}}{L_f} + \frac{\Delta M_{ppt}}{\Delta t} + \frac{\Delta M_{dep}}{\Delta t} - \frac{\Delta M_{sub}}{\Delta t} - \frac{\Delta M_{water}}{\Delta t} \quad (3.27f)$$

Considering AIRs as water reservoirs, their net water loss can be defined as:

$$\text{Net water losses} = \frac{M_{waste} + M_{sub}}{(M_F + M_{ppt} + M_{dep})} \cdot 100 \quad (3.28)$$

### 3.3 Model extensions

The AIR model presented above was extended in order to (a) recommend fountain scheduling strategies and (b) improve its transferability to new locations.

#### 3.3.1 Discharge rate scheduler

In this section, we focus on the description of the integration of fountain scheduling processes in the model.

Two types of fountain scheduling strategies are possible depending on the constraints of water supply and favourable weather window in the respective location. Locations constrained by their available water supply require water-sensitive fountain scheduling strategies and those constrained by the duration of favourable weather windows require weather-sensitive fountain scheduling strategies. These two kinds of scheduled fountains will be referred to as water-sensitive fountain and weather-sensitive fountain henceforth.

Water-sensitive fountains are expected to produce higher water use efficiency whereas weather-sensitive fountains are expected to produce higher ice volumes. Accordingly, we produce the discharge rate recommendations for these two kinds of fountains through

TABLE 3.3: Assumptions for the parametrisation introduced to simplify the model.

Estimation of	Symbol	IVOM	WEOM
Slope	$s_{cone}$	1	0
Albedo	$\alpha$	$\alpha_{snow}$	$\alpha_{ice}$
Cloudiness	$cld$	0	1

two sets of model forcing assumptions for the following three model variables: (a) slope , (b) albedo and (c) cloudiness. These two kinds of models will be referred to as ice volume optimised model (IVOM) and water-use efficiency optimised model (WEOM) respectively. The slope variable increases the shortwave radiation and sensible heat impact. The albedo variable decreases the shortwave radiation impact. The cloudiness variable increases both the shortwave and the longwave radiation impact. We associate the upper and lower bounds of these variables with the IVOM and WEOM versions depending on whether they overestimate and underestimate the freezing rate of the AIR as shown in Table 3.3.

We apply the assumptions described in Table 3.3 on the one-dimensional description of energy fluxes through Eqn. 3.7. The derivation of the individual energy and mass balance terms for the IVOM and WEOM model versions are discussed in Paper III.

### 3.3.2 Location classifier

The model, in its current form, is not expected to perform well for locations where it has not been calibrated for before. This limits its ability to identify and classify other favourable locations worldwide.

In this section, we showcase a strategy to improve the AIR model’s transferability to new locations. Specifically, in paper I, we highlight the sensitivity of the model to the surface layer thickness parameter. This parameter requires prior calibration for better model performance. However, the dependence of the model on this parameter can be removed if spatial temperature fluctuations across the ice structure are resolved.

Here we combine the AIR model with the COupled Snowpack and Ice surface energy and mass balance model in PYthon (COSIPY) in order to remove the calibration requirements for model performance. COSIPY is typically used for modelling distributed snow and glacier mass changes [29]. However, its flexible, user-friendly and modular framework makes it an ideal platform to implement the alternate modules required for modelling ice reservoirs. This modified COSIPY model will be referred to as COSIS-TUPA henceforth.

### 3.3.2.1 Model configuration

In this section, we describe all the adjustments to COSIPY modules necessary to convert it to the COSISTUPA model.

The cosy model input was extended to include discharge rate and cloudiness index measurements. Additionally, spray radius parameter was provided as input during model initialization. The model initialization of the ice dimensions were made identical to the AIR model.

Several parameterizations are available for estimating each of the surface processes in COSIPY. Most of the parameterizations used in the AIR model are among these options. But some parameterizations required minor modifications to be applicable for processes on a conical surface. Additionally, new parameterizations were required to estimate the conical shape evolution and model the freezing process due to the fountain discharge rate. To modify COSIPY into COSISTUPA, parametrizations of the following processes were modified:

- Fountain rain heat flux : The heat flux generated due to the difference in fountain water droplet temperature and surface temperature was introduced as a new energy balance component. This implementation is identical to that described in Sec. 3.2.2.4
- Turbulent flux scaling : The sensible and the latent heat fluxes were scaled by the  $\mu_{cone}$  factor introduced in Sec. 3.2.2.3
- Freezing process : Phase transition processes were introduced during time periods when the fountain discharge was active. These processes created new ice layers whenever the energy balance allowed it following the algorithm introduced in Sec. 3.2.2.7
- Conical shape evolution : The surface mass balance estimation was converted to the volume estimation through the methodology introduced in Sec. 3.2.1

Please note the above list of changes are not exhaustive and represent only the major modifications necessary to develop the COSISTUPA model.

### 3.3.2.2 Advantages

Execution time and multiprocessing workflow RMSE error User friendly and long-term maintenance

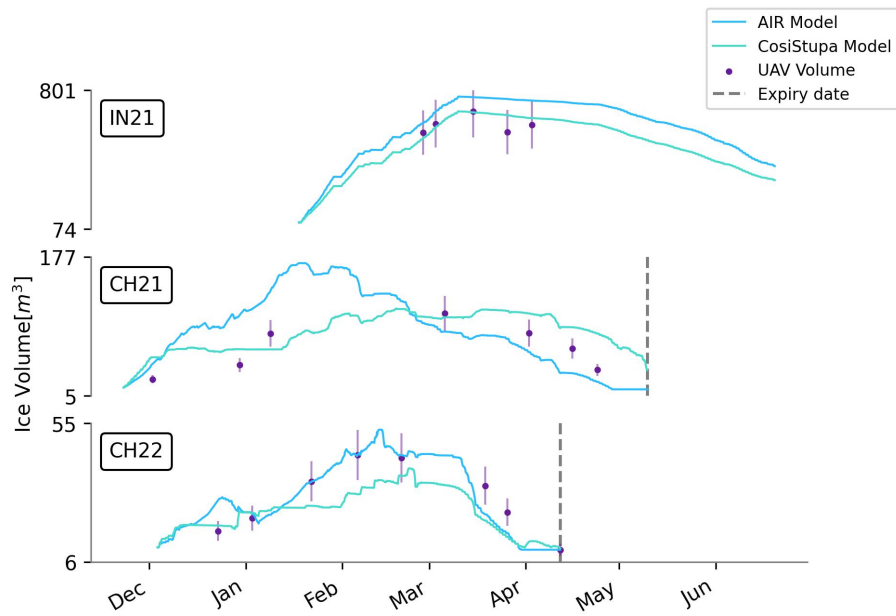


FIGURE 3.4

## 3.4 Suggestions

### 3.4.1 Model development

### 3.4.2 Further Data acquisition

#### 3.4.2.1 Meltwater quantities

#### 3.4.2.2 Fountain characteristics

#### 3.4.2.3 Drone flight analysis

### 3.4.3 Improvement of model algorithm

#### 3.4.3.1 Initialisation of model

#### 3.4.3.2 Better model parametrisations

# Chapter 4

## Habitat of ice reservoirs

AIRs cannot be built anywhere. They require sufficient water supply and weather conditions cold enough to amass a seasonal stock of ice. This imposes several meteorological and topographical requirements for the chosen construction location. The meteorological requirements can be used to identify favourable regions worldwide whereas the topographical requirements can be used to pinpoint the construction site within the respective region. Below we detail these requirements and propose methodologies for finding construction sites satisfying them.

### 4.1 Requirements for AIR construction

- **Water supply** : The water source of an AIR could be either a spring or a stream. Springs are the ideal water source since they are easy to transport via pipelines to the construction site due to their relatively warm temperatures. Other water sources have higher risks of pipeline freezing events.
- **Weather conditions** : AIRs prefer colder, drier and less-cloudy regions. Correspondingly, temperature, humidity and number of cloud-free days during the construction period can be used to rank different sites.
- **Topography** : AIRs prefer shadowed valleys. This is because these landforms have lower sunshine hours which is the major driver of the melting rate of all the AIRs studied in this thesis.



FIGURE 4.1: AIRs show significant variation in volume evolution depending on the choice of construction location.

#### 4.1.1 Checklist to identify AIR construction regions

Accordingly, we propose the following checklist to determine AIR site suitability. The values presented are determined based on past construction experiences and can be used as guidelines to avoid construction attempts in unfavourable sites.

1. Minimum mean monthly temperature less than 0.
2. Water supply with mean discharge rate more than  $2l/min$ .
3. Terrain slope between water source and site greater than 10 m every km.

#### 4.1.2 Metrics to rank sites within the same region

Given a valley or a region satisfying the above requirements, further selection of sites around the particular water supply can be performed using the criterions below:

1. Water source temperature is higher.
2. Daylight hours are lower.
3. Cloudy days are lower.
4. Temperature is lower.
5. Humidity is lower.

Such villages are expected to produce AIRs that supply daily meltwater in the order of thousands of litres for 2 months.

Different forms of AIRs show different sensitivities to each of these requirements. This is discussed in the next chapter.

# Chapter 5

## Technology of ice reservoirs

AIRs are a natural evolution of Ladakh's agricultural system. They can be related to traditional water harvesting technologies like the *zing*, which are small tanks where meltwater is collected through the use of an intricate network of channels. The mountain oases of the Hindu Kush and Karakoram ranges have similar irrigation networks [1].

### 5.1 Ice terraces

Ice terraces are the oldest form of AIRs [30]. Usually situated below the glaciers at elevations where snowmelt starts end of March, these structures facilitate the freezing of stream water during winter at selected sites, usually shaded by surrounding mountains. Chewang Norphel, a well known engineer of the Leh Nutrition Project, introduced this practice to Ladakh in the 1980s and 1990s [9].

#### 5.1.1 Construction strategy

There are four distinct types of ice terraces with site-specific modifications as shown in Fig. 5.1: the first type is built as cascades on perennial streams. A series of loose rock walls in the river bed reduce reduces flow velocity, but still lets water pass through. Such cascades allow flowing water to freeze on exposed surfaces and form superimposed ice layers when temperatures drop.

The second type diverts water from streams with higher flow velocity to small side valleys, shaded by surrounding mountains. This design allows to integrate higher slope positions for additional ice formation. It consists of a series of partially cemented stone

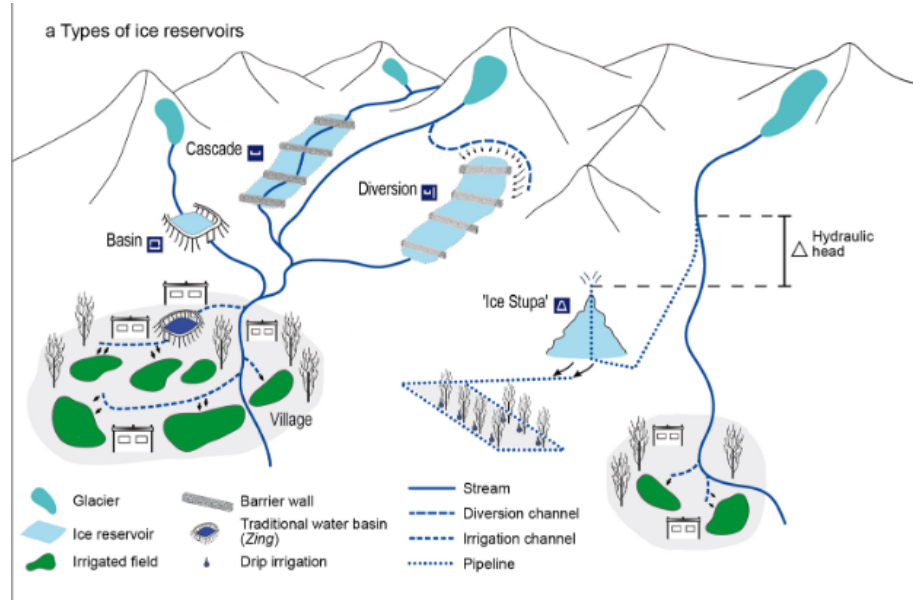


FIGURE 5.1: Adapted from: [11]

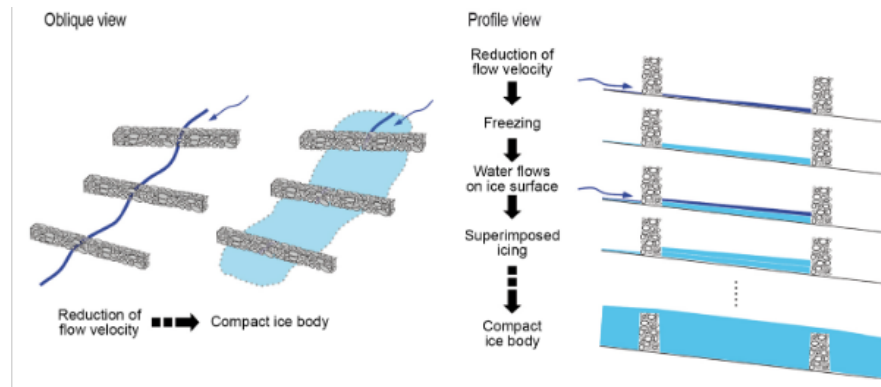


FIGURE 5.2: The process of ice accumulation for ice terraces Adapted from: [11]

walls across the stream bed. Their dimensions are adjusted based on the valley topography. The water for the ice terrace is obtained through a long diversion channel.

The third type is a basin structure, resembling the traditional *zing* form of water storage, but located above the cultivated fields.

### 5.1.2 Application

Over the past 30 years, 14 ice terraces have been constructed in central Ladakh, located in tributary valleys of the Indus. The oldest ice terrace was of the form cascades in Ladakh was built in 1987 at a favourable location between 4290 and 4640 m in Phuktse. However, according to oral history and Corona imagery from 1969, the first ice terrace of this design type are older than 50 years and can be found in Phuktse and Igoo. In

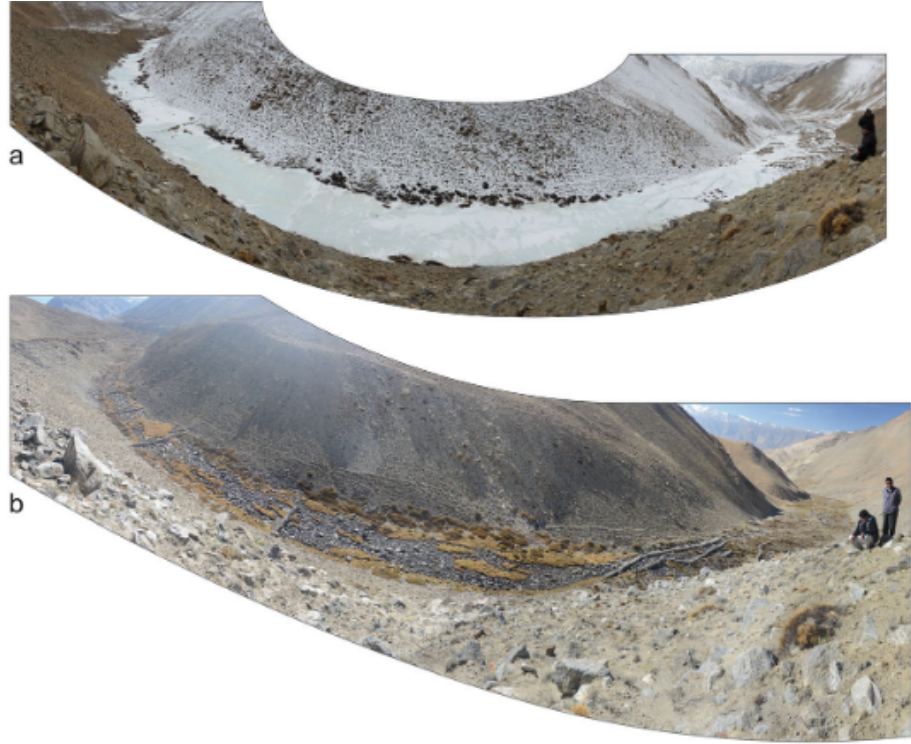


FIGURE 5.3: Ice terrace of Phuktse, viewpoint 4430 m. (a) February 2014 (b) October 2014 Adapted from: [11]

February 2014, Phuktse built a successful cascade with an almost continuous stretch of ice (Fig.).

### 5.1.3 Drawbacks

However, the location requirements and the construction cost of ice terraces were prohibitive for widespread adoption.

## 5.2 Ice stupas

This prompted the invention of Ice stupas by Sonam Wangchuk in 2013 ???. Due to their shape, Ice stupas could be built adjacent to the irrigated plantations. It was also relatively cheaper. A typical Ice stupa just requires a fountain nozzle mounted on a supply pipeline. The water source is usually a spring or a glacial stream. Due to the altitude difference between the pipeline input and fountain output, water ejects from the fountain nozzle as droplets that eventually lose their energy and accumulate as ice. The fountain is manually activated during the winter nights and is raised, through addition of metal pipes, when significant ice accumulates below.

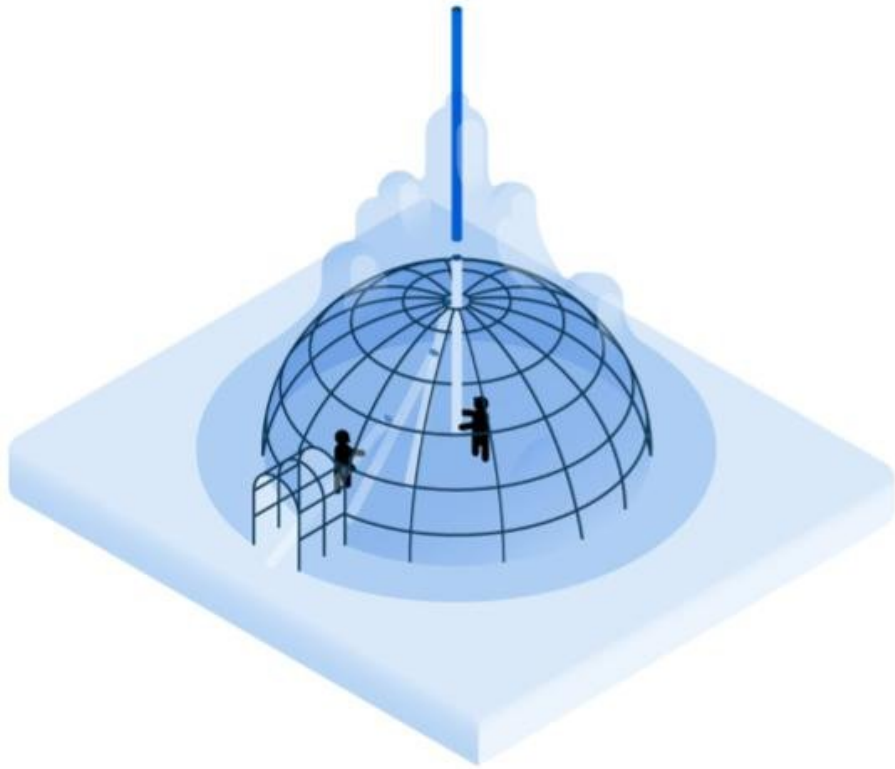


FIGURE 5.4: The process of ice accumulation for ice stupas. Diagram by: Francesco Muzzi

### 5.2.1 Construction strategy

A typical AIR (see Fig. ??) simply requires a fountain nozzle mounted on a supply pipeline. The water source is usually a high altitude lake or glacial stream. Due to the altitude difference between the pipeline input and fountain output, water ejects from the fountain nozzle as droplets which freeze under subzero winter conditions. The fountain is manually activated during winter nights. The fountain nozzle is raised through the addition of metal pipes when significant ice accumulates below. Typically, a dome of branches is constructed around the metal pipes so that pipe extensions can be done from within this dome. Threads, tree branches and fishing nets are used to guide and accelerate the ice formation.



FIGURE 5.5: Ice terrace of Phuktse, viewpoint 4430 m. (a) February 2014 (b) October 2014 Adapted from: [11]

### 5.2.2 Application

### 5.2.3 Drawbacks

## 5.3 Improvement of construction strategies through weather-sensitive automation systems

# Chapter 6

## Heritage of ice reservoirs

This chapter provides conclusions based on research findings from data collected on AIRs in Switzerland and India, as well as discussion and recommendations for future research. This Chapter will review the purpose of the study, research questions, literature review, and findings of the study. It will then present conclusions, discussion of the conclusions, and recommendations for practice and for further research.

### 6.1 Summary

Cryosphere fed irrigation networks are completely dependant on the timely availability of meltwater from glaciers, snow and permafrost. With the accelerated decline of glaciers, these irrigation networks can no longer deliver adequate water to sustain agricultural output and take advantage of the complete growing season. As a consequence, some mountain villages have either been abandoned or lie on the brink of desertification [31].

In the past few decades, artificial ice reservoir (AIR) technologies have provided much needed relief to these water-stressed communities. These strategies revolve around augmenting their glacial ice reservoirs with man-made ones that provide supplementary irrigation during the spring. In the context of the observed present and predicted global glacier shrinkage, the development of such water storage technologies is crucial to ensure continued sustenance of cryosphere-fed irrigation networks.

AIR observations and investigations date back to the mid-2000s [4]. The vast majority have been published in the 2010s, mostly using qualitative methods. However, quantifications of their storage capacity differ widely amongst these publications. [5, 11, 17].

We attempt to address this gap through a quantitative study on AIRs. With a special focus on ice stupas, a mass and energy balance model was developed and used as a

tool to quantify the influence of meteorological conditions and fountain characteristics. Because small-scale processes, complex feedbacks and non-linearities govern their evolution, modelling the volume evolution of ice stupas is only feasible if backed up with comprehensive input, calibration and validation datasets.

In response, we conducted measurement campaigns using drones, flowmeters and weather stations on almost a dozen AIRs across two locations (India and Switzerland), over four winters (2019, 2020, 2021 and 2022) and using two different construction methods (traditional and automated). Each dataset contained information on the meteorological conditions, fountain characteristics and AIR volume evolution. The meteorological and fountain observations were used as model input; AIR volume observations were used to calibrate the model parameters and validate its ice volume estimations.

## 6.2 Conclusions

The main objective of this thesis was to improve our understanding about the response of AIRs to changes in their construction location and fountain characteristics. In a first experiment, the evolution of AIRs in Indian Himalayas and the Swiss Alps are compared. In a second experiment, the evolution of AIRs using different fountain scheduling strategies are compared. The model results show:

1. Volumes of ice stupas located in different locations may differ by an order of magnitude. The differences could be attributed to the accelerated sublimation process in colder and drier locations.
2. Water losses of ice stupas may be upto 80 % due to excessive use of water by traditional construction strategies. However, weather-sensitive fountain systems can produce icestupas of similar volumes by using just one-tenth of the water supply.
3. Traditional construction strategies demand significant maintenance efforts since they are prone to fountain freezing events. However, automated construction strategies can prevent these events to make the construction process maintenance-free.

### **6.3 Discussion**

### **6.4 Recommendations**

- Colder, drier and less cloudy construction locations form long-lasting AIRs with higher maximum ice volumes.
- Weather-sensitive fountain systems produce larger and efficient AIRs effortlessly.

### **6.5 Suggestions for future research**

- Identification of favourable locations.
- Cosistupa model development.

### **6.6 Final thoughts**

# Paper I

## **Brief communication: Growth and decay of an ice stupa in alpine conditions – a simple model driven by energy-flux ob- servations over a glacier surface**

Oerlemans, J., S. Balasubramanian, C. Clavuot, and F. Keller. The Cryosphere 15, no. 6 (2021): 3007–12. doi:10.5194/tc-15-3007-2021.



## Brief communication: Growth and decay of an ice stupa in alpine conditions – a simple model driven by energy-flux observations over a glacier surface

Johannes Oerlemans<sup>1</sup>, Suryanarayanan Balasubramanian<sup>2</sup>, Conradin Clavuot<sup>3</sup>, and Felix Keller<sup>4,5</sup>

<sup>1</sup>Institute for Marine and Atmospheric Research, Utrecht University, Princetonplein 5, Utrecht, 3585CC, the Netherlands

<sup>2</sup>Department of Geosciences, University of Fribourg, Fribourg, Switzerland

<sup>3</sup>Architecture Clavuot, Gängelistrasse 49, Chur 7000, Switzerland

<sup>4</sup>Academia Engiadina, Samedan, Switzerland

<sup>5</sup>Department of Environmental Systems Science, ETH, Zurich, Switzerland

**Correspondence:** Johannes Oerlemans (j.oerlemans@uu.nl)

Received: 13 February 2021 – Discussion started: 1 April 2021

Revised: 30 May 2021 – Accepted: 4 June 2021 – Published: 29 June 2021

**Abstract.** We present a simple model to calculate the evolution of an ice stupa (artificial ice reservoir). The model is formulated for a cone geometry and driven by energy balance measurements over a glacier surface for a 5-year period. An “exposure factor” is introduced to deal with the fact that an ice stupa has a very rough surface and is more exposed to wind than a flat glacier surface. The exposure factor enhances the turbulent fluxes.

For characteristic alpine conditions at 2100 m, an ice stupa may reach a volume of 200 to 400 m<sup>3</sup> in early April. We show sensitivities of ice stupa size to temperature changes and exposure factor. The model may also serve as an educational tool, with which the effects of snow cover, switching off water during daytime, different starting dates, switching off water during high wind speeds, etc. can easily be evaluated.

### 1 Introduction

Ice stupas (Fig. 1), also referred to as artificial ice reservoirs (AIRs), are used more and more as a means to store water in the form of ice (Nüsser et al., 2018). In Ladakh, India, engineer Sonam Wangchuk initiated and developed the use of ice stupas to provide water for irrigation purposes in spring and early summer. The ice stupas grow in winter by sprinkling water on the growing ice structure, and they melt in spring and summer to deliver water; a typical turnover volume is up

to  $1 \times 10^6$  L. Ice stupas also form interesting touristic attractions with a distinct and special artistic flavour. They come in the same class as ice sculptures, which are popular in all regions of the world that have a cold winter.

The possibility to grow ice stupas of appreciable size depends on the meteorological conditions and the availability of water. When a surface has a negative energy balance and water is sprayed on it, ice will form (a well-known technique to make skating rinks). The more effective the latent heat of fusion can be removed by contact with cold air and effective emittance of longwave radiation, the faster the ice layer may grow. In spring and summer incoming solar radiation will dominate and the ice stupa will lose mass.

In this note we present a model of ice stupa growth and decay, based on a simple consideration of the total energy budget, and driven by energy flux observations over a glacier surface (half hourly observations over a 5-year period). We believe that the energy balance of a glacier surface and of an ice stupa have much in common and therefore consider this data set as ideal for a first study. The focus is on alpine conditions at a typical height of 2100 m a.s.l. The purpose of this study is to obtain first-order estimates of how fast an ice stupa may grow and melt and what processes are most important. We emphasize that in this note the focus is on the energetics of the ice stupa system, not on the technical aspects that have to be dealt with in constructing an ice stupa.

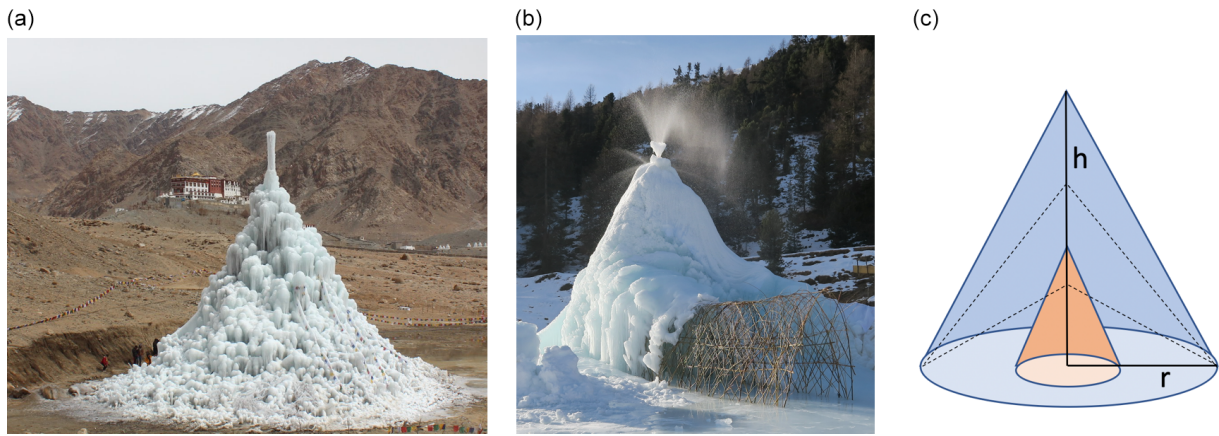


**Figure 1.** (a) Ice stupa in Ladakh, India (courtesy of Sonam Wangchuk). (b) Early growing stage of ice stupa with inner structure in Val Roseg, Switzerland (courtesy of Conradin Clavou). (c) Simple geometrical representation. The ice stupa can have an inner structure (brown). The dashed lines illustrate the growth of an ice stupa from a base with a constant radius.

## 2 Geometry

Ice stupas have different and often complex shapes. The *cone* is probably the most appropriate simple geometric shape to represent an ice stupa (Fig. 1), but alternatively a *dome* (half sphere) could also be considered.

The geometric characteristics of a cone with radius  $r$  and height  $h$  are

$$\text{Area of base: } \pi r^2, \quad (1a)$$

$$\text{Lateral area: } \pi r \sqrt{r^2 + h^2}, \quad (1b)$$

$$\text{Volume: } \pi r^2 h / 3. \quad (1c)$$

It is useful to introduce a shape parameter  $s = h/r$ . The volume can then also be written as

$$V = \pi h^3 / 3s^2. \quad (2)$$

So for a given volume the height of the ice stupa can be calculated from

$$h = \left\{ \frac{3}{\pi} V s^2 \right\}^{1/3}. \quad (3)$$

In this note we will consider two cases: (i) the shape factor is constant during growth and decay, and (ii) the ice stupa grows upward from a base with a fixed radius, implying that the shape factor gradually increases. The first case may be more appropriate when an inner structure is used or when water supply is by varying sprinkler properties or even manually. Case (ii) describes better the situation when a fixed spray radius is maintained during the growth phase.

## 3 Energy exchange

Ice stupas exchange energy with the surroundings by absorbing and reflecting solar radiation, absorbing and emitting longwave (terrestrial) radiation, and by turbulent fluxes

of sensible and latent heat. Because of the complex shape of an ice stupa, as compared to a horizontal ice/snow surface, it is hard to describe these processes in detail. However, some simplifying assumptions may help to arrive at reasonable approximations.

We use 5 years of energy balance measurements with an automatic weather station (AWS) on the Vadret da Morteratsch (Morteratsch Glacier) (e.g. Oerlemans et al., 2009), which was located at an elevation of about 2280 m a.s.l. The surface energy flux is written as

$$\text{energy flux} = S_{\text{in}} - S_{\text{out}} + L_{\text{in}} - L_{\text{out}} + H + G. \quad (4)$$

$S_{\text{in}}$  stands for solar radiation,  $S_{\text{out}}$  for reflected solar radiation,  $L_{\text{in}}$  for incoming longwave radiation,  $L_{\text{out}}$  for emitted longwave radiation,  $H$  for the total turbulent heat flux, and  $G$  for the ground heat flux (conduction from or into the surface layer – generally small compared to the other components). These quantities are normally expressed in  $\text{W m}^{-2}$ . So the energy flux is positive when directed towards the surface. A positive energy flux will be used for melting of ice or snow; when the energy flux is negative freezing of water can take place (when available).

We now discuss how these measurements over (almost) flat terrain can be applied to an ice stupa. We first deal with solar radiation and consider the direct part (fraction  $q$ ) and diffuse part (fraction  $1 - q$ ) separately. Although the ratio of direct to diffuse solar radiation depends strongly on cloud conditions, outside subtropical climate zones where low cloudiness prevails the components are typically of the same order of magnitude (e.g. Li et al., 2015; Berrizbeitia et al., 2020).

With respect to direct solar radiation, the solar beam can be considered to have a vertical component, impinging on the horizontal surface (base of the ice stupa), and a horizontal component impinging on the vertical cross section (a triangle). Measurements over a flat surface, like those from

the glacier AWS, thus underestimate the solar radiation intercepted by an ice stupa. A correction factor  $f$  is therefore needed with which the direct radiation as measured by the AWS has to be multiplied. This factor may be large for a low sun, but in alpine conditions where there is always significant shading by the surroundings this situation is rarely found. A simple analysis shows that, for a shape factor of  $s = 2$ ,  $f$  varies from 2.5 for a solar elevation of  $20^\circ$  to about 1.2 for a solar elevation of  $60^\circ$ . To account for the fact that the correction factor should be 1 for a flat surface and increase with the shape factor, we use (note that  $f$  and  $s$  are dimensionless)

$$f = 1 + s/4. \quad (5)$$

For the *diffuse* part of the solar radiation, illumination is on all sides and the relevant area therefore is the lateral area as given in Eq. (1b). Therefore the total amount of absorbed solar radiation per unit of time can be estimated as (in  $\text{J s}^{-1}$ )

$$F_{\text{sol}} = f q (S_{\text{in}} - S_{\text{out}}) \pi r^2 + (1 - q) (S_{\text{in}} - S_{\text{out}}) \pi r \sqrt{r^2 + h^2}. \quad (6)$$

Alternatively, one may wish to prescribe the albedo  $\alpha$  separately, i.e.

$$F_{\text{sol}} = f q S_{\text{in}} (1 - \alpha) \pi r^2 + (1 - q) S_{\text{in}} (1 - \alpha) \pi r \sqrt{r^2 + h^2}. \quad (7)$$

For the longwave radiation and turbulent exchange, the exposed surface is also the lateral area. The longwave radiation balance then becomes

$$F_{\text{lw}} = (L_{\text{in}} - L_{\text{out}}) \pi r \sqrt{r^2 + h^2}. \quad (8)$$

The turbulent heat fluxes depend on the roughness and exposure of the surface. Since we do not calculate the surface (skin) temperature, we simply assume that it is close to the melting point. The sensible and latent heat input are calculated using the well-known bulk transfer equations (e.g. Garrett, 1992):

$$F_H = \mu \rho c_p C U (T - T_s) \pi r \sqrt{r^2 + h^2} \quad (9)$$

$$F_L = 0.623 \mu \rho L_v C U p^{-1} (e_s - e) \pi r \sqrt{r^2 + h^2}. \quad (10)$$

Here  $C$  is the bulk turbulent exchange coefficient over a flat surface,  $T$  is the air temperature,  $T_s$  is the surface temperature (set to the melting point),  $\rho$  is air density,  $L_v$  is the latent heat of sublimation ( $2830000 \text{ J kg}^{-1}$ ),  $c_p$  is the specific heat capacity of air ( $1004 \text{ J kg}^{-1} \text{ K}^{-1}$ ),  $e$  is the vapour pressure,  $e_s$  is the saturation vapour pressure,  $p$  is atmospheric pressure, and  $U$  is the wind speed. The total turbulent heat flux  $H$  is just the sum of the fluxes of sensible and latent heat.

The dimensionless parameter  $\mu$  is an “exposure/roughness parameter” that deals with the fact that an ice stupa has a rough appearance and forms an obstacle to the wind regime. So  $\mu$  is expected to be larger than 1 and could perhaps have a

value of 2 or more. For a larger shape parameter the exposure will be larger; we therefore use

$$\mu = 1 + s/2. \quad (11)$$

Equation (9) is no more than an educated guess. It is hard to base estimates of this parameter on information in the literature. Many studies have been carried out on the effect of obstacles on atmospheric boundary layer flow (e.g. trees, but also buildings), but always in an ensemble setting, looking at the bulk effect of an ensemble of obstacles. We deal with a case of a single obstacle in open terrain, and we are confident that the roughness of the surface and the exposure will lead to larger turbulent fluxes. Given the uncertainty in the exposure parameter, later on we will present results for different values.

When water availability is unlimited, the mass gain or loss is given by

$$dM/dt = (F_{\text{sol}} + F_{\text{lw}} + F_L + F_H)/L_m + F_L/L_v. \quad (12)$$

$M$  is the mass of the ice stupa and  $L_m$  is the latent heat of melting/fusion ( $334000 \text{ J kg}^{-1}$ ). For typical alpine conditions the last term in Eq. (10) is normally quite small. Since the volume of the ice stupa is simply related to the mass ( $V = M/\rho_{\text{ice}}$ ), the height of the stupa can directly be calculated for a given shape factor (case i) or given radius (case ii).

#### 4 Application to the Oberengadin region, Switzerland

Over the past few years, several ice stupas have been constructed in the Oberengadin, southeast Switzerland. In the winter of 2017/2018 an ice stupa was constructed in the Val Roseg at 2000 m a.s.l. (Fig. 1, maximum height about 12 m). In the winter of 2018/2019 several smaller ice stupas (height about 5 m) were built at a site in the Val Morteratsch at about 1900 m a.s.l. Since February 2021 a test site for ice stupa construction has been in operation at the Diavolezza Talstation at an altitude of 2080 m a.s.l.

To obtain first-order estimates of growth and decay rates for typical climatic conditions in the Oberengadin, we used the energy balance measurements from the automatic weather station on the Vadret da Morteratsch as a proxy for this high alpine region. During the period 1 July 2007–30 September 2012, the AWS on the Vadret da Morteratsch was located at an altitude of about 2280 m a.s.l. and has produced a unique data set without any gaps. The annual melt at the AWS location was between 5 and 7 m of ice. With a focus on the Diavolezza site, which is at an altitude of 2080 m a.s.l., a temperature correction of  $+1.3 \text{ K}$  was applied to the input data (based on a standard atmospheric temperature lapse rate of  $0.0065 \text{ K m}^{-1}$ ). We note that all the locations mentioned above are within a distance of 10 km from each other (interactive map to find locations: <https://map.wanderland.ch>, last access: 25 June 2021).

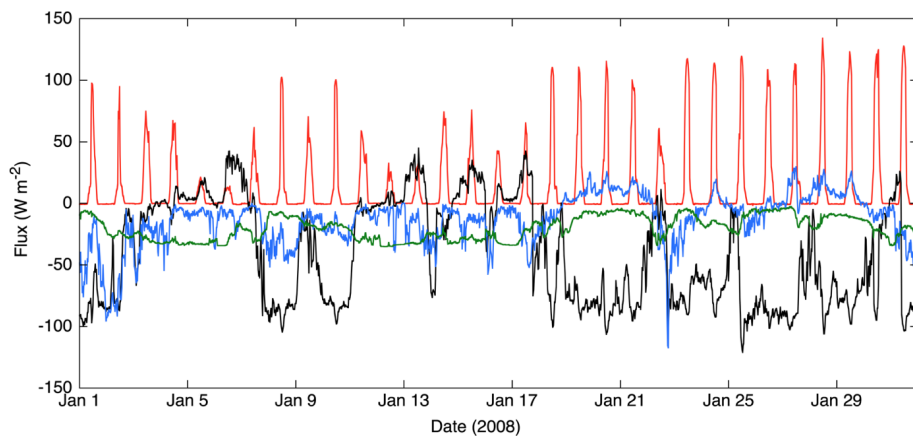


**Figure 2.** Energy balance components as measured by the AWS on the Vadret da Morteratsch for January 2008. Net solar radiation in red, net longwave radiation flux in black, turbulent sensible heat flux in blue, turbulent latent heat flux in green.

Figure 2 shows an example of data from the AWS. The data have been stored as 30 min averages. The turbulent heat fluxes have been calculated from the wind speed, air temperature, and humidity, where the turbulent exchange coefficient  $C$  was used as a tuning parameter (to obtain the correct amount of observed ice melt over a 5-year period). The example shown is just for one relatively sunny winter month (January 2008). Note the large degree of compensation between net solar radiation and net longwave radiation – the well-known effect in clear sky conditions on the radiation balance. As a consequence, the turbulent heat fluxes are more important than it appears at first sight.

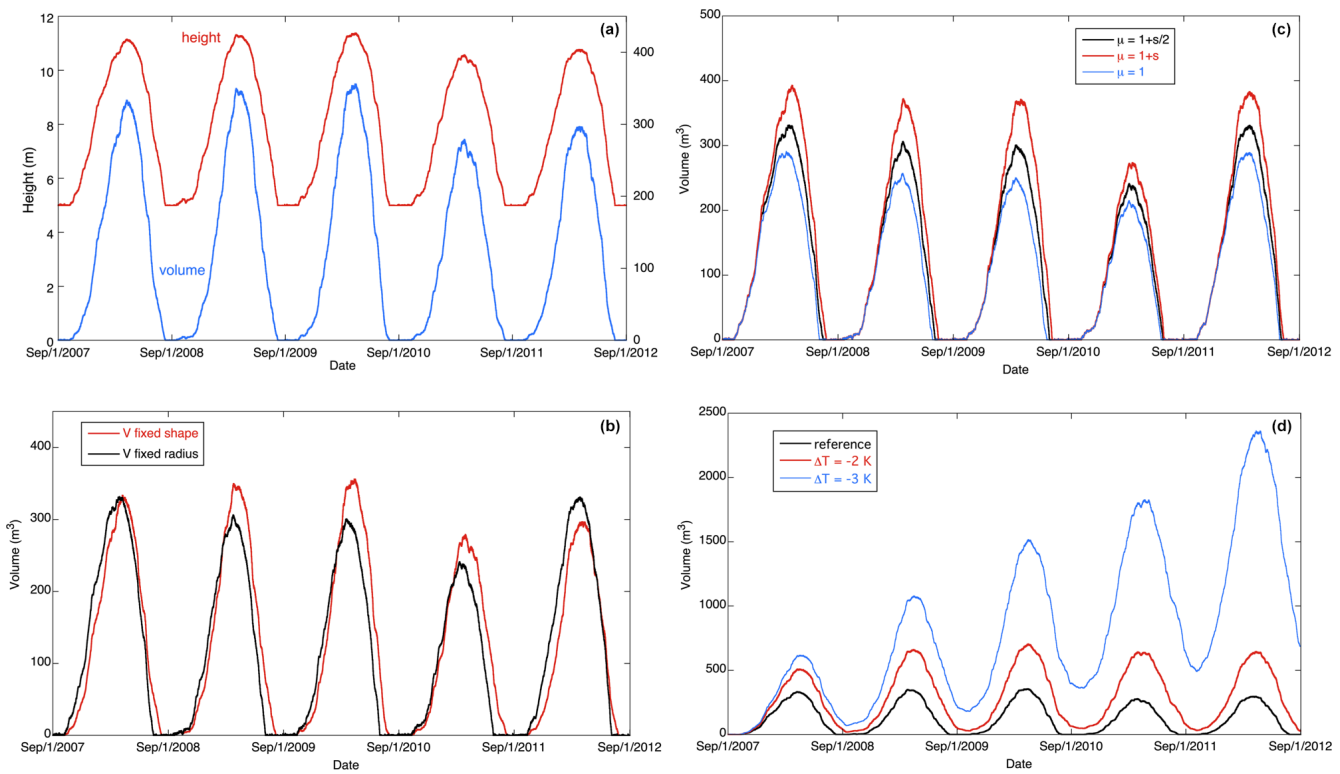
Figure 3 summarizes model results in terms of ice stupa height and volume for 5 years. In all calculations we used  $q = 0.5$  and  $\alpha = 0.6$ . It has been assumed that water availability is unlimited. In the first example (Fig. 3a) we show the evolution of an ice stupa on a 5 m high inner structure. In the model this is simply achieved by setting  $h = 5$  m at the start of the integration and correct the total volume afterwards for the volume of the inner structure. The use of an inner structure has the advantage that the freezing area is larger from the beginning and that the typical ice stupa shape is achieved relatively fast. The shape factor has been taken constant and equal to 2. We see some differences among the years: the maximum ice stupa height varies between 10 and 12 m and is normally reached in early April. For the last 2 years the simulated ice stupa volume is smaller mainly because of slightly higher temperatures and larger insolation. The decay of the ice stupa is hardly faster than the growth. A faster decay would occur if the albedo were not constant but would be prescribed to decrease during the melt phase (which is more realistic in most cases).

Figure 3b shows a comparison between the fixed-shape simulation just described and a fixed-radius simulation with  $r = 7$  m. This value of the radius was chosen to obtain more or less the same ice stupa volume. It can be seen that in the first stage of growth the volume for the fixed-radius case in-

creases somewhat faster than for the fixed-shape case. Nevertheless, the differences in the curves are not large and point to the fact that in the end the energy constraints determine how much ice can form (in the case of unlimited water availability).

Because the value of the exposure parameter  $\mu$  is highly uncertain, we show the sensitivity of the fixed-radius ice stupa volume to different formulations (Fig. 3c). For  $\mu = 1$ , implying that the situation is equivalent to that of a flat surface, the stupa volume is significantly smaller than in the reference case ( $\mu = 1 + s/2$ ). A stronger dependence of  $\mu$  on the shape factor ( $\mu = 1 + s$ ) increases the stupa volume by about 25 %. For a larger shape factor, the mostly negative turbulent fluxes in winter increase, and this is not compensated by a larger interception of solar radiation.

In the simulations discussed so far the ice stupas disappear in summer. One may ask the question under what conditions an ice stupa may survive the summer and grow to a larger size in the next winter. A possible way to study this question is to decrease the air temperature uniformly (temperature change  $\Delta T$ ). This will imply a stronger negative sensible heat flux in winter and a weaker positive heat flux in summer, thus accelerating stupa growth and slowing down its decay. We found a break-even point for  $\Delta T \approx -2$  K (Fig. 3d). For larger negative values of  $\Delta T$  the ice stupa does not disappear in summer and keeps growing from year to year. For  $\Delta T \approx -3$  K, the maximum volume in the fifth year ( $\sim 2400$  m $^3$ ) is about 4 times that in the first year ( $\sim 600$  m $^3$ ). We note that in this calculation the effect of lower temperatures on the net longwave radiation balance has not been taken into account, because the radiation fluxes were prescribed according to the AWS observations. It is likely that we therefore underestimate the effect of lower air temperature.



**Figure 3.** Calculated evolution of ice stupa for the case of unlimited water supply for five winters. **(a)** Height and volume for the case with an inner structure (height 5 m) and fixed shape. **(b)** Volume for the case with an inner structure and the case with a fixed radius (7 m). **(c)** The effect of the exposure parameter  $\mu$  on the volume (fixed radius). **(d)** The effect of a negative temperature perturbation. For  $\Delta T = -3 \text{ K}$  the stupa does not disappear anymore but is growing from year to year (fixed shape).

## 5 Discussion

The data set used to simulate ice stupa growth and decay for typical conditions in the Oberengadin is probably quite appropriate. The setting of the location of the AWS (on the lower tongue of the Vadret da Morteratsch when it still existed) and the Diavolezza Talstation are rather similar: the altitude is about the same, and the valley is relatively wide. However, differences in the wind statistics are likely to exist, but they are difficult to assess. The Morteratsch AWS reveals a steady katabatic (glacier) wind most of the time, whereas the Diavolezza Talstation is more exposed to the larger-scale wind regime. It seems likely that the average wind speed at the Diavolezza Talstation is somewhat higher than at the AWS site, where the 5-year average wind speed is  $2.8 \text{ m s}^{-1}$ . In contrast, the sites in the Val Roseg and Val Morteratsch are more sheltered and wind speeds are probably lower.

The examples presented here are best-case scenarios with respect to ice stupa growth. In practice it is not always possible to have unlimited water availability, and it may be difficult to sprinkle the water more or less evenly over the stupa, especially at higher wind speeds. The choice of the shape of the ice stupa depends on the sprinkling strategy. It may be more realistic to describe an ice stupa with different shapes

for the growth phase (e.g. fixed radius) and decay phase (e.g. constant shape factor). Such an approach can easily be accommodated in the model.

We note that the ice stupa volume calculated here for alpine conditions at  $\sim 2100 \text{ m a.s.l.}$  (typically  $250 \text{ m}^3$ ) is significantly smaller than the volumes obtained in the big ice stupas in Ladakh. Winter conditions in Ladakh are considerably colder and therefore growth rates can be much larger.

In this exploratory study a solid comparison between observed and simulated stupa sizes was not attempted. However, we note that the maximum height of the stupa in the Val Roseg was 12 m, which is in good agreement with the stupa height shown in Fig. 3a.

The model presented here is simple, basically because we consider the ice stupa to be a single unit with a surface temperature close to the melting point. As soon as this constraint is relaxed and the surface temperature of the stupa is considered to be a dependent variable, the whole procedure becomes more complicated, and some processes can be studied more explicitly. Nevertheless, we believe that the simple approach presented in this note, which requires no more than one page of coding, is a useful tool to obtain first-order estimates of growth and decay rates under various conditions. Effects of snow cover, switching off water during daytime,

switching of water supply for high wind speeds, different starting dates, differences between warm and cold winters, etc. can be evaluated. We finally note that the model can easily be reformulated for another geometry, e.g. a dome.

*Data availability.* The 5-year data set from the weather station on the Vadret da Morteratsch is available on request.

*Author contributions.* JO designed, coded, and ran the model. Through their experience in constructing ice stupas, SB, CC, and FK have made important contributions concerning the concept and application of the model. JO wrote the text of this communication.

*Competing interests.* The authors declare that they have no conflict of interest.

*Disclaimer.* Publisher's note: Copernicus Publications remains neutral with regard to jurisdictional claims in published maps and institutional affiliations.

*Acknowledgements.* We thank the reviewers and editor for their constructive comments. The operation of the weather station on the Vadret da Morteratsch was made possible by the NWO-SPINOZA grant (Dutch Research Council) to Johannes Oerlemans.

*Review statement.* This paper was edited by Chris Derksen and reviewed by Jonathan D. Mackay and two anonymous referees.

## References

- Berrizbeitia, S. E., Cago, E. J., and Muneer, T.: Empirical models of the estimation of solar sky-diffusive radiation. A review and experimental analysis, *Energies*, 13, 701, <https://doi.org/10.3390/en13030701>, 2020.
- Garratt, J.: *The Atmospheric Boundary Layer*, Cambridge University Press, 316 pp., ISBN 0521380529, 1992.
- Li, D. H. W., Lou, S. W., and Lam, J. C.: An analysis of global, direct and diffuse solar radiation, *Energy Procedia*, 75, 388–393, 2015.
- Nüsser, M., Dame, J., Kraus, B., Baghel, R., and Schmidt, S.: Socio-hydrology of artificial glaciers in Ladakh, India: assessing adaptive strategies in a changing cryosphere, *Reg. Environ. Change*, 19, 1327–1337, <https://doi.org/10.1007/s10113-018-1372-0>, 2018.
- Oerlemans, J., Giesen, R. H., and Van den Broeke, M. R.: Retreating alpine glaciers: increased melt rates due to accumulation of dust (Vadret da Morteratsch, Switzerland), *J. Glaciol.*, 55, 729–736, 2009.

## Paper II

# **Influence of Meteorological Conditions on Artificial Ice Reservoir (Icestupa) Evolution**

Balasubramanian, S., Hoelzle, M., Lehning, M., Bolibar, J., Wangchuk, S., Oerlemans, J., and Keller, F.

Frontiers in Earth Science 9 (February 23, 2022): 771342. doi:10.3389/feart.2021.771342.



# Influence of Meteorological Conditions on Artificial Ice Reservoir (Icestupa) Evolution

Suryanarayanan Balasubramanian<sup>1,2\*</sup>, Martin Hoelzle<sup>1</sup>, Michael Lehning<sup>3</sup>, Jordi Bolibar<sup>4</sup>, Sonam Wangchuk<sup>2</sup>, Johannes Oerlemans<sup>4</sup> and Felix Keller<sup>5,6</sup>

<sup>1</sup>Department of Geosciences, University of Fribourg, Fribourg, Switzerland, <sup>2</sup>Himalayan Institute of Alternatives Ladakh, Leh, India,

<sup>3</sup>WSL Institute for Snow and Avalanche Research, Davos, Switzerland, <sup>4</sup>Institute for Marine and Atmospheric Research, Utrecht University, Utrecht, Netherlands, <sup>5</sup>Academia Engiadina, Samedan, Switzerland, <sup>6</sup>ETH, Zürich, Switzerland

## OPEN ACCESS

### Edited by:

Thomas Vikhamar Schuler,  
University of Oslo, Norway

### Reviewed by:

Alan Rempel,  
University of Oregon, United States  
Lukas U. Arenson,  
BGC Engineering, Canada

### \*Correspondence:

Suryanarayanan Balasubramanian  
suryanarayanan.balasubramanian@  
unifr.ch

### Specialty section:

This article was submitted to  
Cryospheric Sciences,  
a section of the journal  
Frontiers in Earth Science

Received: 06 September 2021

Accepted: 23 December 2021

Published: 23 February 2022

### Citation:

Balasubramanian S, Hoelzle M, Lehning M, Bolibar J, Wangchuk S, Oerlemans J and Keller F (2022)  
Influence of Meteorological Conditions  
on Artificial Ice Reservoir  
(Icestupa) Evolution.  
*Front. Earth Sci.* 9:771342.  
doi: 10.3389/feart.2021.771342

Since 2014, mountain communities in Ladakh, India have been constructing dozens of Artificial Ice Reservoirs (AIRs) by spraying water through fountain systems every winter. The meltwater from these structures is crucial to meet irrigation water demands during spring. However, there is a large variability associated with this water supply due to the local weather influences at the chosen location. This study compared the ice volume evolution of an AIR built in Ladakh, India with two others built in Guttannen, Switzerland using a surface energy balance model. Model input consisted of meteorological data in conjunction with fountain discharge rate (mass input of an AIR). Model calibration and validation were completed using ice volume and surface area measurements taken from several drone surveys. The model was successful in estimating the observed ice volume evolution with a root mean square error within 18% of the maximum ice volume for all the AIRs. The location in Ladakh had a maximum ice volume four times larger compared to the Guttannen site. However, the corresponding water losses for all the AIRs were more than three-quarters of the total fountain discharge due to high fountain wastewater. Drier and colder locations in relatively cloud-free regions are expected to produce long-lasting AIRs with higher maximum ice volumes. This is a promising result for dry mountain regions, where AIR technology could provide a relatively affordable and sustainable strategy to mitigate climate change induced water stress.

**Keywords:** icestupa, water storage, climate change adaptation, geoengineering, energy balance (EB) model, water resource management, Ladakh

## 1 INTRODUCTION

Seasonal snow cover and glaciers are expected to change their water storage capacity due to climate change with major consequences for downriver water supply (Immerzeel et al., 2019). The challenges brought about by these changes are especially important for dry mountain environments such as in Central Asia or the Andes, which directly rely on the seasonal meltwater for their farming and drinking needs (Unger-Shayesteh et al., 2013; Chen et al., 2016; Buytaert et al., 2017; Apel et al., 2018; Hoelzle et al., 2019).

Ladakh, sandwiched between the Himalayan ranges and the Karakoram in India, is one such region experiencing climate change induced water stress. Glaciers in the Ladakh region are vital for sustaining agricultural activities which form the basis for regional food security and socio-economic



**FIGURE 1 |** Icestupa in Ladakh, India on March 2017 was 24 m tall and contained around  $3,700 \text{ m}^3$  of water. Picture Credits: Lobzang Dadul.

development (Labbal, 2000; Schmidt and Nüsser, 2012). During a low precipitation year, glacier melt and snowmelt are the only sources of water supply to the region (Thayyen and Gergan, 2010). Some villages in Ladakh have already been forced to relocate due to glacial retreat and the corresponding loss of their main fresh water resources (Grossman, 2015).

Around 26 villages in this region (Wangchuk, 2021) have been using artificial ice reservoirs (AIR) to adapt to these changes since they require very little infrastructure, skills and energy to be constructed in comparison to other water storage technologies (Nüsser et al., 2019b; Hock et al., 2019). An AIR is a human-made ice structure typically constructed during the cold winter months and designed to slowly release freshwater during the warm spring and summer months. The main purpose of AIRs is irrigation. Therefore, AIRs are designed to store water in the form of ice as long into the summer as possible. The energy required to construct an AIR is usually derived from the gravitational head of the source water body. Some are constructed horizontally by freezing water using a series of checkdams while others are built vertically by spraying water through fountain systems (Nüsser et al., 2019a). The latter are colloquially referred to as Icestupas and are the subject of this study.

A typical AIR (see **Figure 1**) simply requires a fountain nozzle mounted on a supply pipeline. The water source is usually a high altitude lake or glacial stream. Due to the altitude difference between the pipeline input and fountain output, water ejects from the fountain nozzle as droplets which freeze under subzero winter conditions. The fountain is manually activated during winter nights. The fountain nozzle is raised through the addition of metal pipes when significant ice accumulates below. Typically, a dome of branches is constructed around the metal pipes so that pipe extensions can be done from within this dome. Threads, tree branches and fishing nets are used to guide and accelerate the ice formation.

However, to date, no reliable estimates exist about the quantity of meltwater an AIR can provide (Nüsser et al., 2019a). Moreover, preliminary estimates of AIRs in Ladakh

indicate that they generate high water losses during their lifetimes (see **Supplementary Appendix 7.1**). During their accumulation period, AIRs can lose excessive fountain water and, during the ablation period, sublimation losses could also be significant. However, the relative contribution of these processes in the total water loss remains unknown.

In this paper, we develop a physically-based model of vertical AIRs (or Icestupas) that can estimate their freezing and melting rates. Mass and energy balance equations were used to estimate the quantity of ice, meltwater, sublimation and wastewater. Sensitivity and uncertainty analysis were performed to identify the most sensitive parameters and the variance they caused. For calibration, we chose two AIRs built across the winter of 2020/21 in India and Switzerland, and validated the model on a Swiss AIR built during winter 2019/20. Our model results provide a first step towards evaluating the potential of this decade old water storage technology worldwide (Wangchuk, 2014).

## 2 STUDY SITES AND DATA

The model requires three kinds of datasets containing weather, fountain and AIR volume measurements to accurately calibrate, estimate and validate the ice volume of AIRs. Through the winters of 2018/19, 2019/20 and 2020/21, such datasets were acquired for four AIRs in both Switzerland and India. Here, we present the results of three AIRs, which have a complete dataset. Two of them were constructed in the same Swiss location called Guttannen (referred to with the prefix CH) but during different winters, and the other was constructed at Ganges, India (referred to with the prefix IN). The 2020/21 AIR constructed on both these locations are shown in **Figure 2**.

The Guttannen site ( $46.66^\circ\text{N}, 8.29^\circ\text{E}$ ) in the Bern region lies at  $1047 \text{ m a.s.l.}$ . In the winter (Oct-Apr), mean daily minimum and maximum air temperatures vary between  $-13$  and  $15^\circ\text{C}$ . Clear skies are rare, averaging around 7 days during winter. Daily winter precipitation can sometimes be as high as  $100 \text{ mm}$ . These values are based on 30 years of hourly weather model simulations (Meteoblue, 2021). The site was situated adjacent to a stream resulting in high humidity values across the study period as shown in **Figure 2**. AIR were constructed here by the Guttannen Bewegt Association during the winters of 2019–20 (CH20) and 2020–21 (CH21). Tree branches were laid covering the fountain pipe to initiate the ice formation process. The fountain height varied between 2 and 5 m during the construction period. The water was transferred from a spring water source and flowed via a flowmeter to the nozzle. In addition, a webcam guaranteed a continuous survey of the site during the construction of the AIR.

The Ganges site ( $34.22^\circ\text{N}, 77.61^\circ\text{E}$ ) is located around 20 km north of Leh city in the Ladakh region, lying at  $4025 \text{ m a.s.l.}$ . The mean annual temperature is  $5.6^\circ\text{C}$ , and the thermal range is characterized by high seasonal variation. During January, the coldest month, the mean temperature drops to  $-7.2^\circ\text{C}$ . During August, the warmest month, the mean temperature rises to

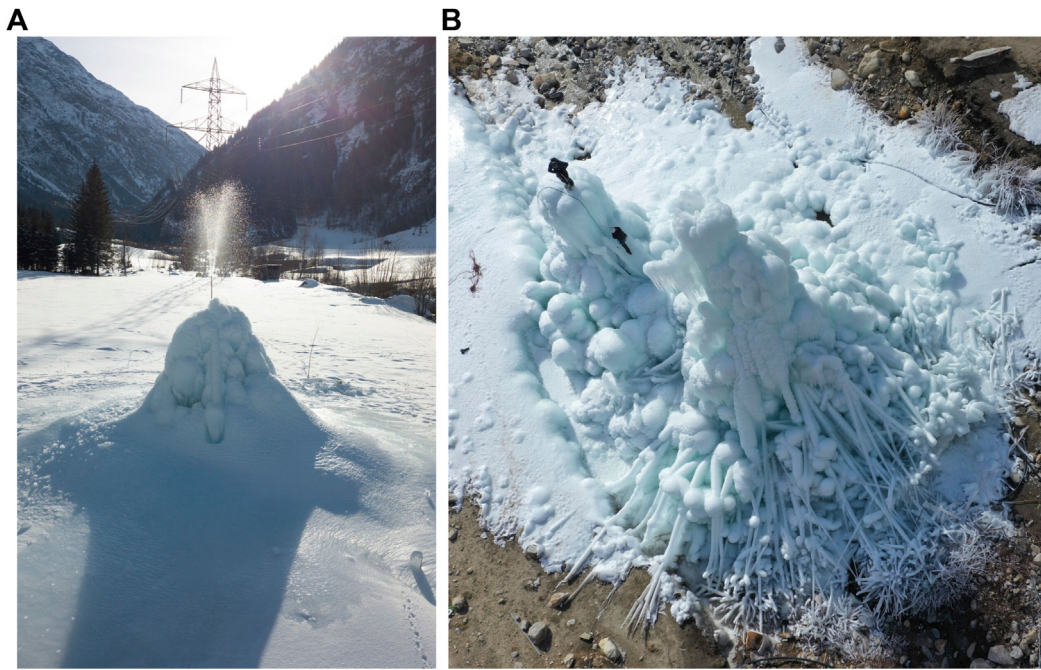


**FIGURE 2 |** The Swiss and Indian AIRs were 5 m and 13 m tall on January 9 and March 3, 2021 respectively. Picture credits: Daniel Bürki (**A**) and Thinles Norboo (**B**).

**TABLE 1 |** Summary of the weather and fountain observations. The expiry date refers to the date when all of the ice of the AIR completely disappeared and only the dome volume remains. The weather measurements are shown using their mean ( $\mu$ ) and standard deviation ( $\sigma$ ) during the study period as  $\mu \pm \sigma$ .

	Name	Symbol	IN21	CH21	CH20	Units
Weather	Air temperature	$T_a$	$0 \pm 7$	$2 \pm 6$	$2 \pm 4$	°C
	Relative humidity	$RH$	$35 \pm 20$	$79 \pm 18$	$77 \pm 17$	%
	Wind speed	$V_a$	$3 \pm 1$	$2 \pm 2$	$2 \pm 2$	m/s
	Direct Shortwave	$SW_{direct}$	$246 \pm 333$	$80 \pm 156$	$80 \pm 150$	W m <sup>-2</sup>
	Diffuse Shortwave	$SW_{diffuse}$	$0 \pm 0$	$58 \pm 87$	$51 \pm 74$	W m <sup>-2</sup>
	Incoming Longwave Radiation	$LW_{in}$	$194 \pm 31$	$239 \pm 35$	$236 \pm 34$	W m <sup>-2</sup>
	Hourly Precipitation	$ppt$	$0 \pm 0$	$139 \pm 457$	$95 \pm 404$	mm
	Pressure	$P_a$	$623 \pm 3$	$794 \pm 9$	$798 \pm 7$	hPa
	Start Date		Jan 18 2021	Nov 22 2020	Jan 3 2020	
	Expiry Date		June 20 2021	May 10 2021	April 6 2020	
Fountain	Discharge rate	$d_F$	60	7.5	7.5	l/min
	Runtime	$t_F$	829	2155	1553	hours
	Spray radius	$r_F$	10.2	6.9	7.7	m
	Water temperature	$T_F$	1.5	1.5	1.5	°C

17.5 °C (Nüsser et al., 2012). Because of the rain shadow effect of the Himalayan Range, the mean annual precipitation in Leh totals less than 100 mm, and there is high interannual variability. Whereas the average summer rainfall between July and September reaches 37.5 mm, the average winter precipitation between January and March amounts to 27.3 mm and falls almost entirely as snow. AIRs were constructed here as part of the Ice Stupa Competition by the Himalayan Institute of Alternatives, Ladakh (HIAL). The fountain height of the AIR varied between 5 and 9 m.

## 2.1 Meteorological Data

Air temperature, relative humidity, wind speed, pressure, longwave, shortwave direct and diffuse radiation are required to calculate the surface energy balance of an AIR (see Table 1). The study period starts when the fountain was first switched on and ends when the respective AIR melted completely. These two dates are denoted as start and expiry dates henceforth.

For the CH site, the primary weather data source was a meteoswiss AWS located 184 m away (Station ID: 0-756-0-GTT). In addition, we used ERA5 reanalysis dataset

**TABLE 2 |** Summary of the drone surveys.

	No.	Date	Volume (m <sup>3</sup> )	Radius (m)	Surface Area (m <sup>2</sup> )
IN21	1	Jan 18, 2021	103	9.1	411
	2	Feb 27, 2021	580	10.2	668
	3	Mar 3, 2021	626	10.3	694
	4	Mar 15, 2021	692	10	681
	5	Mar 26, 2021	582	10.2	671
	6	Apr 3, 2021	620	10.1	658
CH21	1	Nov 22, 2020	13	5.4	136
	2	Dec 2, 2020	26	5.7	118
	3	Dec 30, 2020	43	7.5	189
	4	Jan 9, 2021	82	6.5	150
	5	Mar 6, 2021	108	7.5	183
	6	Apr 2, 2021	83	6.5	150
	7	Apr 16, 2021	64	6.2	134
	8	Apr 24, 2021	37	4.7	80
CH20	1	Jan 3, 2020	24	6.7	170
	2	Jan 24, 2020	59	7.7	228

(Copernicus Climate Change Service (C3S), 2017) for filling data gaps and adding the shortwave and longwave radiation data that were not measured directly. The ERA5 reanalysis dataset is known to have a high correlation with sites in Switzerland (Scherrer, 2020). The Guttannen temperature dataset had a correlation greater than 0.8 with the ERA5 temperature for both winters. The ERA5 grid point chosen (46.64 °N, 8.25 °E) for the Swiss site was around 3.6 km away from the actual site. ERA5 variables (except incoming shortwave and longwave radiation) were fitted to the meteoswiss dataset via linear regressions. The zero wind speed values recorded by the meteoswiss AWS whenever snow accumulated on the ultrasonic wind sensor were replaced using the ERA5 dataset.

For the IN site, two different weather data sources were used to log all weather parameters required for the model. Temperature, humidity, wind speed and pressure data were logged with a weather station located 440 m away from the construction site. Shortwave radiation data were derived from another weather station located 15 km away. Unfortunately, precipitation was not logged. Since winter precipitation in Ladakh is less than 30 mm (Nüsser et al., 2012), we can safely assume negligible precipitation and mostly clear skies. As a consequence, the diffuse fraction of the global shortwave radiation was also assumed to be negligible. Temperature and humidity were measured with a rotronic sensor with an accuracy of  $\pm 0.3$  °C and  $\pm 1\%$  respectively. A young sensor measured the wind speed with an accuracy of  $\pm 0.3 \text{ ms}^{-1}$  and a setra sensor measured the pressure with an accuracy of  $\pm 0.01 \text{ hPa}$ .

## 2.2 Fountain Observations

We define the fountain used through four attributes; namely, its spray radius, mean discharge rate, discharge runtime and water temperature as shown in **Table 1**. Continuous measurement of the discharge rate was unsuccessful in all sites due to data logger malfunctions of the associated flowmeter. Instead the discharge

duration was first determined and then the available discharge measurement was used to determine the average discharge rate  $d_F$  during these periods. The spray radius  $r_F$  was estimated from the mean AIR circumference measured in the drone surveys during the fountain runtime.

The Swiss fountain discharge duration was extrapolated from just one fountain on and off event each. Even though the Indian fountain was never manually switched off, there were many pipeline freezing events that interrupted the discharge duration. Discharge rate was extrapolated to be the mean discharge rate  $d_F$  except during these pipeline freezing events.

## 2.3 Drone Surveys

Several photogrammetric surveys using drones were conducted on the Swiss and Indian sites. The details of these surveys and the methodology used to produce the corresponding outputs are explained in **Supplementary Appendix 7.2**. The digital elevation maps (DEMs) generated from the obtained imagery were analysed to document the radius, surface area and volume of the ice structure. The number of surveys conducted for the IN21, CH21 and CH20 AIRs were six, eight and two, respectively (see **Table 2**). The first drone flight was used to set the dome volume ( $V_{dome}$ ) for model initialisation. The remaining surveys were used for model calibration and validation. Since the Indian AIR was built on top of another ice structure (see **Figure 2**), it had a much higher dome volume compared to the other AIRs.

## 3 MODEL SETUP

A bulk energy and mass balance model is used to calculate the amounts of ice, meltwater, water vapour and wastewater of the AIR. In each hourly time step, the model uses the AIR surface area, energy balance and mass balance calculations to estimate its ice volume, surface temperature and wastewater as shown in **Figure 3**.

### 3.1 Surface Area Calculation

The model assumes the AIR shape to be a cone and assigns the following shape attributes:

$$A_{cone}^i = \pi \cdot r_{cone}^i \cdot \sqrt{(r_{cone}^i)^2 + (h_{cone}^i)^2} \quad (1a)$$

$$V_{cone}^i = \pi / 3 \cdot (r_{cone}^i)^2 \cdot h_{cone}^i \quad (1b)$$

$$j_{cone}^i = \frac{\Delta M_{ice}^i}{\rho_{water} * A_{cone}^i} \quad (1c)$$

where  $i$  denotes the model time step,  $r_{cone}^i$  is the radius;  $h_{cone}^i$  is the height;  $A_{cone}^i$  is the surface area;  $V_{cone}^i$  is the volume and  $j_{cone}^i$  is the AIR surface normal thickness change as shown in **Figure 4**.  $M_{ice}^i$  is the mass of the AIR and  $\Delta M_{ice}^i = M_{ice}^{i-1} - M_{ice}^{i-2}$ . Henceforth, the equations used display the model time step superscript  $i$  only if it is different from the current time step.

AIR volume can also be expressed as:

$$V_{cone} = \frac{M_{ice}}{\rho_{ice}} \quad (2)$$

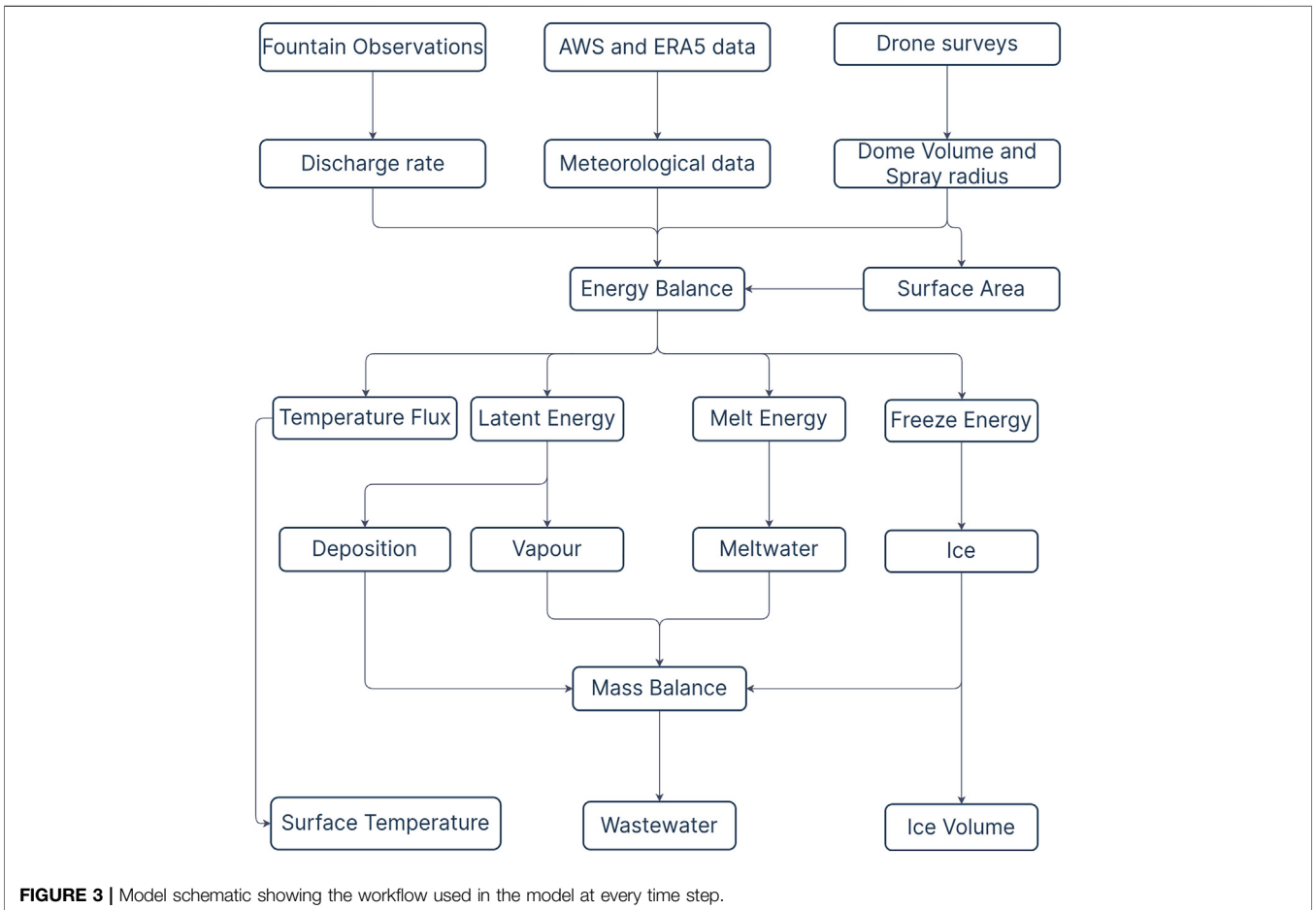


**FIGURE 3 |** Model schematic showing the workflow used in the model at every time step.

where  $\rho_{ice}$  is the density of ice ( $917 \text{ kg m}^{-3}$ ).

The initial radius of the AIR is assumed to be  $r_F$ . The initial height  $h_0$  depends on the dome volume  $V_{dome}$  used to construct the AIR as follows:

$$h_0 = \Delta x + \frac{3 \cdot V_{dome}}{\pi \cdot (r_F)^2} \quad (3)$$

where  $\Delta x$  is the surface layer thickness (defined in **Section 3.2**)

During the subsequent time steps, the dimensions of the AIR evolve assuming a uniform thickness change ( $j_{cone}$ ) across its surface area with an invariant slope  $s_{cone} = \frac{j_{cone}}{r_{cone}}$ . During these time steps, the volume is parameterised using **Eq. 1b** as:

$$V_{cone} = \frac{\pi \cdot (r_{cone})^3 \cdot s_{cone}}{3} \quad (4)$$

We define the Icestupa boundary through its spray radius, i.e. we assume ice formation is negligible when  $r_{cone} > r_F$ . Combining **Eqs 1b, 2 Eqs 3, 4, 4**, the geometric evolution of the Icestupa at each time step  $i$  can be determined by considering the following rules:

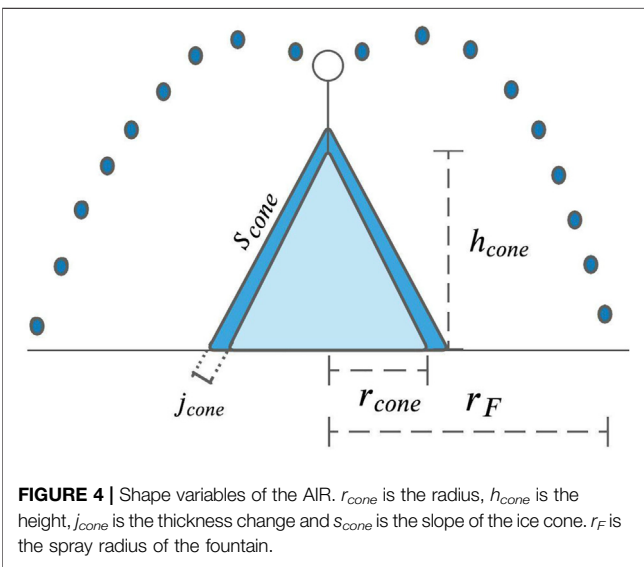
$$(r_{cone}, h_{cone}) = \begin{cases} (r_F, h_0) & \text{if } i = 0 \\ \left( r_{cone}^{i-1}, \frac{3 \cdot M_{ice}}{\pi \cdot \rho_{ice} \cdot (r_{cone}^{i-1})^2} \right) & \text{if } r_{cone}^{i-1} \geq r_F \text{ and } \Delta M_{ice} > 0 \\ \left( \frac{3 \cdot M_{ice}}{\pi \cdot \rho_{ice} \cdot s_{cone}} \right)^{1/3} \cdot (1, s_{cone}) & \text{otherwise} \end{cases} \quad (5)$$

### 3.2 Energy Balance Calculation

We approximate the energy balance at the surface of an AIR by a one-dimensional description of energy fluxes into and out of a (thin) layer with thickness  $\Delta x$ :

$$\rho_{ice} \cdot c_{ice} \cdot \frac{\Delta T}{\Delta t} \cdot \Delta x = q_{SW} + q_{LW} + q_L + q_S + q_F + q_G \quad (6)$$

Upward and downward fluxes relative to the ice surface are positive and negative, respectively. The first term is the energy change of the surface layer, which can be translated into a phase change energy should phase changes occur;  $q_{SW}$  is the net shortwave radiation;  $q_{LW}$  is the net longwave radiation;  $q_L$  and  $q_S$  are the turbulent latent and sensible heat fluxes.  $q_F$  represents the heat exchange of the fountain water droplets with the AIR ice surface.  $q_G$  represents ground heat flux between the AIR surface and its interior.



The energy flux acts upon the AIR surface layer, which has an upper and lower boundary defined by the atmosphere and the ice body of the AIR, respectively. A sensitivity analysis was later performed to understand the influence of this factor and decide its value. Here, we define the surface temperature  $T_{ice}$  to be the modelled average temperature of the icestupa surface layer.

### 3.2.1 Net Shortwave Radiation $q_{SW}$

The net shortwave radiation  $q_{SW}$  is computed as follows:

$$q_{SW} = (1 - \alpha) \cdot (SW_{direct} \cdot f_{cone} + SW_{diffuse}) \quad (7)$$

where  $SW_{direct}$  and  $SW_{diffuse}$  are the direct and diffuse shortwave radiation,  $\alpha$  is the modelled albedo and  $f_{cone}$  is the area fraction of the ice structure exposed to the direct shortwave radiation.

The albedo varies depending on the water source that formed the current AIR surface layer. During the fountain runtime, the albedo assumes a constant value corresponding to ice albedo. However, after the fountain is switched off, the albedo can reset to snow albedo during snowfall events and then decay back to ice albedo. We use the scheme described in Oerlemans and Knap (1998) to model this process. The scheme records the decay of albedo with time after fresh snow is deposited on the surface.  $\delta t$  records the number of time steps after the last snowfall event. After snowfall, albedo changes over a time step,  $\delta t$ , as

$$\alpha = \alpha_{ice} + (\alpha_{snow} - \alpha_{ice}) \cdot e^{(-\delta t)/\tau} \quad (8)$$

where  $\alpha_{ice}$  is the bare ice albedo value (0.25),  $\alpha_{snow}$  is the fresh snow albedo value (0.85) and  $\tau$  is a decay rate (16 days), which determines how fast the albedo of the ageing snow recedes back to ice albedo.

The solar area fraction  $f_{cone}$  of the ice structure exposed to the direct shortwave radiation depends on the shape considered. Using the solar elevation angle  $\theta_{sun}$ , the solar beam can be considered to have a vertical component, impinging on the

horizontal surface (semicircular base of the AIR), and a horizontal component impinging on the vertical cross section (a triangle). The solar elevation angle  $\theta_{sun}$  used is modelled using the parametrisation proposed by Woolf (1968). Accordingly,  $f_{cone}$  is determined as follows:

$$f_{cone} = \frac{(0.5 \cdot r_{cone} \cdot h_{cone}) \cdot \cos \theta_{sun} + (\pi \cdot (r_{cone})^2 / 2) \cdot \sin \theta_{sun}}{\pi \cdot r_{cone} \cdot ((r_{cone})^2 + (h_{cone})^2)^{1/2}} \quad (9)$$

The diffuse shortwave radiation is assumed to impact the conical AIR surface uniformly.

### 3.2.2 Net Longwave Radiation $q_{LW}$

The net longwave radiation  $q_{LW}$  is determined as follows:

$$q_{LW} = LW_{in} - \sigma \cdot \epsilon_{ice} \cdot (T_{ice} + 273.15)^4 \quad (10)$$

where  $T_{ice}$  is the modelled surface temperature given in [°C],  $\sigma = 5.67 \cdot 10^{-8} \text{ J m}^{-2} \text{s}^{-1} \text{K}^{-4}$  is the Stefan-Boltzmann constant,  $LW_{in}$  denotes the incoming longwave radiation and  $\epsilon_{ice}$  is the corresponding emissivity value for the Icestupa surface (0.97).

The incoming longwave radiation  $LW_{in}$  for the Indian site, where no direct measurements were available, is determined as follows:

$$LW_{in} = \sigma \cdot \epsilon_a \cdot (T_a + 273.15)^4 \quad (11)$$

here  $T_a$  represents the measured air temperature and  $\epsilon_a$  denotes the atmospheric emissivity. We approximate the atmospheric emissivity  $\epsilon_a$  using the equation suggested by Brutsaert (1982), considering air temperature and vapor pressure (Eqn. 12). The vapor pressure of air over water and ice was obtained using Eq. (15). The expression defined in Brutsaert (1975) for clear skies (first term in equation 12) is extended with the correction for cloudy skies after Brutsaert (1982) as follows:

$$\epsilon_a = 1.24 \cdot \left( \frac{P_{v,w}}{(T_a + 273.15)} \right)^{1/7} \cdot (1 + 0.22 \cdot cld^2) \quad (12)$$

with a cloudiness index  $cld$ , ranging from 0 for clear skies to 1 for complete overcast skies. For the Indian site, we assume cloudiness to be negligible.

### 3.2.3 Turbulent Fluxes

The turbulent sensible  $q_s$  and latent heat  $q_L$  fluxes are computed with the following expressions proposed by Garratt (1992):

$$q_s = \mu_{cone} \cdot c_a \cdot \rho_a \cdot p_a / p_{0,a} \cdot \frac{\kappa^2 \cdot v_a \cdot (T_a - T_{ice})}{(\ln \frac{h_{AWS}}{z_0})^2} \quad (13)$$

$$q_L = \mu_{cone} \cdot 0.623 \cdot L_s \cdot \rho_a / p_{0,a} \cdot \frac{\kappa^2 \cdot v_a (P_{v,w} - P_{v,ice})}{(\ln \frac{h_{AWS}}{z_0})^2} \quad (14)$$

where  $h_{AWS}$  is the measurement height above the ground surface of the AWS (around 2 m for all sites),  $v_a$  is the wind speed in [ $m s^{-1}$ ],  $c_a$  is the specific heat of air at constant pressure ( $1010 \text{ J kg}^{-1} \text{K}^{-1}$ ),  $\rho_a$  is the air density at standard sea level ( $1.29 \text{ kg m}^{-3}$ ),  $p_{0,a}$  is the air pressure at standard sea level

(1013 hPa),  $p_a$  is the measured air pressure,  $\kappa$  is the von Karman constant (0.4),  $z_0$  is the surface roughness (3 mm) and  $L_s$  is the heat of sublimation (2848 kJ kg<sup>-1</sup>). The vapor pressure of air with respect to water ( $p_{v,w}$ ) and with respect to ice ( $p_{v,ice}$ ) was obtained using the formulation given in Huang (2018) :

$$\begin{aligned} p_{v,w} &= e^{\frac{(34.494 - \frac{6924.99}{T_a + 25.7})}{(T_a + 105)^{1.5} \cdot 100}} \cdot \frac{RH}{100} \\ p_{v,ice} &= e^{\frac{(43.494 - \frac{6545.89}{T_{ice} + 278})}{(T_{ice} + 868)^2 \cdot 100}} \end{aligned} \quad (15)$$

The dimensionless parameter  $\mu_{cone}$  is an exposure parameter that deals with the fact that AIR has a rough appearance and forms an obstacle to the wind regime. This factor accounts for the larger turbulent fluxes due to the roughness of the surface (Oerlemans et al., 2021), and is a function of the AIR slope as follows:

$$\mu_{cone} = 1 + \frac{s_{cone}}{2} \quad (16)$$

A possible source of error is the fact that wind measurements from the horizontal plane at the AWS are used, which might be different from those on a slope. However, without detailed datasets from the AIR surface, we retain this assumption.

### 3.2.4 Fountain Discharge Heat Flux $q_F$

The fountain water, at temperature  $T_F$ , is assumed to cool to 0 °C. Thus, the heat flux caused by this process is:

$$q_F = \frac{\Delta M_F \cdot c_{water} \cdot T_F}{\Delta t \cdot A_{cone}} \quad (17)$$

with  $c_{water}$  as the specific heat of water (4186 J kg<sup>-1</sup> K<sup>-1</sup>).

### 3.2.5 Bulk Icestupa Heat Flux $q_G$

The bulk Icestupa heat flux  $q_G$  corresponds to the ground heat flux in normal soils and is caused by the temperature gradient between the surface layer ( $T_{ice}$ ) and the ice body ( $T_{bulk}$ ). It is expressed by using the heat conduction equation as follows:

$$q_G = k_{ice} \cdot (T_{bulk} - T_{ice}^{i-1}) / l_{cone} \quad (18)$$

where  $k_{ice}$  is the thermal conductivity of ice (2.123 W m<sup>-1</sup> K<sup>-1</sup>),  $T_{bulk}$  is the mean temperature of the ice body within the icerupa and  $l_{cone}$  is the average distance of any point in the surface to any other point in the ice body.  $T_{bulk}$  is initialised as 0 °C and later determined from Eq. 18 as follows:

$$T_{bulk}^{i+1} = T_{bulk} - (q_G \cdot A \cdot \Delta t) / (M_{ice} \cdot c_{ice}) \quad (19)$$

Since AIRs typically have conical shapes with  $r_{cone} > h_{cone}$ , we assume that the center of mass of the cone body is near the base of the fountain. Thus, the distance of every point in the AIR surface layer from the cone body's center of mass is between  $h_{cone}$  and  $r_{cone}$ . Therefore, we calculate  $q_G$  assuming  $l_{cone} = (r_{cone} + h_{cone})/2$ .

### 3.2.6 Phase Changes

In this section, the numerical procedures to model phase changes at the surface layer are explained. Let  $T_{temp}$  be the calculated surface temperature. Therefore, Eq. (6) can be rewritten as:

$$q_{total} = \rho_{ice} \cdot c_{ice} \cdot \frac{(T_{temp} - T_{ice})}{\Delta t} \cdot \Delta x$$

where  $q_{total}$  represents the total energy available to be redistributed. Even if the numerical heat transfer solution produces temperatures which are  $T_{temp} > 0^\circ\text{C}$ , say from intense shortwave radiation, the ice temperature must remain at  $T_{temp} = 0^\circ\text{C}$ . The "excess" energy is used to drive the melting process. Moreover, the energy input is used to melt the surface ice layer, and not to raise the surface temperature to some unphysical value. Similarly, for freezing to occur, three conditions are required. Firstly, fountain water is present ( $\Delta M_F > 0$ ) and secondly the calculated temperature of the ice,  $T_{temp}$ , is below 0 °C. However, these two conditions are not sufficient as the latent heat turbulent fluxes can only contribute to temperature fluctuations. Therefore, an additional condition, namely,  $(q_{total} - q_L) < 0$ , is required. Depending on the above conditions, the total energy  $q_{total}$  can be redistributed for the melting ( $q_{melt}$ ), freezing ( $q_{freeze}$ ) and surface temperature change ( $q_T$ ) processes as follows:

$$q_{total} = \begin{cases} q_{freeze} + q_T & \text{if } \Delta M_F > 0 \text{ and } T_{temp} < 0 \text{ and } (q_{total} - q_L) < 0 \\ q_{melt} + q_T & \text{otherwise} \end{cases} \quad (20)$$

Henceforth, time steps when the total energy is redistributed to the freezing energy are called freezing events and the rest of the time steps are called melting events.

During a freezing event, the AIR surface is assumed to warm to 0 °C. The available energy ( $q_{total} - q_L$ ) is further increased due to this change in surface temperature represented by the energy flux:

$$q_0 = \frac{\rho_{ice} \cdot \Delta x \cdot c_{ice} \cdot T_{ice}^{i-1}}{\Delta t}$$

The available fountain discharge ( $\Delta M_F$ ) may not be sufficient to utilize all the freezing energy. At such times, the additional freezing energy further cools down the surface temperature. Accordingly, the surface energy flux distribution during a freezing event can be represented as:

$$(q_{freeze}, q_T) = \begin{cases} \left( \frac{(\Delta M_F \cdot L_f)}{A_{cone} \cdot \Delta t}, q_{total} + \frac{\Delta M_F \cdot L_f}{A_{cone} \cdot \Delta t} \right) & \text{if } \Delta M_F \text{ insufficient} \\ (q_{total} - q_L + q_0, q_L - q_0) & \text{otherwise} \end{cases} \quad (21)$$

If  $T_{temp} > 0^\circ\text{C}$ , then energy is reallocated from  $q_T$  to  $q_{melt}$  to maintain surface temperature at melting point. The total energy flux distribution during a melting event can be represented as:

$$(q_{melt}, q_T) = \begin{cases} (0, q_{total}) & \text{if } T_{temp} \leq 0 \\ \left( \frac{T_{temp} \cdot \rho_{ice} \cdot c_{ice} \cdot \Delta x}{\Delta t}, q_{total} - \frac{T_{temp} \cdot \rho_{ice} \cdot c_{ice} \cdot \Delta x}{\Delta t} \right) & \text{if } T_{temp} > 0 \end{cases} \quad (22)$$

### 3.3 Mass Balance Calculation

The mass balance equation for an AIR is represented as:

$$\frac{\Delta M_F + \Delta M_{ppt} + \Delta M_{dep}}{\Delta t} = \frac{\Delta M_{ice} + \Delta M_{water} + \Delta M_{sub} + \Delta M_{waste}}{\Delta t} \quad (23)$$

where  $M_F$  is the cumulative mass of the fountain discharge;  $M_{ppt}$  is the cumulative precipitation;  $M_{dep}$  is the cumulative accumulation through water vapour deposition;  $M_{ice}$  is the cumulative mass of ice;  $M_{water}$  is the cumulative mass of melt water;  $M_{sub}$  represents the cumulative water vapor loss by sublimation and  $M_{waste}$  represents the fountain wastewater that did not interact with the AIR. The left hand side of Eq. 23 represents the rate of mass input and the right hand side represents the rate of mass output for an AIR.

Precipitation input is calculated as shown in Eq. 24b where  $\rho_w$  is the density of water ( $1000 \text{ kg m}^{-3}$ ),  $\Delta ppt/\Delta t$  is the measured precipitation rate in [ $\text{m s}^{-1}$ ] and  $T_{ppt}$  is the temperature threshold below which precipitation falls as snow. Here, snowfall events were identified using  $T_{ppt}$  as  $1^\circ\text{C}$ . Snow mass input is calculated by assuming a uniform deposition over the entire circular footprint of the AIR.

The latent heat flux is used to estimate either the evaporation and condensation processes or sublimation and deposition processes as shown in Equation (24c). During the time steps at which the surface temperature is below  $0^\circ\text{C}$  only sublimation and deposition can occur, but if the surface temperature reaches  $0^\circ\text{C}$ , evaporation and condensation can also occur. As the differentiation between evaporation and sublimation (and condensation and deposition) when the air temperature reaches  $0^\circ\text{C}$  is challenging, we assume that negative (positive) latent heat fluxes correspond only to sublimation (deposition), i.e. no evaporation (condensation) is calculated.

Since we have categorized every time step as a freezing or melting event, we can determine the melting/freezing rates and the corresponding meltwater/ice quantities as shown in Eqs 24e, 24d, and 24f. Having calculated all other mass components, the fountain wastewater generated every time step can be calculated using Eq. 23.

$$\frac{\Delta M_F}{\Delta t} = \begin{cases} \frac{60}{\rho_w \cdot \Delta t} \cdot d_F & \text{if fountain is on} \\ 0 & \text{otherwise} \end{cases} \quad (24a)$$

$$\frac{\Delta M_{ppt}}{\Delta t} = \begin{cases} \pi \cdot (r_{cone})^2 \cdot \rho_w \cdot \frac{\Delta ppt}{\Delta t} & \text{if } T_a < T_{ppt} \\ 0 & \text{if } T_a \geq T_{ppt} \end{cases} \quad (24b)$$

$$\left( \frac{\Delta M_{dep}}{\Delta t}, \frac{\Delta M_{sub}}{\Delta t} \right) = \begin{cases} \frac{q_L \cdot A_{cone}}{L_s} \cdot (1, 0) & \text{if } q_L \geq 0 \\ \frac{q_L \cdot A_{cone}}{L_s} \cdot (0, -1) & \text{if } q_L < 0 \end{cases} \quad (24c)$$

$$\frac{\Delta M_{water}}{\Delta t} = \frac{q_{melt} \cdot A_{cone}}{L_f} \quad (24d)$$

$$\frac{\Delta M_{freeze/melt}}{\Delta t} = \frac{q_{freeze/melt} \cdot A_{cone}}{L_f} \quad (24e)$$

$$\frac{\Delta M_{ice}}{\Delta t} = \frac{q_{freeze} \cdot A_{cone}}{L_f} + \frac{\Delta M_{ppt}}{\Delta t} + \frac{\Delta M_{dep}}{\Delta t} - \frac{\Delta M_{sub}}{\Delta t} - \frac{\Delta M_{water}}{\Delta t} \quad (24f)$$

Considering AIRs as water reservoirs, their net water loss can be defined as:

$$\text{Net water losses} = \frac{M_{waste} + M_{sub}}{(M_F + M_{ppt} + M_{dep})} \cdot 100 \quad (25)$$

### 3.4 Uncertainty Quantification

The uncertainty in the model of estimating ice volumes is caused by three sources, namely, model forcing data, model hyperparameters and model parameters. Model forcing data can further be divided into weather and fountain forcing data. Significant uncertainty exists in the weather forcing data, particularly for all the radiation measurements ( $SW_{direct}$ ,  $SW_{diffuse}$ ,  $LW_{in}$ ) since they were taken from ERA5 dataset or an AWS far away from the construction sites. Since no other weather datasets exist for comparison, especially near the IN21 AIR, we are not accounting for uncertainties related to meteorological forcing data in this analysis. Uncertainty in the fountain forcing data arises due to only some fountain parameters listed in Table 3. Fountain runtime  $t_F$  has no uncertainty for the Swiss AIRs because no interruptions occurred during the study period. However, significant uncertainty exists for the IN21 AIR, where the interruptions due to pipeline freezing events happened overnight but this was ignored in this analysis. Fountain spray radius  $r_F$  was measured using the drone survey and therefore also doesn't contribute to model uncertainty. The choice of mean discharge rate  $d_F$  for both sites was just a best guess, based on few observations made by the flowmeter. So we associate this parameter by a large uncertainty of  $\pm 50\%$ . For the fountain water temperature  $T_F$ , we assumed an upper bound of  $3^\circ\text{C}$  since it is unlikely for it to have been beyond this range considering winter conditions at all the sites. The model structure introduces uncertainty through the spatial and temporal hyperparameters  $\Delta x$  and  $\Delta t$ . By definition,  $\Delta x$  is directly proportional to  $\Delta t$ . Therefore, we fix the temporal resolution of the model at hourly timesteps and only investigate the uncertainty caused by  $\Delta x$  here. Since the surface layer thickness for an AIR does not resemble to any parameter in the glaciological literature, we attribute a wide range of values for it (from 1 to 10 cm). The model parameters are henceforth called as weather parameters to distinguish them from the fountain forcing parameters. These were fixed within a range based on literature values (see Table 3).

The three types of uncertain parameters namely, model hyperparameters ( $\Delta x$ ), fountain forcing parameters ( $d_F$ ,  $T_F$ ) and weather parameters ( $\epsilon_{ice}$ ,  $z_0$ ,  $\alpha_{ice}$ ,  $\alpha_{snow}$ ,  $T_{ppb}$ ,  $\tau$ ) are denoted as  $Q^M$ ,  $Q^F$  and  $Q^W$  henceforth. Together, these nine parameters cause a large uncertainty in the ice volume estimates. In order to reduce this uncertainty, we perform a global sensitivity analysis with the net water loss as our objective. The objective of this sensitivity analysis was to reduce the dimension of the parameter space by calibrating the parameters with high total-order sensitivities ( $S_{T_j} > 0.5$ ). The methodology to determine  $S_{T_j}$  is described in Supplementary Appendix 7.3. These sensitive model parameters were calibrated based on the root mean squared error (RMSE) between the drone

**TABLE 3 |** Free parameters in the model categorised as constant, derived, model hyperparameters, weather and fountain forcing parameters with their respective values/ranges.

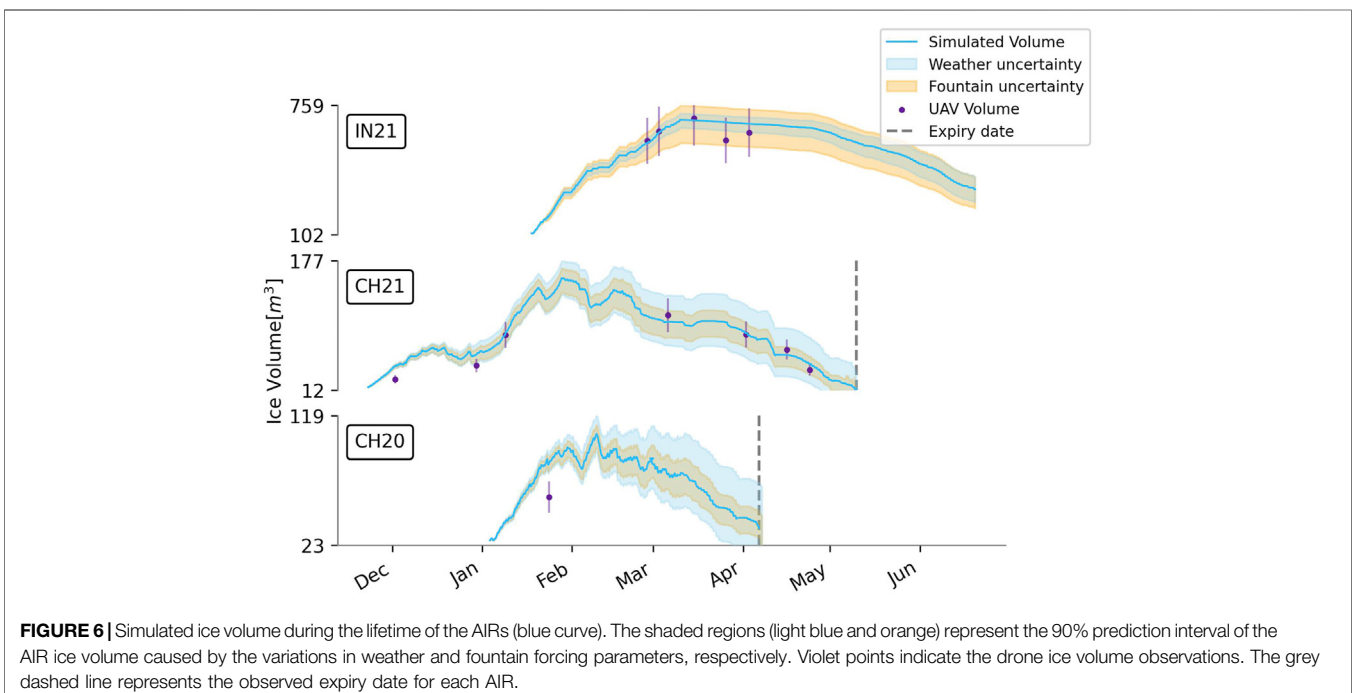
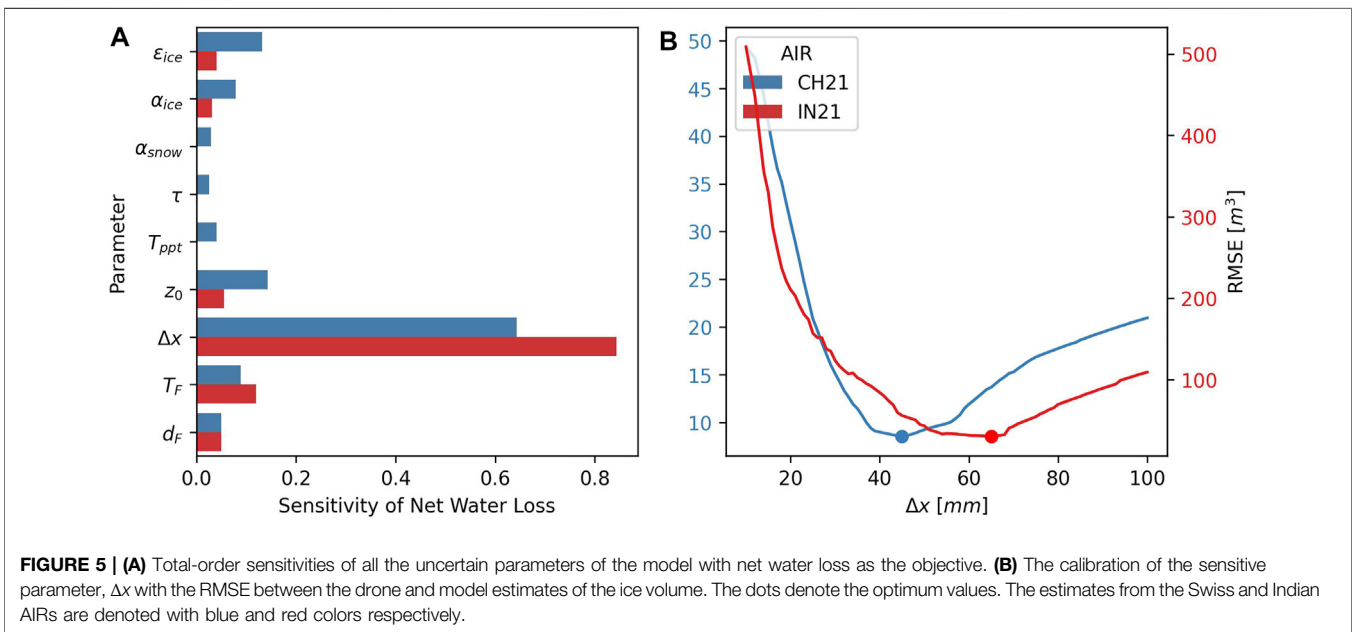
Constant parameters	Symbol	Value	Unit	References
Van Karman constant	$\kappa$	0.4	dimensionless	Cuffey and Paterson (2010)
Stefan Boltzmann constant	$\sigma$	$5.67 \times 10^{-8}$	$W m^{-2} K^{-4}$	Cuffey and Paterson (2010)
Air pressure at sea level	$p_{0,a}$	1013	hPa	Mölg and Hardy (2004)
Density of water	$\rho_w$	1000	$kg m^{-3}$	Cuffey and Paterson (2010)
Density of ice	$\rho_{ice}$	917	$kg m^{-3}$	Cuffey and Paterson (2010)
Density of air	$\rho_a$	1.29	$kg m^{-3}$	Mölg and Hardy (2004)
Specific heat of water	$c_w$	4186	$J kg^{-1} ^\circ C^{-1}$	Cuffey and Paterson (2010)
Specific heat of ice	$c_{ice}$	2097	$J kg^{-1} ^\circ C^{-1}$	Cuffey and Paterson (2010)
Specific heat of air	$c_a$	1010	$J kg^{-1} ^\circ C^{-1}$	Mölg and Hardy (2004)
Thermal conductivity of ice	$k_{ice}$	2.123	$W m^{-1} K^{-1}$	Bonales et al. (2017)
Latent Heat of Sublimation	$L_s$	$2.85 \times 10^6$	$J kg^{-1}$	Cuffey and Paterson (2010)
Latent Heat of Fusion	$L_f$	$3.34 \times 10^5$	$J kg^{-1}$	Cuffey and Paterson (2010)
Gravitational acceleration	$g$	9.81	$m s^{-2}$	Cuffey and Paterson (2010)
Weather station height	$h_{AWS}$	2	m	assumed
Model timestep	$\Delta t$	3600	s	assumed
Fountain spray radius	$r_F$		m	measured
Fountain runtime	$t_F$		hours	measured
Derived Parameters	Symbol		Unit	Section
Radius of AIR	$r_{cone}$		m	3.1
Height of AIR	$h_{cone}$		m	3.1
Slope of AIR	$s_{cone}$		dimensionless	3.1
Thickness change of AIR	$j_{cone}$		m	3.1
Atmospheric emissivity	$\epsilon_a$		dimensionless	3.2.2
Cloudiness	$cl_d$		dimensionless	assumed
Vapour pressure over water	$p_{v,w}$		hPa	3.2.3
Vapour pressure over ice	$p_{v,ice}$		hPa	3.2.3
Solar elevation angle	$\theta_{sun}$		°	3.2.1
Albedo	$\alpha$		dimensionless	3.2.1
Solar area fraction	$f_{cone}$		dimensionless	3.2.1
Ice body and surface distance	$l_{cone}$		m	3.2.5
AIR surface temperature	$T_{ice}$		°C	3.2.5
AIR bulk temperature	$T_{bulk}$		°C	3.2.5
Model Hyperparameters	Symbol	Range	Unit	References
Surface layer thickness	$\Delta x$	[1e - 2, 1e - 1]	m	assumed
Weather Parameters	Symbol	Range	Unit	References
Ice Emissivity	$\epsilon_{ice}$	[0.95, 0.99]	dimensionless	Hori et al. (2006)
Surface Roughness	$Z_0$	[1e - 3, 5e - 3]	m	Brock et al. (2006)
Ice Albedo	$\alpha_{ice}$	[0.15, 0.35]	dimensionless	Steiner et al. (2015)
Snow Albedo	$\alpha_{snow}$	[0.8, 0.9]	dimensionless	Zolles et al. (2019)
Precipitation Temperature threshold	$T_{ppt}$	[0, 2]	°C	Zhou et al. (2010)
Albedo Decay Rate	$\tau$	[10, 22]	days	Schmidt et al. (2017)
Oerlemans and Knap (1998)				
Fountain Forcing Parameters	Symbol	Range	Unit	References
Discharge rate	$d_F$	$[0.5 \cdot d_F, 1.5 \cdot d_F]$	l/min	assumed
Water temperature	$T_F$	[0, 3]	°C	assumed

surveys (see **Table 2**) and the model estimations of the ice volume. For this calibration procedure, all the other parameters were set to the median value of their respective ranges defined in **Table 3**. The sensitivity analysis and calibration were carried out with the drone surveys of CH21 and IN21 AIRs.

The model uncertainty was quantified separately for the remaining parameters in  $Q^M$ ,  $Q^F$  and  $Q^W$  using the corresponding 90 % prediction interval  $I^M$ ,  $I^F$  and  $I^W$ . The 90 % prediction interval,  $I^k$ ,

gives us the interval within which 90 % of the ice volume outcomes occur when all the parameters in  $Q^k$  are varied assuming each has an independent uniform probability density function. 5 % of the outcomes are above and 5 % are below this interval. The methodology to obtain this is described in **Supplementary Appendix 7.3**.

For validation, the calibrated model was tested with two datasets namely, the expiry date of all AIRs and the drone surveys of CH20 AIR.



## 4 RESULTS

### 4.1 Calibration of Sensitive Parameters

The total-order sensitivities of all the nine parameters with respect to the net water loss objective are shown in **Figure 5A**. In total, the global sensitivity analysis required 1432 model runs to determine these sensitivities for each site. The only sensitive parameter ( $S_{T_j} > 0.5$ ) for both AIRs was the surface layer thickness. The RMSE between the drone surveys and the model ice volume estimates for different surface layer thickness are shown in **Figure 5B**. The optimum value of  $\Delta x$  was

found to be 45 and 65 mm with an RMSE of 9 m<sup>3</sup> and 30 m<sup>3</sup> for CH21 and IN21 AIRs respectively.

### 4.2 Weather and Fountain Forcing Uncertainty Quantification

The uncertainty in the ice volume estimates caused by the weather and fountain forcing parameters are shown in **Figure 6**. The ranges highlighted represent the corresponding 90 % prediction interval of the ice volume estimates. Weather

uncertainty determination required 422 simulations whereas fountain forcing uncertainty determination required 32 simulations for each AIR. Since the results presented below differ significantly during the fountain runtime, we divided the simulation duration of the AIR into accumulation and ablation periods. The accumulation (ablation) period ends (starts) at the last fountain discharge event.

The prediction interval of the weather and fountain forcing parameters behave differently during the accumulation and ablation period for all AIRs. Prediction interval of the weather parameters increase throughout the simulation period, but that of the fountain forcing parameters only increase during the accumulation period. This is to be expected since the fountain forcing parameters directly affect the model estimates only during the accumulation period.

Weather uncertainty for the Indian site was low compared to the Swiss since precipitation and the associated variation in albedo was negligible. At the end of the accumulation period, the Indian weather prediction interval had a magnitude of  $73 \text{ m}^3$  which was 10 % of the maximum simulated volume, whereas the magnitude of the Swiss weather prediction interval was much higher (28 % of the maximum simulated volume for the CH21 AIR). This was expected since four out of the six uncertain Indian weather parameters were part of the albedo module. Among all the weather parameters, surface roughness caused the most variance in both Indian and the Swiss ice volume estimates.

Fountain forcing uncertainty for the Indian site was higher than its weather uncertainty (28 % of the maximum simulated volume at the end of the accumulation period). This was predominantly due to the uncertainty in the fountain's water temperature. However, for the Swiss site, the prediction interval of the fountain forcing parameters was similar to that of the weather parameters during the accumulation period. Since the mean fountain discharge rate of the Indian location was eight times that of the Swiss, the uncertainty due to the fountain forcing parameters was expected to be larger for the Indian location.

### 4.3 Validation

Model performance can be judged based on the ice volume left on the expiry date of all AIRs. In the case of CH21 AIR no ice volume was left whereas for CH20 AIR ice volume of  $12 \text{ m}^3$  was left on the expiry date. For the IN21 AIR, the determination of the expiry date was not possible. In reality, the IN21 AIR was found to have disintegrated into several ice blocks on 20th June 2021.

There was also one drone survey of the CH20 AIR volume for validation purposes (see Table 2). The RMSE of that observation with the modelled volume was  $19 \text{ m}^3$  which is 18 % of the maximum simulated ice volume of CH20 AIR.

### 4.4 AIR Ice Volume Estimates

Since this model used a surface energy balance model commonly applied on glaciers, we analyse the AIR temporal and spatial variation similar to how it is done for a glacier. Particularly, we used the AIR surface normal thickness change ( $j_{cone}$ ) as a measure to quantify the location influence. Note that  $j_{cone}$  is

similar to the "specific mass balance" of a glacier with units *m w.e.*. The thickness change during the accumulation and ablation period was referred to as thickness growth and decay, respectively.

The construction decisions responsible for the observed magnitude and variance of the ice volume estimates can be categorised based on the fountain used and the location selected. According to Eq. 24e, the freezing/melting rate of the AIRs can be decomposed to the corresponding freezing/melting energy and the surface area. The construction location chosen determines the thickness growth/decay through the freezing/melting energy flux and the fountain determines the surface area through its spray radius.

The influence of location can be further comprehended if we analyse the daily surface normal thickness change together with the corresponding energy fluxes. Figure 7 shows the daily thickness and energy balance components calculated with the calibrated surface layer thickness for the first and last 20 days for each AIR. The two time periods selected were characteristic of the accumulation and ablation period, respectively. A strong variability was evident between the accumulation and ablation periods and between the CH21 and the IN21 AIRs.

The daily mean thickness change of the Indian location was positive ( $3 \text{ mm w.e.}$ ) with a daily mean growth of  $31 \text{ mm w.e.}$  and a mean decay of  $11 \text{ mm w.e.}$  In the Swiss location, the daily mean thickness change was negative ( $-4 \text{ mm w.e.}$ ) with a daily mean thickness growth of  $8 \text{ mm w.e.}$  and a mean decay of  $18 \text{ mm w.e.}$  The difference in magnitude between the growth and the decay corresponds to the difference between the freezing and the melting energy balance components. For the Indian site,  $q_{freeze}$  accounted for 73 %,  $q_{melt}$  accounted for 23 % and  $q_T$  just 4 % of overall energy turnover. The energy turnover is calculated as the sum of energy fluxes in absolute values. For the Swiss site,  $q_{freeze}$  accounted for 37 %,  $q_{melt}$  accounted for 61 % and  $q_T$  just 2 % of overall energy turnover. The freezing events occurred for 19 and 34% of the simulation duration (see Table 1) for the Indian and Swiss sites, respectively. The accumulation period is characteristic of these freezing events and the ablation period is characteristic of the melting events. We compare the energy turnover of different energy fluxes between these two periods to quantify the influence of different surface processes.

To understand the overall impact of the radiation fluxes (longwave and shortwave) and the turbulent fluxes (sensible and latent) on the freezing and melting energies, we sum their respective energy turnover by taking into account the sign of their mean energy during the accumulation/ablation period (see Table 4). A negative sign indicates that the corresponding energy flux increased/decreased the freezing/melting energy respectively. Note that all energy fluxes maintain the same sign for both accumulation and ablation periods for the Indian location, but the latent heat changes sign for the Swiss location. The radiation fluxes contributed -27 and 0 % to the freezing and melting energies for the Indian location and -20 % and -6 % to the Swiss location, respectively. Similarly, the turbulent fluxes at the Indian location contribute -11 and 10 % and at the Swiss location contribute 12 and 49% respectively. Therefore, the

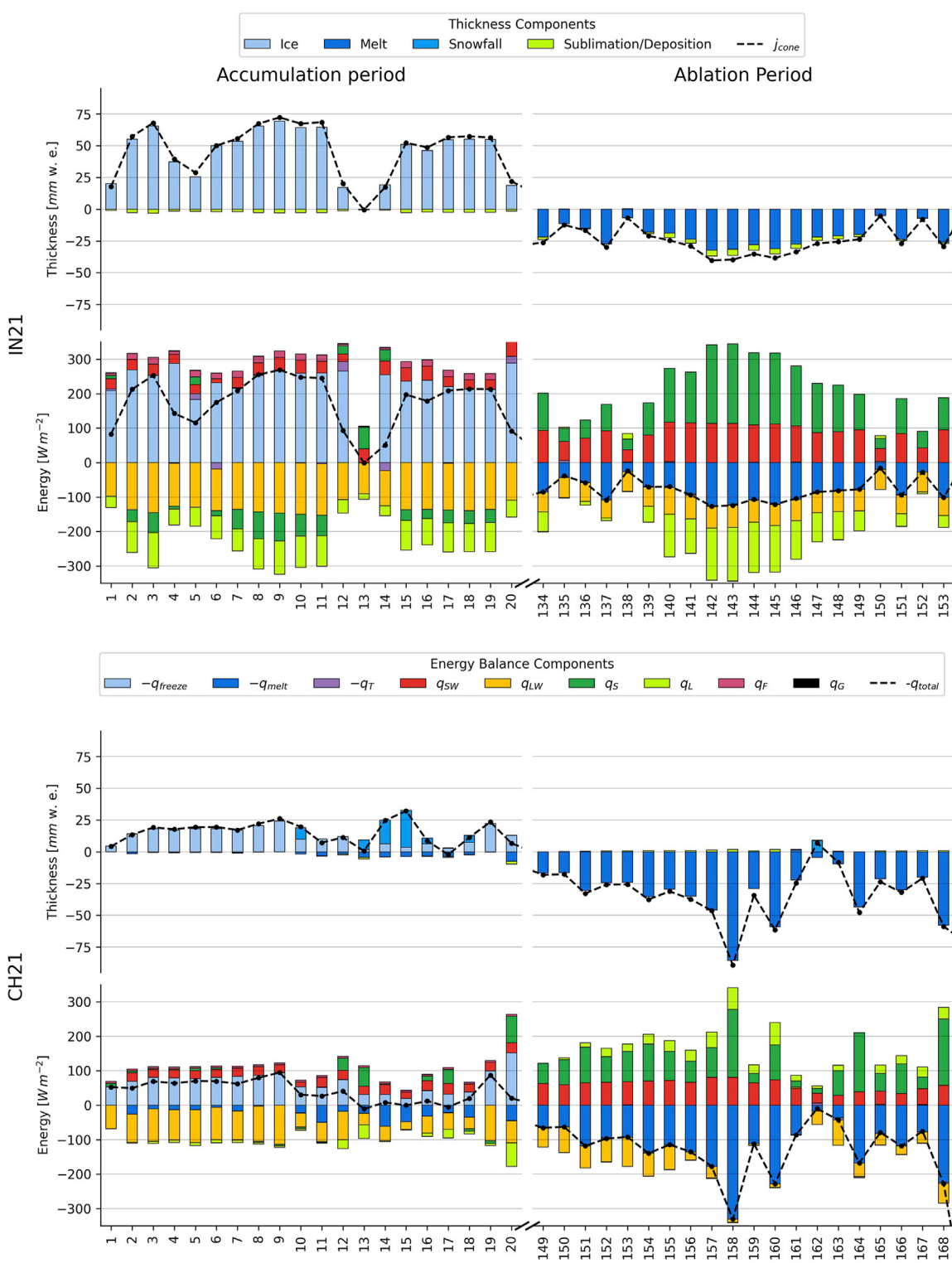


**FIGURE 7 |** Daily averages of thickness and energy balance components for the Indian and Swiss AIRs during the first 20 days of the accumulation and the last 20 days of the ablation period respectively.

AIR thickness growth was driven by the net radiation fluxes and the AIR thickness decay was driven by the net turbulent fluxes.

The longwave radiation flux had the highest energy turnover during the accumulation period for both locations. It increased and decreased the freezing and melting energy balance

components during the accumulation and ablation period, respectively. However, its magnitude was much lower in the ablation period compared to the accumulation period since the rising air temperature increased the incoming longwave radiation in the ablation period. The mean longwave radiation flux (see **Table 4**) was lower for the Indian site as its incoming longwave radiation was strongly reduced due to cloud free skies. (see **Table 1**).

Global shortwave radiation was around two times higher for the Indian location due to its higher altitude and lower latitude. However, the energy turnover of the shortwave radiation for both sites were similar (see **Table 4**). The main cause of this is the differential exposure of a conical structure to direct and diffuse fractions of global shortwave radiation. This effect is quantified by the area fraction parameter  $f_{cone}$ . Less than 20 % of the AIR surface area on average was exposed to direct shortwave radiation flux for both locations. Cloudy days increase the diffuse fraction of global shortwave radiation. Therefore, the net shortwave radiation impact for the Indian site was significantly reduced as the study period had mostly clear days. Since the Swiss site had many cloudy days, its higher diffuse shortwave radiation enhanced the net shortwave radiation impact (see **Table 1**). Temporal variation in the  $f_{cone}$  factor due to increasing solar elevation angle and decreasing AIR slope leads to higher shortwave radiation in the ablation period compared to the accumulation period. Albedo, on the other hand, only varied temporally for the Swiss location because there was no precipitation for the Indian site.

Turbulent fluxes play an essential role in the energy balance. Sensible heat fluxes had the highest energy turnover during the ablation period for both locations. It decreased and increased the freezing and melting energy balance components respectively. The Indian location had a much higher sensible heat due to higher wind speeds and higher temperature gradient between the AIR surface and the atmosphere. The sensible heat contributes much more to the energy turnover during ablation period than the latent heat flux due to rising air temperature. Alternatively, latent heat flux does not vary much in energy turnover between the accumulation and ablation periods. For the Indian site, latent heat flux increased and decreased the freezing and melting energy, since sublimation was favoured throughout the simulation duration. On the contrary, for the Swiss location, latent heat increased both the freezing and the melting energy, as sublimation and deposition were favoured during the accumulation and ablation periods, respectively.

The mass contribution of the sublimation/deposition process (shown in **Table 5**) was significantly smaller than the energy flux contribution of this process (shown in **Table 4**), since the heat of vaporization is around nine times higher than the heat of fusion. The magnitude of the sublimation/deposition process was significantly different for both AIRs: IN21 AIR lost 2 % of its mass input to sublimation compared to the 1 % mass loss of CH21 AIR (see **Table 5**). For the IN21 AIR, the mass gain due to deposition was an order of magnitude smaller than the mass loss due to sublimation. For the CH21 AIR, there were no significant differences between the mass lost by sublimation and the mass gained by deposition. This was expected, since glaciers near the

**TABLE 4 |** Contribution of the energy balance components (EBC) to the total energy turnover (the sum of energy fluxes in absolute values) during the accumulation and ablation periods with their daily mean ( $\mu$ ) and standard deviation ( $\sigma$ ) for each site. The positive/negative sign is indicative of the upward/downward direction of the mean energy flux during the respective period.

	EBC	Accumulation	Ablation	$\mu \pm \sigma$
IN21	$q_{SW}$	16 %	25 %	$65 \pm 99 W m^{-2}$
	$q_{LW}$	-43 %	-25 %	$-89 \pm 27 W m^{-2}$
	$q_S$	13 %	30 %	$63 \pm 73 W m^{-2}$
	$q_L$	-24 %	-20 %	$-63 \pm 62 W m^{-2}$
	$q_F$	4 %	0 %	$4 \pm 7 W m^{-2}$
	$q_G$	0 %	0 %	$1 \pm 1 W m^{-2}$
CH21	$q_{SW}$	21 %	23 %	$38 \pm 58 W m^{-2}$
	$q_{LW}$	-41 %	-29 %	$-60 \pm 32 W m^{-2}$
	$q_S$	23 %	39 %	$47 \pm 99 W m^{-2}$
	$q_L$	-11 %	10 %	$-6 \pm 40 W m^{-2}$
	$q_F$	3 %	0 %	$3 \pm 3 W m^{-2}$
	$q_G$	0 %	0 %	$0 \pm 1 W m^{-2}$

IN21 location have been hypothesized to lose a significant amount of their mass through sublimation, as suggested by Azam et al. (2018).

The fountain had some influence on the energy fluxes through its water temperature, temperature forcing and albedo forcing. However, this influence was insignificant compared to its influence on the surface area which was directly proportional to the fountain's spray radius during the accumulation period. Therefore, the thickness growth was uniformly scaled to produce the corresponding ice volume. Additionally, the higher spray radius of the Indian fountain resulted in a higher maximum ice volume. Nonetheless, this was accompanied by an earlier expiry date, as a larger surface area increased both the freezing and the melting rate.

## 5 DISCUSSION

### 5.1 Model Limitations

#### 5.1.1 Fountain Quantification

The model requires the fountain spray radius to be provided as input. This is a significant limitation since the model is very sensitive to the spray radius parameter. Moreover,  $r_F$  is not only determined by the fountain characteristics but also due to refreezing and melting events across the AIR perimeter. Therefore, the same fountain may produce different spray radius under different weather conditions.

Contrary to our model assumptions, the parameters used to define the fountain were not independent. The fountain height, fountain aperture diameter (both ignored in this analysis), discharge rate, water temperature and spray radius were related through the trajectories of the water droplets. Particularly, the temporal variation of both the spray radius and the water temperature were completely ignored in the model. During the IN21 experiment, snow formation was observed, indicating that the fountain water droplets have the potential to freeze before deposition on the AIR surface. Modelling such processes would require modelling the conduction, convection and nucleation processes that all droplets undergo during their flight time. Therefore, a proper quantification of the fountain is

**TABLE 5 |** Summary of the mass balance and AIR characteristics estimated at the end of the respective simulation duration.

	Name	Symbol	IN21	CH21	Units
Input	Fountain discharge	$M_F$	$2.90 \times 10^6$	$9.70 \times 10^5$	kg
	Snowfall	$M_{ppt}$	0	$5.60 \times 10^4$	kg
	Deposition	$M_{dep}$	$6.30 \times 10^3$	$4.10 \times 10^3$	kg
Output	Meltwater	$M_{water}$	$2.40 \times 10^5$	$2.30 \times 10^5$	kg
	Ice	$M_{ice}$	$2.20 \times 10^5$	$2.90 \times 10^2$	kg
	Sublimation	$M_{sub}$	$4.80 \times 10^4$	$5.20 \times 10^3$	kg
	Fountain wastewater	$M_{waste}$	$2.50 \times 10^6$	$8.00 \times 10^5$	kg
AIR	Freezing rate	$\Delta M_{freeze}/\Delta t$	$11 \pm 7$	$1 \pm 2$	l/min
	Melting rate	$\Delta M_{melt}/\Delta t$	$2 \pm 4$	$1 \pm 2$	l/min
	Thickness change	$j_{cone}$	$3 \pm 25$	$-4 \pm 27$	mm w. e.
	Net Water Loss		81	77	%
	Maximum Ice Volume		685	155	$m^3$
	Surface Area	$A_{cone}$	$350 \pm 38$	$127 \pm 34$	$m^2$
Model	Surface layer thickness	$\Delta x$	65	45	mm
	RMSE with ice volume		41	10	$m^3$
	Correlation with ice volume		0.98	0.96	N.A.

much more complex and requires a closer look at the correlation of the fountain parameters amongst themselves and with the weather parameters. This will be investigated in a follow-up study, with this study focusing on the weather aspects of the model.

### 5.1.2 Shape Assumption

The RMSE between the drone and the model estimates of the surface area for the IN21, CH21 and CH20 AIRs were 69 %, 25 and 65 % of the maximum area of the respective AIRs (see **Table 2**). There are two crude assumptions that lead to such a large error namely, assuming a conical shape and assuming a constant spray radius.

Both these assumptions are a consequence of favoring model simplicity over accuracy. One could, for example, model the AIR shape assuming its cross section is a gaussian curve instead of a triangle. But such methodologies will involve the inclusion of even more model parameters.

## 5.2 Model Calibration, Validation and Uncertainty

The calibration process used has an inherent temporal and spatial bias due to the choice of when and how many drone surveys were possible in each location. Among the five surveys of IN21 AIR used for calibration, most of them were conducted around early March when the AIR volume was near its maximum whereas the seven surveys of the CH21 location were more evenly spaced out in comparison (see **Table 2**). Moreover, the fountain spray radius is also biased as a consequence leading to further model error. Overestimation of CH20 AIR's spray radius could be one of the reasons we observe an overestimation of its volume since the spray radius is derived from just one drone survey closer to the end of the accumulation period.

The calibration methodology assumed no correlation between the sensitive model hyperparameter  $\Delta x$  and the other eight parameters. Since for all AIRs, the total order sensitivity of  $\Delta x$

and the rest of the parameters was greater and lesser than 0.6 and 0.1, respectively, this was a reasonable assumption to make.

Theoretically, the parameter selection for  $\Delta x$  is based on the following two arguments: (a) the ice thickness  $\Delta x$  should be small enough to represent the surface temperature variations at every model time step  $\Delta t$  and (b)  $\Delta x$  should be large enough for these temperature variations to not reach the bottom of the surface layer. The minimum modelled ice and bulk temperatures decrease and increase with increasing  $\Delta x$ . Thus, we can reframe conditions (a) and (b) in terms of the relationship between  $T_{ice}$ ,  $T_{bulk}$  and  $\Delta x$ . For example, all three AIRs studied had similar minimum modelled surface and bulk temperature around  $-24^\circ C$  and  $-3^\circ C$  respectively. Compared to  $T_{bulk}$ , the value of  $T_{ice}$  is not too high in accordance with (a) and not too low in accordance with (b). The magnitude of the difference expected between  $T_{ice}$  and  $T_{bulk}$  can be fixed with additional spatial and temporal ice temperature measurements of the AIR. This would lead to a better calibrated  $\Delta x$ . Therefore, uncertainty of the model could have been significantly reduced if such a temperature dataset had been available.

Practically, the surface layer thickness was also the only parameter compensating for the model's shape assumption. Since two AIRs merged to create the IN21 AIR, it had a drastically different shape evolution compared to the CH21 AIR. This also resulted in the different calibrated values of  $\Delta x$  in the Indian and the Swiss locations.

Uncertainty caused due to the other model parameters could also have been significantly reduced with further measurements. In particular, the fountain forcing parameters could have been avoided with a complete discharge rate dataset. Four out of the six uncertain weather parameters namely,  $\alpha_{ice}$ ,  $\alpha_{snow}$ ,  $\tau$  and  $T_{ppt}$  could have been better constrained through periodic measurements with an albedometer and a snow height sensor.

The model results highlight the high water losses in all the chosen locations. This could have been verified independently if all AIR meltwater and wastewater had been stored in a tank. But there were

two location-specific conditions that prevented us from doing so. First, the terrain of the site needs to be waterproof and oriented so that most of the AIR runoff can be collected. Second, the chosen location should not have high wind speeds, otherwise a significant fraction of AIR wastewater would be dispersed in the air. Both these conditions were not met for our chosen locations, hence efforts to measure the AIR runoff were abandoned. However, in an ideal location, this dataset could serve as a superior way to validate the model compared to the drone surveys which are also used for determining the spray radius.

### 5.3 Water Losses of AIRs

The net water losses of IN21 and CH21 AIR were 81 and 77 % of the total mass input, respectively. The high water losses were caused by the fountain wastewater for both AIRs. Therefore, AIRs lose water mostly during the accumulation period. The freezing rate of the IN21 AIR was less than  $20 \text{ l min}^{-1}$  for more than 90 % of the accumulation period, meaning that the growth was not limited by the water supply rate but rather by the freezing rate. The CH21 AIR freezing rate was able to reach the mean fountain discharge rate provided, albeit for only 2 h out of the 2155 h of fountain runtime available.

### 5.4 Fountain Optimization

Water losses could have been reduced in two ways: (a) reducing the fountain runtime  $t_F$  and (b) decreasing the mean fountain discharge rate  $d_F$ . For the CH21 AIR, strategy (a) could have saved considerable wastewater as no freezing was possible for 37 % of the accumulation period. For the IN21 site, strategy (b) would have yielded the least water loss as the freezing rate was more than half the mean discharge rate for just 2 hours. However, strategy (b) will also lead to a reduction in  $r_F$  if it is not accompanied by a suitable change in the fountain height and aperture diameter. So it can only be applied using the model if the corresponding fountain parameters are better parameterised.

Practically, both strategies are difficult to apply. It is unrealistic to expect someone constantly switching the fountain on and off under subzero conditions in accordance with strategy (a). Yes, strategy (b) is comparatively easier, but the minimum discharge rate is further constrained by the critical discharge rate below which the pipeline will freeze. However, both strategies can simultaneously be applied if the construction process is completely automated via a system that regulates the discharge in accordance with the model freezing estimates. Such a system can also drain the complete pipeline to prevent any pipeline freezing events. Since none of these functions are energy intensive, this system can be deployed anywhere using a solar powered energy source.

### 5.5 Favourable AIR Locations

Weather conditions play a significant role in making the Indian AIR larger and survive longer than the Swiss AIR, namely cloudiness, temperature and relative humidity. The lower cloudiness and mean winter temperature of the Indian location significantly reduced the net radiation flux during the accumulation period, enabling a faster AIR thickness growth. The lower winter temperature and humidity favour the sublimation over the deposition process, thus decreasing the magnitude of net turbulent fluxes during the ablation period. This results in a slower thickness decay. For AIRs with similar

fountain parameters, we expect locations with lower cloudiness, lower mean winter temperature to augment freezing rates and locations with lower humidity to dampen melting rates. Hence, AIRs should be considered in the water resource management strategy particularly of dry and cold mountain regions such as in Central Asia or the Andes where few other sustainable and affordable alternatives exist.

### 5.6 Model Application in New Locations

Since the model has been validated in two drastically different weather conditions and uses a methodology similar to the ones used on glaciers worldwide, we believe its performance should be similar in any other location.

The meteorological data and some fountain parameters are necessary to obtain modelled ice volume estimates. The necessary fountain parameters are  $r_F$  and  $t_F$ . The fountain runtime can be defined either with a fountain on and off date parameter or with a CSV file. Additionally, if  $d_F$  is known, the associated water losses can also be determined. As discussed before, the model is very sensitive to  $r_F$ , therefore it is recommended to manually measure the spray radius with the chosen fountain and pipeline.

All weather parameters can be assumed to have the median values of their ranges defined in **Table 3**. The model hyperparameter  $\Delta x$  needs to be calibrated beforehand. For a new location, we can use the surface layer thickness of CH21 AIR (45 mm) since it is representative of the shape evolution of a conical AIR.

The model is written in Python and completely based on open-source libraries. The model, source code, case studies and code examples for data preprocessing are provided on a freely accessible Git repository ([https://github.com/Gayashiva/air\\_model](https://github.com/Gayashiva/air_model), last access: December 17, 2021) for non-profit purposes. As a vision for the future, it is conceivable to extend the model for automatic AIR construction and foster a space where scientific and mountain communities can develop and apply various water resource management strategies together.

## 6 CONCLUSION

In this paper, we have developed a bulk energy and mass balance model to simulate AIR evolution using data from field measurements in Ganges, India and Guttannen, Switzerland. The use of these datasets, in combination with the novel model, allowed for an accurate representation of the complex evolution that is typical of an AIR. The model was calibrated and validated with ice volume and surface area observations obtained via drone surveys. We calculated the freezing and melting rates for each of the three AIRs and explained their corresponding magnitudes in terms of the influence of the chosen location and the fountain used. Our main conclusions are summarized below:

- The model was successful in reproducing the observed ice volume evolution with a correlation greater than 0.96 and an RMSE less than 18 % of the maximum ice volume for all AIRs.
- The ice volume achieved after the accumulation period was much higher for the Indian AIR compared to the Swiss AIRs. The lower net radiation fluxes of the Indian location favored a

faster thickness growth and the spray radius of the Indian fountain produced a higher surface area compared to the Swiss counterparts. Thus, the more than three times higher mean surface area and four times higher mean thickness growth during the two times shorter accumulation period of the Indian location resulted in a four times higher maximum ice volume of the Indian AIR compared to the Swiss.

- The ablation period of the Indian AIR was longer than the Swiss AIRs. However, the lower turbulent fluxes resulted in a slower thickness decay on a larger surface area. This rendered the differences between the IN21 and CH21 melting rates negligible. Since the accumulation period produced much higher ice volumes, the Indian AIR was able to last much longer than the Swiss AIRs.
- Water losses were high (> 77 %) mostly due to fountain wastewater for all AIRs. Vapour losses were insignificant (< 2 %) in comparison. However, a significant reduction in water loss is possible through optimization of fountain discharge rate.
- The Indian construction site produced long-lasting AIRs with higher maximum ice volumes since it was colder, drier and less cloudy compared to the Swiss construction site. Thus, the AIR technology is ideally suited to serve as a water management strategy, especially in dry and cold mountain regions such as in Central Asia or the Andes impacted by climate change induced water stress.

## DATA AVAILABILITY STATEMENT

Model code is freely available on GitHub ([https://github.com/Gayashiva/air\\_model](https://github.com/Gayashiva/air_model), last access: 17 December 2021) for non-profit purposes. The drone data can be obtained from the authors upon request.

## AUTHOR CONTRIBUTIONS

SB, MH, SW, and FK designed the study. SB developed the methodology with inputs from MH. MH, ML, and JO reviewed the algorithm and helped improve it. SB processed the drone data.

## REFERENCES

- Apel, H., Abdykerimova, Z., Agalhanova, M., Baimaganbetov, A., Gavrilenko, N., Gerlitz, L., et al. (2018). Statistical Forecast of Seasonal Discharge in central Asia Using Observational Records: Development of a Generic Linear Modelling Tool for Operational Water Resource Management. *Hydrol. Earth Syst. Sci.* 22, 2225–2254. doi:10.5194/hess-22-2225-2018
- Azam, M. F., Wagnon, P., Berthier, E., Vincent, C., Fujita, K., and Kargel, J. S. (2018). Review of the Status and Mass Changes of Himalayan-Karakoram Glaciers. *J. Glaciol.* 64, 61–74. doi:10.1017/jog.2017.86
- Bonales, L. J., Rodriguez, A. C., and Sanz, P. D. (2017). Thermal Conductivity of Ice Prepared under Different Conditions. *Int. J. Food Properties* 20, 610–619. doi:10.1080/10942912.2017.1306551
- Brock, B. W., Willis, I. C., and Sharp, M. J. (2006). Measurement and Parameterization of Aerodynamic Roughness Length Variations at Haut Glacier d’Arolla, Switzerland. *J. Glaciol.* 52, 281–297. doi:10.3189/172756506781828746
- SB wrote the model code. JB helped with model validation and uncertainty assessment. SB, MH, FK, and SW participated in the fieldwork. SB led the writing of the paper and all co-authors contributed to it.

## FUNDING

This work was supported and funded by the University of Fribourg and by the Swiss Government Excellence Scholarship (SB). The associated fieldwork in India was supported by the Himalayan Institute of Alternatives and funded by the Swiss Polar Institute.

## ACKNOWLEDGMENTS

This work would not have been possible without the untiring efforts of the Swiss and Indian iceshelf construction teams through the winters of 2019, 2020, and 2021. We thank Mr. Adolf Kaeser and Mr. Flavio Catillaz from Eispalast Schwarze (CH19); Daniel Bürki from the Guttannen Bewegt Association (CH20 and CH21); Norboo Thinles, Nishant Tiku, Sourabh Maheshwari and the rest of the HIAL team (IN21). We would also like to thank Hansueli Gubler for designing the Swiss AWS; Dr. Tom Matthews for designing the Indian AWS; Michelle Stirnimann for conducting the CH20 drone surveys and Digmesa AG for subsidising their flowmeter used in the experiment. We would particularly like to thank Prof. Thomas Schuler and 4 reviewers who gave us important inputs to improve the paper. We also thank Prof. Christian Hauck, Prof. Nanna B. Karlsson Dr. Andrew Tedstone and Alizé Carrère for valuable suggestions that improved the manuscript.

## SUPPLEMENTARY MATERIAL

The Supplementary Material for this article can be found online at: <https://www.frontiersin.org/articles/10.3389/feart.2021.771342/full#supplementary-material>

- Brutsaert, W. (1982). *Evaporation into the Atmosphere. Theory, History and Application.* Kluwer Academic Publishers.
- Brutsaert, W. (1975). On a Derivable Formula for Long-Wave Radiation from clear Skies. *Water Resour. Res.* 11, 742–744. doi:10.1029/WR011i005p00742
- Buytaert, W., Moulds, S., Acosta, L., De Bièvre, B., Olmos, C., Villacis, M., et al. (2017). Glacial Melt Content of Water Use in the Tropical Andes. *Environ. Res. Lett.* 12, 114014. doi:10.1088/1748-9326/aa926c
- Chen, Y., Li, W., Deng, H., Fang, G., and Li, Z. (2016). Changes in central Asia’s Water tower: Past, Present and Future. *Nature* 6, 35458. doi:10.1088/1748-9326/aa926c
- [Dataset] Copernicus Climate Change Service (C3S) (2017). Era5: Fifth Generation of Ecmwf Atmospheric Reanalyses of the Global Climate. Available at <https://cds.climate.copernicus.eu/cdsapp#!/home> (Accessed 10/01/2019).
- Cuffey, K. M., and Paterson, W. S. B. (2010). *The Physics of Glaciers.* Elsevier.
- Furukawa, Y., and Ponce, J. (2010). Accurate, Dense, and Robust Multiview Stereopsis. *IEEE Trans. Pattern Anal. Mach. Intell.* 32, 1362–1376. doi:10.1109/TPAMI.2009.161

- Garratt, J. R. (1992). *The Atmospheric Boundary Layer*. Cambridge University Press.
- Grossman, D. (2015). As Himalayan Glaciers Melt, Two Towns Face the Fallout. Available at [https://e360.yale.edu/features/as\\_himalayan\\_glaciers\\_melt\\_two\\_towns\\_face\\_the fallout](https://e360.yale.edu/features/as_himalayan_glaciers_melt_two_towns_face_the fallout) (Accessed 10 01, 2019).
- Hock, R., Rasul, G., Adler, C., Cáceres, B., Gruber, S., Hirabayashi, Y., et al. (2019). "2019: High Mountain Areas," in *IPCC Special Report on the Ocean and Cryosphere in a Changing Climate*. Editors H.-O. Pörtner, D. C. Roberts, V. Masson-Delmotte, P. Zhai, M. Tignor, E. Poloczanska, et al. (Cambridge, United Kingdom: Cambridge University Press).
- Hoelzle, M., Barandun, M., Bolch, T., Fiddes, J., Gafurov, A., Muccione, V., et al. (2019). The Status and Role of the alpine Cryosphere in Central Asia, 100, 121. doi:10.4324/9780429436475-8
- Hori, M., Aoki, T., Tanikawa, T., Motoyoshi, H., Hachikubo, A., Sugiura, K., et al. (2006). In-situ Measured Spectral Directional Emissivity of Snow and Ice in the 8–14 μm Atmospheric Window. *Remote Sensing Environ.* 100, 486–502. doi:10.1016/j.rse.2005.11.001
- Huang, J. (2018). A Simple Accurate Formula for Calculating Saturation Vapor Pressure of Water and Ice. *AMETSO* 57, 1265–1272. doi:10.1175/JAMC-D-17-0334.1
- Immerzeel, W. W., Lutz, A. F., Andrade, M., Bahl, A., Biemans, H., Bolch, T., et al. (2019). Importance and Vulnerability of the World's Water Towers. *Nature* 577, 364–369. doi:10.1038/s41586-019-1822-y
- Küng, O., Strecha, C., Beyeler, A., Zufferey, J.-C., Floreano, D., Fua, P., et al. (2011). The Accuracy of Automatic Photogrammetric Techniques on Ultra-light Uav Imagery. *Int. Arch. Photogramm. Remote Sens. Spat. Inf. Sci.* XXXVIII-1/C22, 125–130. doi:10.5194/isprsarchives-XXXVIII-1-C22-125-2011
- Labbal, V. (2000). *Traditional Oases of Ladakh: A Case Study of Equity in Water Management*. Oxford, UK: Oxford University Press, 163–183.
- Lowe, D. G. (2004). Distinctive Image Features from Scale-Invariant Keypoints. *Int. J. Comp. Vis.* 60, 91–110. doi:10.1023/B:VISI.0000029664.99615.94
- Meteoblue (2021). Climate Guttannen. Available at [https://www.meteoblue.com/en/weather/historyclimate/climatemodeled/guttannen\\_switzerland\\_2660433](https://www.meteoblue.com/en/weather/historyclimate/climatemodeled/guttannen_switzerland_2660433) (Accessed 07 19, 2021).
- Mölg, N., and Bolch, T. (2017). Structure-from-motion Using Historical Aerial Images to Analyse Changes in Glacier Surface Elevation. *Remote Sensing* 9, 1021. doi:10.3390/rs9101021
- Mölg, T., and Hardy, D. R. (2004). Ablation and Associated Energy Balance of a Horizontal Glacier Surface on Kilimanjaro. *J. Geophys. Res.* 109, 1–13. doi:10.1029/2003JD004338
- Nüsser, M., Dame, J., Kraus, B., Baghel, R., and Schmidt, S. (2019a). Socio-hydrology of "artificial Glaciers" in Ladakh, India: Assessing Adaptive Strategies in a Changing Cryosphere. *Reg. Environ. Change* 19, 1327–1337. doi:10.1007/s10113-018-1372-0
- Nüsser, M., Dame, J., Parveen, S., Kraus, B., Baghel, R., and Schmidt, S. (2019b). Cryosphere-Fed Irrigation Networks in the Northwestern Himalaya: Precarious Livelihoods and Adaptation Strategies under the Impact of Climate Change. *Mountain Res. Dev.* 39. doi:10.1659/MRD-JOURNAL-D-18-00072.1
- Nüsser, M., Schmidt, S., and Dame, J. (2012). Irrigation and Development in the Upper Indus Basin: Characteristics and Recent Changes of a Socio-Hydrological System in Central Ladakh, India. *Mountain Res. Dev.* 32, 51–61. doi:10.1659/MRD-JOURNAL-D-11-00091.1
- Oerlemans, J., Balasubramanian, S., Clavuot, C., and Keller, F. (2021). Brief Communication: Growth and Decay of an Ice Stupa in alpine Conditions - a Simple Model Driven by Energy-Flux Observations over a Glacier Surface. *The Cryosphere* 15, 3007–3012. doi:10.5194/tc-15-3007-2021
- Oerlemans, J., and Knap, W. H. (1998). A 1 Year Record of Global Radiation and Albedo in the Ablation Zone of Morteratschgletscher, switzerland. *J. Glaciol.* 44, 231–238. doi:10.3189/S00221430000257410.1017/S0022143000002574
- Sa, P. (2020). Pix4dMapper 4.1 User Manual. Available at <https://support.pix4d.com/hc/en-us/articles/204272989-Offline-Getting-Started-and-Manual-pdf> (Accessed 12 09, 2021).
- Scherrer, S. C. (2020). Temperature Monitoring in Mountain Regions Using Reanalyses: Lessons from the Alps. *Environ. Res. Lett.* 15, 044005. doi:10.1088/1748-9326/ab702d
- Schmidt, L. S., Aðalgeirs Óttir, G., Guðmundsson, S., Langen, P. L., Pálsson, F., Mottram, R., et al. (2017). The Importance of Accurate Glacier Albedo for Estimates of Surface Mass Balance on Vatnajökull: Evaluating the Surface Energy Budget in a Regional Climate Model with Automatic Weather Station Observations. *The Cryosphere* 11, 1665–1684. doi:10.5194/tc-11-1665-2017
- Schmidt, S., and Nüsser, M. (2012). Changes of High Altitude Glaciers from 1969 to 2010 in the Trans-himalayan Kang Yatze Massif, Ladakh, Northwest india. *Arctic, Antarctic, Alpine Res.* 44, 107–121. doi:10.1657/1938-4246-44.1.107
- Steiner, J. F., Pellicciotti, F., Buri, P., Miles, E. S., Immerzeel, W. W., and Reid, T. D. (2015). Modelling Ice-Cliff Backwasting on a Debris-Covered Glacier in the Nepalese Himalaya. *J. Glaciol.* 61, 889–907. doi:10.3189/2015JoG14J194
- Tennøe, S., Halnes, G., and Einevoll, G. T. (2018). UncertaintyPy: A python Toolbox for Uncertainty Quantification and Sensitivity Analysis in Computational Neuroscience. *Front. Neuroinform.* 12, 49. doi:10.3389/fninf.2018.00049
- Thayyen, R. J., and Gergan, J. T. (2010). Role of Glaciers in Watershed Hydrology: a Preliminary Study of a "Himalayan Catchment". *The Cryosphere* 4, 115–128. doi:10.5194/tc-4-115-2010
- Turner, D., Lucieer, A., and Watson, C. (2012). An Automated Technique for Generating Georectified Mosaics from Ultra-high Resolution Unmanned Aerial Vehicle (Uav) Imagery, Based on Structure from Motion (Sfm) point Clouds. *Remote Sensing* 4, 1392–1410. doi:10.3390/rs4051392
- Unger-Shayesteh, K., Vorogushyn, S., Farinotti, D., Gafurov, A., Duethmann, D., Mandychev, A., et al. (2013). What Do We Know about Past Changes in the Water Cycle of central Asian Headwaters? a Review. *Glob. Planet. Change* 110, 4–25. doi:10.1016/j.gloplacha.2013.02.004
- Wangchuk, S. (2015b). Ice Stupa Artificial Glacier Inaugurated. Available at <http://icestupa.org/news/ice-stupa-artificial-glacier-inaugurated-5th-of-march> (Accessed 10 01, 2019).
- Wangchuk, S. (2014). Ice Stupa Artificial Glaciers of Ladakh. Available at [www.indiegogo.com/projects/ice-stupa-artificial-glaciers-of-ladakh#](http://www.indiegogo.com/projects/ice-stupa-artificial-glaciers-of-ladakh#/) (Accessed 10 01, 2019).
- Wangchuk, S. (2021). Ice Stupa Competition. Available at <https://tribal.nic.in/IceStupa.aspx> (Accessed 12 13, 2021).
- Wangchuk, S. (2015c). Ice Stupa Surpasses Guinness World Record. Available at <http://icestupa.org/news/ice-stupa-surpasses-guinness-world-record> (Accessed 10 01, 2019).
- Wangchuk, S. (2015d). Ice Stupa Way of Celebrating a Special Day. Available at <http://icestupa.org/news/ice-stupa-way-of-celebrating-a-special-day6th-of-june> (Accessed 10 01, 2019).
- Wangchuk, S. (2015a). The Good News at Ice Stupa. Available at <http://icestupa.org/news/the-good-news-at-ice-stupa> (Accessed 10 01, 2019).
- Wangchuk, S. (2015e). World Water Day at Ice Stupa. Available at <http://icestupa.org/news/world-water-day-at-ice-stupa> (Accessed 10 01, 2019).
- Woolf, H. M. (1968). *On the Computation of Solar Elevation Angles and the Determination of Sunrise and sunset Times*. Washington, DC: National Aeronautics and Space Administration. Available at <https://ntrs.nasa.gov/citations/19680025707> (Accessed April 01, 2022).
- Xiu, D., and Hesthaven, J. S. (2005). High-order Collocation Methods for Differential Equations with Random Inputs. *SIAM J. Sci. Comput.* 27, 1118–1139. doi:10.1137/040615201
- Zhou, S., Kang, S., Gao, T., and Zhang, G. (2010). Response of Zhadang Glacier Runoff in Nam Co basin, Tibet, to Changes in Air Temperature and Precipitation Form. *Chin. Sci. Bull.* 55, 2103–2110. doi:10.1007/s11434-010-3290-5
- Zolles, T., Maussion, F., Galos, S. P., Gurgiser, W., and Nicholson, L. (2019). Robust Uncertainty Assessment of the Spatio-Temporal Transferability of Glacier Mass and Energy Balance Models. *The Cryosphere* 13, 469–489. doi:10.5194/tc-13-469-2019
- Conflict of Interest:** The authors declare that the research was conducted in the absence of any commercial or financial relationships that could be construed as a potential conflict of interest.
- Publisher's Note:** All claims expressed in this article are solely those of the authors and do not necessarily represent those of their affiliated organizations, or those of the publisher, the editors and the reviewers. Any product that may be evaluated in this article, or claim that may be made by its manufacturer, is not guaranteed or endorsed by the publisher.
- Copyright © 2022 Balasubramanian, Hoelzle, Lehning, Bolíbar, Wangchuk, Oerlemans and Keller. This is an open-access article distributed under the terms of the Creative Commons Attribution License (CC BY). The use, distribution or reproduction in other forums is permitted, provided the original author(s) and the copyright owner(s) are credited and that the original publication in this journal is cited, in accordance with accepted academic practice. No use, distribution or reproduction is permitted which does not comply with these terms.

## Paper III

# **Improving water-use efficiency of artificial ice reservoirs (Icestupas) through weather-sensitive fountain scheduling strategies**

Balasubramanian, S., Hoelzle, M., and Waser, R.

Frontiers in Earth Science 9 (February 23, 2022): 771342. doi:10.3389/feart.2021.771342.

# Improving water-use efficiency of artificial ice reservoirs (IceStupas) through weather-sensitive fountain scheduling strategies

Suryanarayanan Balasubramanian<sup>1,2</sup>, Martin Hoelzle<sup>1</sup>, and Roger Waser<sup>3</sup>

<sup>1</sup>University of Fribourg, Department of Geosciences, Fribourg, Switzerland

<sup>2</sup>Himalayan Institute of Alternatives, Ladakh, India

<sup>3</sup>University of Applied Sciences and Arts, Luzern, Switzerland

**Correspondence:** suryanarayanan.balasubramanian@unifr.ch

## Abstract.

Artificial Ice Reservoirs (AIRs), often also called - Ice Stupas - are a climate change adaptation strategy developed in the Indian Himalayas (Ladakh). With this technology, otherwise unused stream water is stored in large ice towers in winter. The surplus melt water that is generated in spring is used for satisfying irrigation water demands. Recent studies have shown that during construction of traditional AIRs over 75 % of the water sprayed was lost. Therefore, fountain wastewater production has to be reduced for improving water use efficiency. During the winter of 2021-22, a traditional and an automated AIR were built in Guttannen, Canton of Berne, Switzerland with the main aim of comparing and quantifying the benefits of fountain scheduling. Fountain scheduling was realized through an automation system computing recommended discharge rates using real-time weather input and location metadata. The scheduled fountain produced similar volumes while consuming 87 % less water than the unscheduled fountain. Simulations converting unscheduled fountains to scheduled fountains improved the water use efficiency of several traditional AIRs more than two fold. Overall, these results show that the automated construction strategy can increase the water use efficiency of AIRs without compromising their meltwater production.

## 1 Introduction

Cryosphere-fed irrigation networks in arid mountain regions are completely dependent on timely availability of meltwater from glaciers, snow and permafrost (Immerzeel et al., 2020; Farhan et al., 2015; Tveiten, 2007). With the accelerated decline of glaciers due to climate change (Nüsser and Baghel, 2016), these regions are experiencing water scarcity particularly during the spring season (Norphel and Tashi, 2015). This seasonal water scarcity makes it essential to provide supplementary irrigation in order to sustain agricultural output and take advantage of the complete growing season (Nüsser and Baghel, 2016; Vincent, 2009).

To cope with this recurrent water scarcity, villagers in the region of Ladakh have developed two types of artificial ice reservoirs (AIRs): ice terraces and ice stupas (see Fig. 1). All these types of ice reservoirs capture water in the autumn and winter, allowing it to freeze, and hold it until spring, when it melts and flows down to fields (IPCC, 2019; Vince, 2009; Clouse et al., 2017; Nüsser et al., 2019). In this way, they retain a previously unused portion of the annual flow and facilitate its use to supplement the decreased flow in the following spring. This study focuses on the form of AIRs locally called as ice stupas.

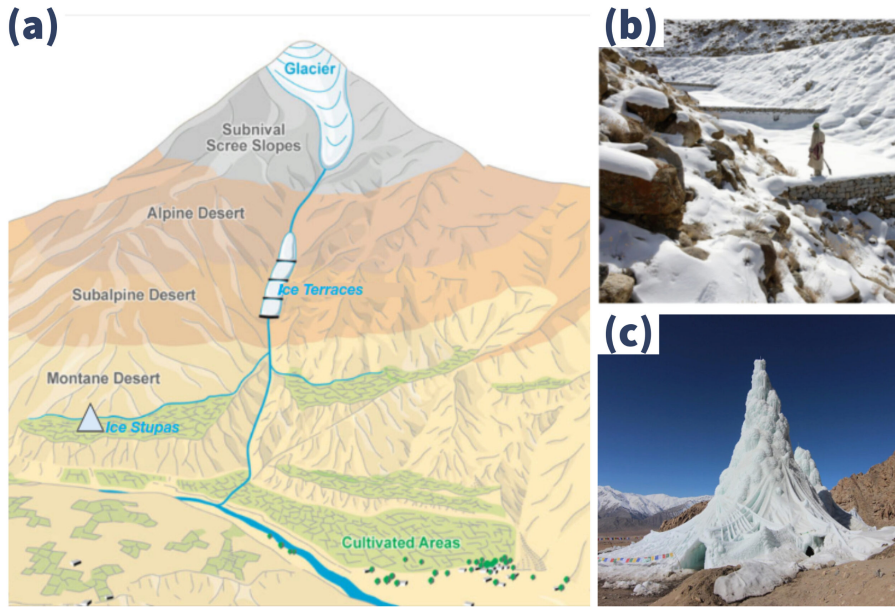


**Figure 1.** (a) Schematic overview of the position of artificial ice reservoirs. These constructions are located at altitudes between the glaciers and the irrigation networks in the cultivated areas. Ice terraces and ice stupas are located at higher and lower altitudes respectively. Adapted from: Nüsser and Baghel (2016)

Over the past decade, several ice stupas have been built to supplement irrigation water supply of mountain villages in India (Wangchuk, 2020; Palmer, 2022; Aggarwal et al., 2021), Kyrgyzstan (BBC News, 2020) and Chile (Reuters, 2021). These AIRs are traditionally constructed by diverting springs or glacial streams into fountain spray systems via embankments and pipelines.

One of the most common problems with AIR construction systems has to do with fountain scheduling. Fountain scheduling is simply answering the questions of “When do we spray?” and “How long do we spray?”. Starting fountain spray too early and/or running a fountain spray too long is considered overwatering. At the very least this practice wastes water. However, overwatering can cause accelerated ice melt if done on a prolonged basis. Likewise, starting fountain spray too late or not running the system for a long enough period of time is considered under watering and can cause reduced ice volumes.

Previous work (Balasubramanian et al., 2022) has shown that traditional construction systems tend to suffer from overwatering. Knowledge of surface freezing rates is important to avoid overwatering. Surface freezing rates can be calculated by means of the full energy balance model developed in Balasubramanian et al. (2022). This model can be forced with either historical weather data or real-time weather data to produce recommended discharge rates.

However, there are several issues that need to be addressed before operating such weather-sensitive fountains. For example, in the case of the Indian AIR, the fountain discharge rate could have been halved since they were always two times higher than the modelled freezing rate (Balasubramanian et al., 2022). However, in practice, reduction of discharge rate would compromise

the maximum ice volume obtained due to reduction in the fountain spray radius and could increase the maintenance cost due to higher risk of fountain freezing events.

An optimum construction strategy, therefore, should first prevent the occurrence of these two events before reducing discharge rates. Spray radius can be maintained if the fountain aperture diameter is lowered with the discharge rate. Fountain  
45 freezing events can be prevented if the discharge is not lowered below a minimum threshold.

Recommended discharge rate needs to be sensitive to constraints on the water supply or weather of the construction site. Locations limited by their water supply like in Ladakh, India would prioritize water use efficiency whereas those limited by the favourable weather windows like in Guttannen, Switzerland would prioritize for maximum ice volume. Accordingly, we  
50 use two types of model parameter optimizations that prevent underwatering and overwatering to attain higher ice volumes and higher water use efficiency respectively.

However, manually adjusting the fountain discharge rate is not practical due to two reasons. Firstly, this would involve constant adjustments of discharge rates in response to the significant diurnal and seasonal variations of the freezing rates. Secondly, frequent pipeline water drainage is required to avoid water losses. Therefore, operation of weather-sensitive fountains via automation systems is preferred to reduce the maintenance long-term costs.

55 The present study was performed to compare two AIRs produced using different fountain scheduling strategies but exposed to identical meteorological conditions. The specific objectives of this study is to include the water-use efficiency and maximum ice volume comparison of different fountain scheduling strategies, presentation of the automation system, and examples of its application to the computation of fountain scheduling strategies.

## 2 Study sites and data

60 In this study, we use some datasets presented in our previous work (Balasubramanian et al., 2022) along with new datasets. These old datasets record the meteorological conditions and fountain characteristics of AIRs built in Gangles, India (IN21) and Guttannen, Switzerland (CH21) during the winter of 2020-21. In this section, we focus on describing the AIR datasets collected in Guttannen, Switzerland during the winter of 2021-22 (CH22).

The Guttannen site ( $46.66^{\circ}\text{N}$ ,  $8.29^{\circ}\text{E}$ ) is situated in the Berne region, Switzerland and has an altitude of  $1047\text{ m a.s.l}$ .  
65 In the winter (Oct-Apr), mean daily minimum and maximum air temperatures vary between  $-13$  and  $15^{\circ}\text{C}$ . Clear skies are rare, averaging around 7 days during winter. Daily winter precipitation can sometimes be as high as  $100\text{ mm}$ . These values are based on 30 years of hourly historical weather data measurements (Meteoblue, 2021). Two AIRs were constructed by the Guttannen Bewegt Association, the University of Fribourg and the Lucerne University of Applied Sciences and Arts during the winters of 2021-22 using a traditional and an automated construction strategy.

70 The automated and the traditional AIRs were constructed adjacent to each other as shown in Fig. 2. This ensured both AIRs shared the same water source and identical weather conditions. In addition, a webcam guaranteed a continuous survey of the automated AIR.



**Figure 2.** Automated and traditional AIRs at Guttannen on February 6, 2022. Picture credits: Daniel Bürki

In the traditional strategy, the fountain was operated manually whereas in the automated strategy a programmed automation system controlled the fountain discharge rate during the whole study period using real time weather input and several control parameters, which could be modified via a user interface. Henceforth, we refer to the fountain used in the traditional and automated construction strategy as unscheduled and scheduled fountains respectively.

In the traditional construction strategy, tree branches were laid covering the fountain pipe to initiate and speed up the ice cone formation process. In the automated strategy, only the fountain pipe was placed before the water spray started. The construction of both the AIRs began on 8th December on a snow bed of 13 cm thickness and ended on 12th April. These two dates are denoted as start and expiry dates henceforth.

## 2.1 Meteorological data

Air temperature, relative humidity, wind speed, pressure, long-wave, short-wave direct and diffuse radiation are required to calculate the surface energy balance of an AIR. The weather data source was an automatic weather station (AWS) located around 20 m away as shown in Fig. 2. Less than 0.4 % of the data was found to be missing and the data gaps were filled by linear interpolation. Hourly ground temperature measurements were also recorded by the AWS to approximate the fountain's water temperature.

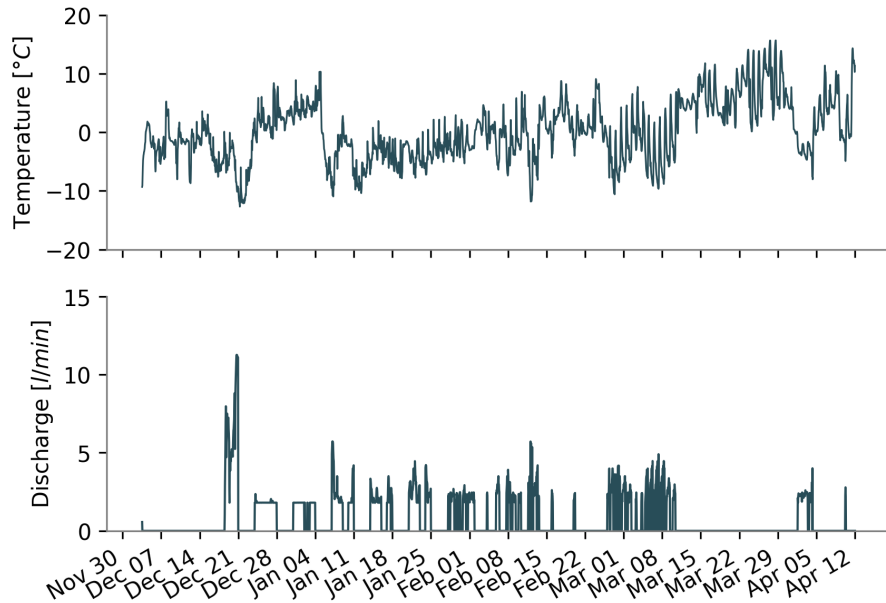


**Figure 3.** Temperature and discharge measurements at the Guttannen construction site

## 2.2 Fountain observations

The fountain consists of a pipeline and a nozzle. The pipeline has three attributes, namely : discharge rate ( $Q$ ), height ( $h$ ) and water temperature ( $T_F$ ). Discharge rate represents the discharge rate of the water in the fountain pipeline. Height denotes 90 the height of the fountain pipeline installed. Fountain water temperature is the temperature of water droplets produced by the fountain.

The fountain nozzle has three characteristics, namely : the aperture diameter ( $dia$ ), the spray radius ( $r$ ) and pressure loss ( $P$ ). The fountain nozzle is assumed to have only one aperture with diameter  $dia$  from where water is sprayed. Spray radius denotes the observed ice radius formed from the fountain water droplets. Pressure loss denotes the loss of water head caused 95 due to the fountain nozzle.

Fig. 3 shows how the automation system scheduled the discharge rate based on real-time meteorological conditions. The automation system caused these variations through its control valve which varied between 0 to 100 % depending on the recommended discharge rate. Throughout the study period, the control valve was opened completely (100 %) only once corresponding to the time when the temperature attained its minimum of -13 °C on 20th December. After this event, the control valve was 100 never opened beyond 34 %.

The unscheduled fountain was manually operated to spray all the available discharge until a fountain freezing event interrupted the discharge on 17th February. Unfortunately, no discharge rate measurements were recorded for the unscheduled

**Table 1.** Summary of the drone surveys

	No.	Date	Volume	Radius	Surface Area
Traditional	1	Dec 23, 2021	17 m <sup>3</sup>	2.9 m	47 m <sup>2</sup>
	2	Jan 3, 2022	22 m <sup>3</sup>	3.4 m	61 m <sup>2</sup>
	3	Jan 22, 2022	35 m <sup>3</sup>	4 m	79 m <sup>2</sup>
	4	Feb 6, 2022	44 m <sup>3</sup>	4.2 m	86 m <sup>2</sup>
	5	Feb 20, 2022	43 m <sup>3</sup>	4.3 m	86 m <sup>2</sup>
	6	Mar 19, 2022	33 m <sup>3</sup>	4.4 m	84 m <sup>2</sup>
	7	Mar 26, 2022	24 m <sup>3</sup>	4.3 m	74 m <sup>2</sup>
	8	Apr 12, 2022	11 m <sup>3</sup>	3.5 m	50 m <sup>2</sup>
Automated	1	Dec 23, 2021	35 m <sup>3</sup>	4.3 m	73 m <sup>2</sup>
	2	Jan 3, 2022	32 m <sup>3</sup>	4.4 m	81 m <sup>2</sup>
	3	Feb 20, 2022	60 m <sup>3</sup>	5.3 m	105 m <sup>2</sup>
	4	Mar 19, 2022	28 m <sup>3</sup>	3.7 m	57 m <sup>2</sup>
	5	Mar 26, 2022	19 m <sup>3</sup>	3.7 m	53 m <sup>2</sup>
	6	Apr 12, 2022	7 m <sup>3</sup>	2.5 m	53 m <sup>2</sup>

fountain. Therefore, this dataset was estimated from the discharge rate measurements and characteristics of the scheduled fountain.

105 The height was also increased in steps of 1 meter for both the fountains. This caused variations in the corresponding discharge rate. For the scheduled fountain, the construction began with a height of 3 m with an increase to 4 m on 23rd December. This fountain height increase reduced its maximum discharge from 13 l/min to 11 l/min. For the unscheduled fountain, the construction began with a height of 3.7 m and then this was increased two times on 23rd December and 12th February.

The water temperature of both the fountains were estimated from the AWS ground temperature dataset.

110 The spray radius was estimated for both the fountains from several drone flights. Ice radius measurements of drone flights which observed either an increase in AIR circumference or volume were averaged to determine the fountain's spray radius.

### 2.3 Drone surveys

Several photogrammetric surveys were conducted on the traditional and the automated AIRs. The details of these surveys and the methodology used to produce the corresponding outputs are explained in Balasubramanian et al. (2022). The digital elevation models (DEMs) generated from the obtained imagery were analysed to document the spray radius, the surface area and the volume of the ice structures. The number of drone surveys conducted for the traditional and the automated AIRs were 8 and 6, respectively (see Table 1).

**Table 2.** Assumptions for the parametrisation introduced to simplify the model.

Estimation of	Symbol	IVOM	WEOM
Slope	$s_{cone}$	1	0
Albedo	$\alpha$	$\alpha_{snow}$	$\alpha_{ice}$
Cloudiness	$cld$	0	1

### 3 Methods

#### 3.1 Determination of recommended discharge rate

120 Recommended discharge rate of the automation system depend upon whether the construction location is constrained by the available water supply or the duration of favourable weather windows for fountain operation. If the respective location has limited water supply then the fountain scheduling strategy should be optimised for water-use efficiency . But if the location is limited by the time period when the fountain can function then the scheduling strategy should be optimised for ice volumes.

Accordingly, we introduce two kinds of model forcing assumptions corresponding to the ice volume and water-use efficiency objective for the following three model variables: (a) slope , (b) albedo and (c) cloudiness. The slope variable increases the shortwave radiation and sensible heat impact. The albedo variable decreases the shortwave radiation impact. The cloudiness variable increases both the shortwave and the longwave radiation impact. Therefore, increase of slope and cloudiness variable increases melting energy and increase of albedo variable increases freezing energy. Assumptions used for the ice volume and water-use efficiency objectives overestimate and underestimate the freezing rate of the AIR respectively. Correspondingly, we 130 associate the upper and lower bounds of these variables as shown in Table 2. These two kinds of models will be referred to as ice volume optimised model (IVOM) and water-use efficiency optimised model (WEOM) respectively.

We apply the assumptions described in Table 2 on the one-dimensional description of energy fluxes as used in Balasubramanian et al. (2022) to obtain the rate of change of AIR ice mass as follows:

$$\frac{\Delta M_{ice}}{\Delta t} = \left( \frac{q_{SW} + q_{LW} + q_S + q_F + q_R + q_G - q_T}{L_F} + \frac{q_L}{L_V} \right) \cdot A_{cone} \quad (1)$$

135 Upward and downward fluxes relative to the ice surface are positive and negative, respectively. The first term represents the mass change rate due to freezing of the fountain water and melting of the ice.  $q_{SW}$  is the net short-wave radiation;  $q_{LW}$  is the net long-wave radiation;  $q_L$  and  $q_S$  are the turbulent latent and sensible heat fluxes;  $q_F$  is the fountain discharge heat flux;  $q_R$  is the rain water heat flux;  $q_G$  is the ground heat flux;  $q_T$  is the temperature heat flux and  $A_{cone}$  is the area of the AIR surface. The derivation of these individual terms for the IVOM and WEOM model versions are discussed in the Appendix C.

140 Equation 1 is implemented in the automation system through a user interface that enables input of the spray radius, altitude, latitude and longitude of the construction location. Once switched on, the automation system regulates the fountain discharge

rate based on the recommended discharge rate. Further details about how the automation system functions can be found in Appendix A.

### 3.2 Model updates

145 The model was made more sensitive to fountain discharge rate feedback for comparing the volume evolution of the automated and traditional AIRs. These updates are explained in detail in Appendix B.

### 3.3 Calibration and Validation

The model parameters were calibrated to the median values of the ranges presented in Appendix Table A1.

We performed the validation of the model on the traditional and automated AIRs by evaluating the root mean squared error 150 (RMSE) between volume estimates and measurements.

The performance of the IVOM and WEOM versions of the physical model was assessed by comparing correlation of its discharge rate estimates with the validated freezing rate of calibrated model.

### 3.4 Fountain characteristics

The aperture configuration of the scheduled and unscheduled fountains were far too complex to enable a direct comparison (see 155 Fig. ). To circumvent this, both the fountain designs were approximated to a simple fountain design with just one aperture (see Fig. ). Then the corresponding aperture diameter (*dia*) of this simple fountain was chosen so that it validates the observations recorded for the different fountains.

The fountain's height (*h*), aperture diameter (*dia*) and pressure loss (*P*) were related to its discharge rate (*Q*) through the Bernoulli equation :

$$160 \quad P_i + \rho_{water} \cdot g \cdot h_i + 1/2 \cdot \rho_{water} \cdot v_i^2 = P_f + \rho_{water} \cdot g \cdot h_f + 1/2 \cdot \rho_{water} \cdot v_f^2 \quad (2)$$

where  $\rho_{water}$  is the density of water and  $v$  is the velocity of the fountain water droplets. The subscripts *i* and *f* refer to the initial and final states of the system.  $v$  can be determined from the discharge rate *Q* through the mass conservation equation as

$$v = 4 \cdot Q / (\pi \cdot dia^2) \quad (3)$$

Combining the Eqns. 2 and 3, we get the final discharge  $Q_f$  after a height change from  $h_i$  to  $h_f$  to be:

$$165 \quad Q_f = \sqrt{Q_i^2 + 2 \cdot g \cdot (h_i - h_f) \cdot (\pi \cdot dia^2 / 4)^2} \quad (4)$$

Assuming that the water droplets have diameter equal to the fountain aperture diameter and follow projectile motion starting from a fountain height *h* with a launch angle  $\theta = 45^\circ$ , we get the following equation for the spray radius *r*:

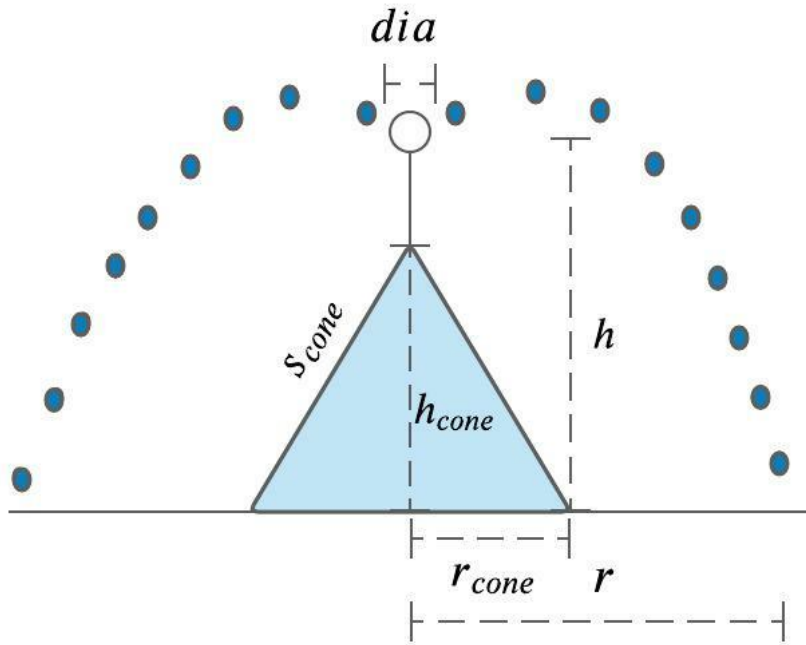


**Figure 4.** Shape variables and fountain characteristics of the AIR.  $r_{cone}$  is the radius,  $h_{cone}$  is the height and  $s_{cone}$  is the slope of the AIR ice cone.  $r$  is the spray radius,  $dia$  is the aperture diameter and  $h$  is the fountain height

$$r = \frac{v \cdot (v + \sqrt{v^2 + 4hg})}{2g} \quad (5)$$

## 4 Results

### 170 4.1 Estimation of fountain characteristics

The influence of the fountain height increase event on the maximum discharge rate was used to determine the fountain nozzle's aperture diameter. The maximum discharge rate of the scheduled fountain reduced from  $Q_i = 13 \text{ l/min}$  to  $Q_f = 11 \text{ l/min}$  when the fountain height was raised from  $h_i = 3 \text{ m}$  to  $h_f = 4 \text{ m}$ . Inputting the corresponding values in Eqn. 2, we get the estimated fountain aperture diameter ( $dia$ ) to be around  $5 \text{ mm}$ .

175 The change in discharge rate observed upon removal of the fountain nozzle was used to determine the fountain pressure loss. When the fountain nozzle was removed, the maximum discharge rate of the fountain was observed to increase from  $Q_i = 11 \text{ l/min}$  to  $Q_f = 27 \text{ l/min}$ . Using the fountain aperture diameter  $d_i = 5 \text{ mm}$ , the pipeline diameter  $d_f = 19 \text{ mm}$ ,  $P_f = 0$  and

$h_i = h_f$  in Eqn. 2 we estimate the pressure loss occurring due to the fountain nozzle to be equivalent to 4.3 meters of water head.

#### 180 4.2 Unscheduled discharge rate estimation

The pressure loss of unscheduled fountain was determined by assuming a linear relationship of pressure loss with aperture diameter. We use two observations to determine this linear relationship, namely, that the pressure loss of the fountain was zero with a diameter of 19 mm (fountain removal event) and that the scheduled fountain had a pressure loss of 4.3 m with an aperture diameter 5 mm. We estimate that for a constant height the pressure decreases by 18 mm for every 1 mm increase in aperture diameter (see Fig. 5 (a)).

The fountain freezing event observation was used to determine the unscheduled fountain nozzle's aperture diameter. The unscheduled fountain had a fountain freezing event at height 5.7 m. We assume that its discharge rate was close to zero during this event. The aperture diameter with the fountain freezing height closest to 5.7 m is 7 mm according to Eqn. 2 as shown in Fig. 5 (b). The corresponding pressure loss of a fountain with 7 mm diameter is 3.7 m as shown in Fig. 5 (a).

190 Fig. 5 (c) shows the unscheduled discharge rate estimated for the study period. The temporal variation in the discharge rate is caused due to the two height increase events on 23rd Dec and 12th February that increased the height from 3.7 to 5.7 m respectively.

#### 4.3 Scheduled discharge rate simulations

We found that the WEOM and IVOM model versions estimated the freezing rate of the unscheduled fountain with a correlation 195 around 0.6 and a RMSE less than 0.6 l/min and 1.6 l/min respectively. The IVOM scheduled fountain overestimated the freezing rate 44 % of the construction duration whereas the WEOM scheduled fountain underestimated the freezing rate 67 % of the construction duration. Therefore, the IVOM and WEOM model forcings were successful in prioritizing the maximum ice volume and water use efficiency metrics respectively.

#### 4.4 Model validation

200 The volume estimation for the automated and traditional AIR had an RMSE of 13 m<sup>3</sup> and 5 m<sup>3</sup> with the drone volume observations, respectively. This RMSE error is within 20 % and 11 % of the maximum volume of the automated and the traditional AIR respectively. The estimated and measured AIR volumes are shown in Fig. 6.

#### 4.5 Comparison of AIR construction strategies

Table 3 shows how the different fountain scheduling strategies influence the mass and energy balance of the respective AIR. The 205 difference between the fountain discharge input and fountain wastewater output of the unscheduled and scheduled fountains was around an order of magnitude.

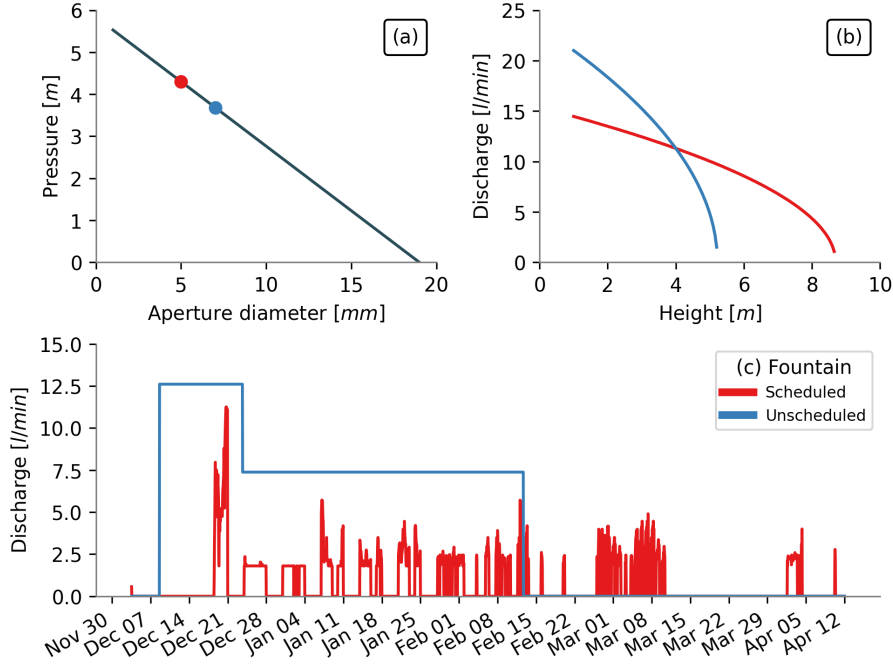


**Figure 5.** (a) Pressure loss as a linear function of aperture diameter for a constant fountain height and discharge rate. The corresponding values for the scheduled and unscheduled fountains are highlighted as red and blue dots respectively. (b) Discharge as a function of height for the scheduled (red curve) and the unscheduled (blue curve) fountain for a constant aperture diameter and pressure loss. (c) Discharge measured for the scheduled fountain (red curve) and estimated for the unscheduled fountain (blue curve) during the study period.

During fountain spray, the AIR surface (a) albedo dampens to ice albedo and (b) absorbs the heat energy of the fountain water droplets. These two processes are the cause of the difference in the mass and energy balance distribution shown in Table 3. The temporal variation of the magnitude of these processes are shown in Fig. 7.

210 The overall impact of the radiation fluxes (long-wave and short-wave) and the turbulent fluxes (sensible and latent) on the freezing and melting energies is determined from their respective energy turnover. The energy turnover is calculated as the sum of energy fluxes in absolute values (see Table 3).

There is a considerable difference in the contribution of the shortwave radiation due to the effect of process (a). Even though the unscheduled fountain was active for a much longer duration, the frequent snowfall events counteracted the albedo feedback 215 of its fountain discharge. However, the albedo of the automated AIR was significantly impacted by late fountain spray events particularly in the month of March and April as shown in Fig. 7.

Similarly, the fountain discharge heat flux for the traditional AIR was enhanced due to process (b). The higher discharge quantity of the unscheduled fountains and its longer duration were responsible for the 10 fold increase in its fountain discharge heat flux.

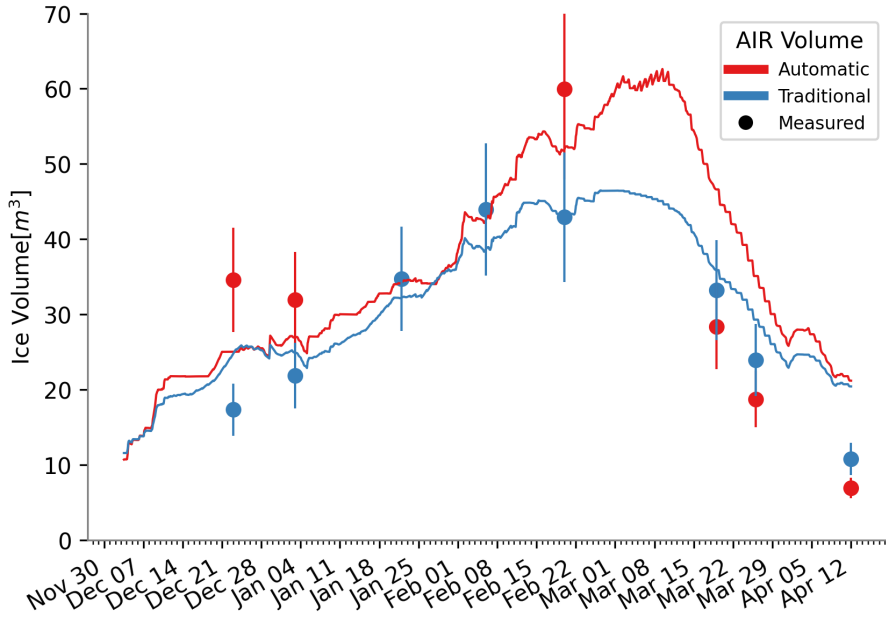


**Figure 6.** Volume validation of the scheduled and unscheduled fountain construction strategies.

## 220 5 Discussion

### 5.1 Benefits of scheduling fountains

The difference in water-use efficiency and maximum volume between unscheduled and scheduled fountains in the two locations across two winters are presented in Fig. 9. Four experimental values (highlighted by circles) are shown together with five simulated values (highlighted by squares). The experimental values were taken from the IN21 and CH21 AIRs studied in Balasubramanian et al. (2022) and the CH22 AIR presented in this study.

The water-use efficiency of all the unscheduled fountains are below 20 %. In general, the water-use efficiency increases more than two fold when the IVOM or WEOM fountain is used in both the locations.

There is also a considerable difference between the outputs of WEOM and IVOM fountains for each AIR. For CH21 AIR, WEOM fountain does not yield any ice formation whereas IVOM fountain succeeds in increasing the water-use efficiency three fold. For CH22 AIR, both experimental and simulated values of IVOM fountains yield an increase in water-use efficiency from 4 % to around 31 %. The WEOM fountain succeeded in increasing the water-use efficiency up to 2 times higher than the IVOM fountain.

For the Swiss location, scheduled fountains yield better water-use efficiency but do not alter the maximum volume obtained significantly.

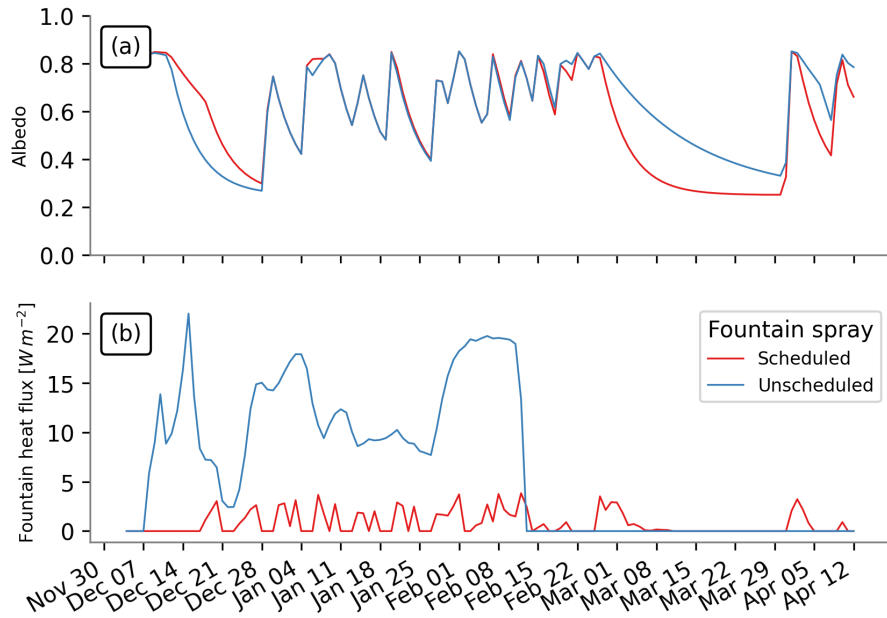


**Figure 7.** (a) Surface albedo and (b) fountain discharge heat flux showed significant variations between the two AIRS due to the differences in their discharge rates.

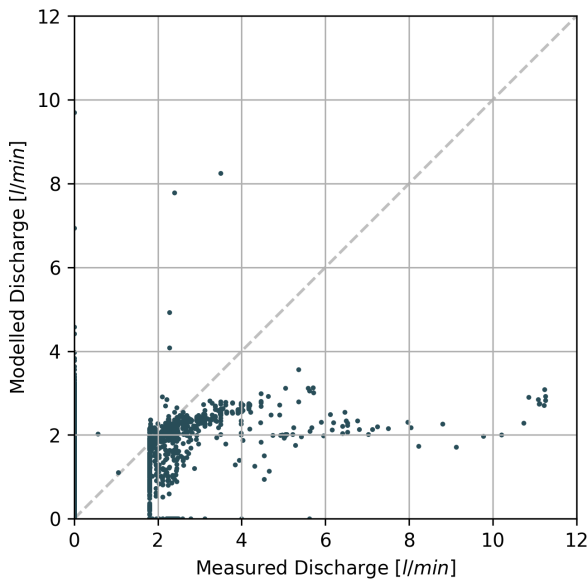


**Figure 8.** Comparison of the discharge rate measured by the automation system and the discharge rate simulated by the IVOM model.

**Table 3.** Summary of the mass balance, energy balance, fountain and AIR characteristics estimated at the end of the respective simulation duration for the automated and the traditional AIRs

	Name	Symbol	Traditional	Automated	Units
Input	Fountain discharge	$M_F$	$8.2 \times 10^5$	$1.4 \times 10^5$	kg
	Snowfall	$M_{ppt}$	$1.1 \times 10^4$	$1.5 \times 10^4$	kg
	Deposition	$M_{dep}$	$9.4 \times 10^2$	$1.2 \times 10^3$	kg
Output	Meltwater	$M_{water}$	$2.9 \times 10^4$	$4.2 \times 10^4$	kg
	Ice	$M_{ice}$	$1.3 \times 10^4$	$1.3 \times 10^4$	kg
	Sublimation	$M_{sub}$	$2.6 \times 10^3$	$3.0 \times 10^3$	kg
	Fountain wastewater	$M_{waste}$	$8.0 \times 10^5$	$1.1 \times 10^5$	kg
Energy Flux	Shortwave radiation	$q_{SW}$	29	39	%
	Longwave radiation	$q_{LW}$	35	34	%
	Sensible heat	$q_S$	8	8	%
	Latent heat	$q_L$	17	17	%
	Fountain discharge heat	$q_F$	10	1	%
	Rain heat	$q_R$	0	0	%
	Ground heat	$q_G$	1	2	%
Fountain	Spray Radius	$r$	4.8	4.1	m
	Aperture Diameter	$dia$	5	7	mm
	Pressure Loss	$P$	4.3	3.7	m
	Minimum discharge rate	$Q_{min}$	2	N.A.	l/min
AIR	Maximum AIR Volume		47	63	$m^3$
	Water Use Efficiency		4	31	%

235 For the Indian location, the two kinds of scheduled fountains yield significantly different results when compared to the unscheduled fountain. The IVOM fountain achieved a 1.5 fold increase in the maximum volume and a 2 fold increase in the water-use efficiency. The WEOM fountain had a water-use efficiency of 73 % but its maximum volume was lower than the unscheduled fountain.

The discharge duration and the max discharge rate of the three IN21 fountains were responsible for these different results  
240 (see Fig. 9 (b)). The max discharge rate of the unscheduled fountain was more than twice that of scheduled fountains resulting in a high water loss. Fountain freezing events caused frequent interruptions in the unscheduled discharge rate (see Fig. 9 (b)). Therefore, the discharge duration of the unscheduled fountain was much lower resulting in lower ice volumes. The WEOM fountain underestimated the freezing rate during the construction period and therefore produced much lower ice volumes compared to the IVOM fountain.

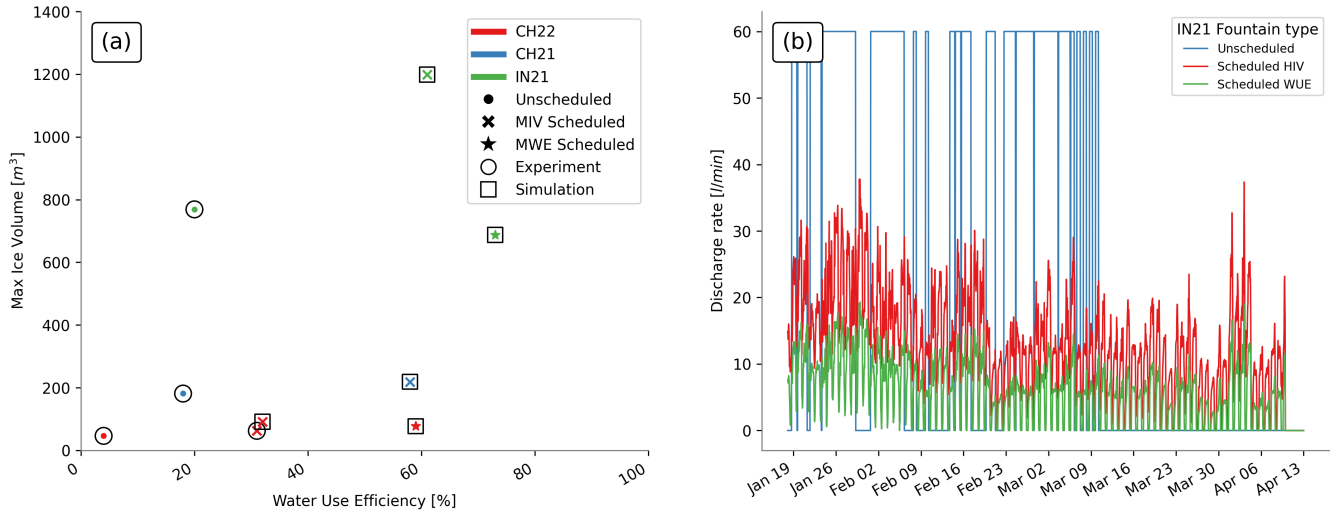


**Figure 9.** (a) The maximum volumes and water-use efficiency estimated for AIRs constructed in different locations (represented by colours) with different fountain scheduling strategies (represented by symbols). Experimental values are highlighted by circles and simulated values are highlighted by squares. (b) Comparison of the unscheduled and scheduled fountain's discharge rates at the IN21 location.

## 245 5.2 Challenges of scheduling fountains

### 5.2.1 Determination of minimum discharge rate

The value of minimum discharge rate determines the duration of the favourable weather windows and the risk of fountain freezing events. Therefore, its accurate quantification is critical. The risk of a fountain freezing event is inversely proportional to the spray radius. Therefore, minimum discharge rate can be determined based on the minimum fountain spray radius desired.

250 In the case of the CH22 experiment, the minimum discharge rate of  $2 l/min$  corresponded to a spray radius of around  $1 m$ .

### 5.2.2 Determination of fountain spray radius

To schedule fountains, one needs to estimate their spray radius accurately since the recommended discharge rate is proportional to the square of the spray radius used. Manual measurements of the fountain spray revealed a maximum spray radius of just 3 m but drone measurements reveal a fountain spray radius of 4.8 m for the scheduled fountain. This discrepancy could be 255 caused by both wind drift of water droplets and refreezing events across the boundary of the AIR.

## 6 Conclusions

In this paper, an automated AIR construction strategy is presented and compared with a traditional strategy using data collected in Guttannen, Switzerland and Gangles, India.

The main purpose of this study was to quantify the influence of different fountain designs and weather-sensitive scheduling strategies on the water use efficiency and volumes of AIRs exposed to identical weather conditions. We found that overwatering not just increased the fountain wastewater production but also enhanced the melting rate of AIRs, mainly due to its surface albedo and fountain heat flux feedbacks. Furthermore, the freezing rate of the scheduled fountain was also enhanced by its lower aperture diameter, which contributed to its higher spray radius. As a consequence, the automated AIR was able to reduce its water consumption by 87 % and increase its maximum volume by 34% compared to the traditional AIR.

265 Two different model forcings sensitive to the limited weather windows or water supply of a new location were used to produce two types of recommended discharge rates favouring higher volumes and better water use efficiencies, respectively. Nevertheless, these models were able to capture more than 44 % of the freezing rate variations produced by the full energy balance model. Simulations comparing scheduled and unscheduled fountains show that up to a two fold increase in water use efficiency is possible without compromising on meltwater production.

270 Fountain design is an important area where improvement is necessary since it can be used to increase AIR ice volumes. If the scheduled fountain of the CH22 experiment was replaced with a fountain with a lower pressure loss but with the same aperture diameter, the automated AIR would have produced more meltwater. Future research must be devoted to engineer such fountains that create larger AIRs effortlessly and efficiently.

#### Appendix A: Automation system

275 The automation hardware consists of an AWS, flowmeter, control valve, drain valves, air valves, fountain, pipeline and a logger. The logger feeds the AWS data to the automation software and informs the recommended discharge rate to the flowmeter. The flowmeter adjusts the control valve to match the recommendation. In case a termination criteria is valid, the drain and air valves allow the removal of water from the pipeline and entry of air in the pipeline respectively.

280 The recommended discharge rate is equal to the ice mass change rate. However, certain termination criteria override the discharge rate recommendation and drain the pipeline to prevent water loss or fountain freezing events, namely:

- High water loss is assumed if wind speed is greater than the user-defined critical wind speed.
- High risk of fountain freezing event is assumed if  $\frac{\Delta M_{ice}}{\Delta t}$  is lower than the user-defined minimum fountain discharge rate.
- Fountain freezing events are assumed if measured discharge rate is zero for at least 20 seconds and the pipeline is drained as a consequence.
- Pipeline leakage is assumed if measured discharge rate is greater than the user-defined maximum fountain discharge rate.

## Appendix B: Model updates

In the previous version of the model (Balasubramanian et al., 2022), the fountain water temperature ( $T_F$ ) was estimated as a constant parameter. However, in reality, this is a poor approximation. This is because the fountain water temperature and source water temperature differ due to the temperature change caused by transit from the source to the AIR surface. Therefore, we instead use measured hourly ground temperature measurements to approximate water temperature for both the AIRs.

In the previous version of the model (Balasubramanian et al., 2022), fountain discharge events were reset from surface albedo to ice albedo. However, this assumption limits the accuracy of the model, especially, for the automated AIR where several fountain discharge events of short durations occur. Therefore, we assumed that discharge events instead reduce the albedo decay rate ( $\tau$ ) by a factor of  $\frac{\alpha_{ice}}{\alpha_{snow}}$ .

Additionally, both the AIRs experienced many precipitation events. Therefore, it was no longer accurate to assume AIR density ( $\rho_{cone}$ ) to be equal to ice density. We instead parameterised AIR density  $\rho_{cone}$  as follows:

$$\rho_{cone} = \frac{M_F + M_{dep} + M_{ppt}}{(M_F + M_{dep})/\rho_{ice} + M_{ppt}/\rho_{snow}} \quad (B1)$$

where  $M_F$  is the cumulative mass of the fountain discharge;  $M_{ppt}$  is the cumulative precipitation;  $M_{dep}$  is the cumulative accumulation through water vapour deposition;  $\rho_{ice}$  is the ice density ( $917 \text{ kg m}^{-3}$ ) and  $\rho_{snow}$  is the density of wet snow ( $300 \text{ kg m}^{-3}$ ) taken from Cuffey and Paterson (2010).

Rain events were not considered in the previous version of the model but they occur in our experiment. The influence of rain events on the albedo and the energy balance was assumed to be similar to that of discharge events. However, the water temperature of a rain event was assumed to be equal to the air temperature. Accordingly, the heat flux generated due to a rain event was equal to:

$$q_R = \frac{\Delta M_{ppt} \cdot c_{water} \cdot T_a}{\Delta t \cdot A_{cone}} \quad (B2)$$

## Appendix C: Model forcing based on water-use efficiency and maximum volume objectives

The model complexity and data requirement (Balasubramanian et al., 2022) were reduced through assumptions that optimise for the ice volume or the water-use efficiency objectives. We define the freezing rate and melting rate as the positive and negative mass change rate, respectively. Assumptions are chosen, based on whether they overestimate/underestimate the freezing rate. HIV objective requires freezing rate to be overestimated whereas water-use efficiency objective requires freezing rate to be underestimated. We describe these two kinds of assumptions applied on each of the energy balance components below:

### C1 Surface Area $A_{cone}$ assumptions

Determination of the surface area during the accumulation period is achieved by assuming a constant ice cone radius equal to  
 315 the fountain spray radius. The surface area scales the freezing rate of the AIR. Hence, for the HIV objective, we assume the maximum possible slope of 1 for the ice cone or in other words  $h_{cone} = r_F$ . Therefore, area is estimated as:

$$A_{cone} = \sqrt{2} \cdot \pi \cdot r_F^2 \quad (C1)$$

Similarly, for the water-use efficiency objective, the area of the conical AIR is approximated to the area of its circular base. Therefore, area is estimated as:

$$320 \quad A_{cone} = \pi \cdot r_F^2 \quad (C2)$$

### C2 Net shortwave radiation $q_{SW}$ assumptions

The net shortwave radiation  $q_{SW}$  is computed as follows:

$$q_{SW} = (1 - \alpha) \cdot (SW_{direct} \cdot f_{cone} + SW_{diffuse}) \quad (C3)$$

where  $\alpha$  is the albedo value ;  $SW_{direct}$  is the direct shortwave radiation;  $SW_{diffuse}$  is the diffuse shortwave radiation and  
 325  $f_{cone}$  is the solar area fraction.

The data requirement was reduced by estimating the global shortwave radiation and pressure directly using the location's coordinates and altitude through the solar radiation model described in Holmgren et al. (2018). The algorithm used to estimate the clear-sky global radiation is described in Ineichen (2008).

The diffuse and direct shortwave radiation is determined using the estimated global solar radiation as follows:

$$SW_{diffuse} = cld \cdot SW_{global}$$

$$330 \quad SW_{direct} = (1 - cld) \cdot SW_{global} \quad (C4)$$

where  $cld$  is the cloudiness factor.  $cld$  is assumed to be 1 and 0 for the water-use efficiency and ice volume objective respectively.

We ignore the variations in the albedo and assume it to be equal to snow albedo and ice albedo for the ice volume and water-use efficiency objective, respectively.

335 The solar area fraction  $f_{cone}$  of the ice structure exposed to the direct shortwave radiation depends on the shape considered. It is computed as

$$f_{cone} = \frac{(0.5 \cdot r_{cone} \cdot h_{cone}) \cdot \cos\theta_{sun} + (\pi \cdot (r_{cone})^2 / 2) \cdot \sin\theta_{sun}}{\pi \cdot r_{cone} \cdot ((r_{cone})^2 + (h_{cone})^2)^{1/2}} \quad (C5)$$

For the ice volume objective, since we assume the slope of the cone to be 1,  $f_{cone}$  is determined as follows:

$$f_{cone} = \frac{\cos\theta_{sun} + \pi \cdot \sin\theta_{sun}}{2\sqrt{2} \cdot \pi} \quad (C6)$$

340 Similarly, for the water-use efficiency objective, since we assume the slope of the cone to be negligible, we get:

$$f_{cone} = \frac{\sin\theta_{sun}}{2} \quad (C7)$$

### C3 Net Longwave radiation $q_{LW}$ assumptions

We assume  $T_{ice} = 0^\circ C$  in order to determine outgoing longwave radiation. Since it is challenging to constrain the minimum ice temperature, we maintain this assumption for both our objectives. However, in order to estimate atmospheric emissivity, we  
345 again assume  $cld$  to be 1 and 0 for the water-use efficiency and ice volume objective respectively.

### C4 Turbulent fluxes assumptions

Turbulent fluxes estimation depend on the slope of the cone through the  $\mu_{cone}$  parameter. As suggested by Oerlemans et al. (2021), we estimated this parameter as follows:

$$\mu_{cone} = 1 + s_{cone}/2 \quad (C8)$$

350 Hence, the  $\mu_{cone}$  parameter takes values of 1.5 and 1 for the ice volume and water-use efficiency objective respectively. Since turbulent fluxes impact both the freezing and the melting rates, this assumption may not favor the corresponding objectives for certain sites.

**Table A1.** Free parameters in the model categorised as constant, model hyperparameters and weather parameters with their respective values/ranges.

Constant Parameters	Symbol	Value	Unit	References
Van Karman constant	$\kappa$	0.4	dimensionless	Cuffey and Paterson (2010)
Stefan Boltzmann constant	$\sigma$	$5.67 \times 10^{-8}$	$W m^{-2} K^{-4}$	Cuffey and Paterson (2010)
Air pressure at sea level	$p_{0,a}$	1013	$hPa$	Mölg and Hardy (2004)
Density of water	$\rho_w$	1000	$kg m^{-3}$	Cuffey and Paterson (2010)
Density of ice	$\rho_{ice}$	917	$kg m^{-3}$	Cuffey and Paterson (2010)
Density of air	$\rho_a$	1.29	$kg m^{-3}$	Mölg and Hardy (2004)
Specific heat of water	$c_w$	4186	$J kg^{-1} {}^\circ C^{-1}$	Cuffey and Paterson (2010)
Specific heat of ice	$c_{ice}$	2097	$J kg^{-1} {}^\circ C^{-1}$	Cuffey and Paterson (2010)
Specific heat of air	$c_a$	1010	$J kg^{-1} {}^\circ C^{-1}$	Mölg and Hardy (2004)
Thermal conductivity of ice	$k_{ice}$	2.123	$W m^{-1} K^{-1}$	Bonales et al. (2017)
Latent Heat of Sublimation	$L_s$	$2.848 \times 10^6$	$J kg^{-1}$	Cuffey and Paterson (2010)
Latent Heat of Fusion	$L_f$	$3.34 \times 10^5$	$J kg^{-1}$	Cuffey and Paterson (2010)
Gravitational acceleration	$g$	9.81	$m s^{-2}$	Cuffey and Paterson (2010)
Weather station height	$h_{AWS}$	2	$m$	assumed
Model timestep	$\Delta t$	3600	$s$	assumed
Model Hyperparameters	Symbol	Range	Unit	References
Surface layer thickness	$\Delta x$	$[1 \times 10^{-2}, 1 \times 10^{-1}]$	$m$	assumed
Weather Parameters	Symbol	Range	Unit	References
Ice Emissivity	$\epsilon_{ice}$	$[0.95, 0.99]$	dimensionless	Hori et al. (2006)
Surface Roughness	$z_0$	$[1 \times 10^{-3}, 5 \times 10^{-3}]$	$m$	Brock et al. (2006)
Ice Albedo	$\alpha_{ice}$	$[0.15, 0.35]$	dimensionless	Steiner et al. (2015); Zolles et al. (2019)
Snow Albedo	$\alpha_{snow}$	$[0.8, 0.9]$	dimensionless	Zolles et al. (2019)
Precipitation Temperature threshold	$T_{ppt}$	$[0, 2]$	${}^\circ C$	ShiChang et al. (2010)
Albedo Decay Rate	$\tau$	$[10, 22]$	$days$	Schmidt et al. (2017); Oerlemans and Knap (1998)

## References

- Aggarwal, A., Frey, H., McDowell, G., Drenkhan, F., Nüsser, M., Racoviteanu, A., and Hoelzle, M.: Adaptation to Climate Change Induced Water Stress in Major Glacierized Mountain Regions, *Climate and Development*, 0, 1–13, <https://doi.org/10.1080/17565529.2021.1971059>, 2021.
- Balasubramanian, S., Hoelzle, M., Lehning, M., Bolibar, J., Wangchuk, S., Oerlemans, J., and Keller, F.: Influence of Meteorological Conditions on Artificial Ice Reservoir (Icestupa) Evolution, *Frontiers in Earth Science*, 9, 771 342, <https://doi.org/10.3389/feart.2021.771342>, 2022.
- BBC News: Bright Artificial Glacier in Naryn - BBC Kyrgyz, <https://www.youtube.com/watch?v=TpeSQf75bFQ>, 2020.
- Bonales, L. J., Rodriguez, A. C., and Sanz, P. D.: Thermal Conductivity of Ice Prepared under Different Conditions, *International Journal of Food Properties*, 20, 610–619, <https://doi.org/10.1080/10942912.2017.1306551>, 2017.
- Brock, B. W., Willis, I. C., and Sharp, M. J.: Measurement and Parameterization of Aerodynamic Roughness Length Variations at Haut Glacier d'Arolla, Switzerland, *Journal of Glaciology*, 52, 281–297, <https://doi.org/10.3189/172756506781828746>, 2006.
- Clouse, C., Anderson, N., and Shippling, T.: Ladakh's Artificial Glaciers: Climate-Adaptive Design for Water Scarcity, *Climate and Development*, 9, 428–438, <https://doi.org/10.1080/17565529.2016.1167664>, 2017.
- Cuffey, K. M. and Paterson, W. S. B.: *The Physics Of Glaciers*, Elsevier, 2010.
- Farhan, S. B., Zhang, Y., Ma, Y., Guo, Y., and Ma, N.: Hydrological Regimes under the Conjunction of Westerly and Monsoon Climates: A Case Investigation in the Astore Basin, Northwestern Himalaya, *Climate Dynamics*, 44, 3015–3032, <https://doi.org/10.1007/s00382-014-2409-9>, 2015.
- Holmgren, W. F., Hansen, C. W., and Mikofski, M. A.: Pvlib Python: A Python Package for Modeling Solar Energy Systems, *Journal of Open Source Software*, 3, 884, <https://doi.org/10.21105/joss.00884>, 2018.
- Hori, M., Aoki, T., Tanikawa, T., Motoyoshi, H., Hachikubo, A., Sugiura, K., Yasunari, T. J., Eide, H., Storvold, R., Nakajima, Y., and Takahashi, F.: In-Situ Measured Spectral Directional Emissivity of Snow and Ice in the 8–14  $\mu\text{m}$  Atmospheric Window, *Remote Sensing of Environment*, 100, 486–502, <https://doi.org/10.1016/j.rse.2005.11.001>, 2006.
- Immerzeel, W. W., Lutz, A. F., Andrade, M., Bahl, A., Biemans, H., Bolch, T., Hyde, S., Brumby, S., Davies, B. J., Elmore, A. C., Emmer, A., Feng, M., Fernández, A., Haritashya, U., Kargel, J. S., Koppes, M., Kraaijenbrink, P. D. A., Kulkarni, A. V., Mayewski, P. A., Nepal, S., Pacheco, P., Painter, T. H., Pellicciotti, F., Rajaram, H., Rupper, S., Sinisalo, A., Shrestha, A. B., Viviroli, D., Wada, Y., Xiao, C., Yao, T., and Baillie, J. E. M.: Importance and Vulnerability of the World's Water Towers, *Nature*, 577, 364–369, <https://doi.org/10.1038/s41586-019-1822-y>, 2020.
- Ineichen, P.: A Broadband Simplified Version of the Solis Clear Sky Model, *Solar Energy*, 82, 758–762, <https://doi.org/10.1016/j.solener.2008.02.009>, 2008.
- IPCC: Chapter 2: High Mountain Areas — Special Report on the Ocean and Cryosphere in a Changing Climate, *IPCC Special Report on the Ocean and Cryosphere in a Changing Climate*, 2019.
- Meteoblue: Climate Guttannen, [https://www.meteoblue.com/en/weather/historyclimate/climatemodelled/guttannen\\_switzerland\\_2660433](https://www.meteoblue.com/en/weather/historyclimate/climatemodelled/guttannen_switzerland_2660433), 2021.
- Mölg, T. and Hardy, D. R.: Ablation and Associated Energy Balance of a Horizontal Glacier Surface on Kilimanjaro, *J. Geophys. Res.-Atmos.*, 109, 1–13, <https://doi.org/10.1029/2003JD004338>, 2004.

- Norphel, C. and Tashi, P.: Snow Water Harvesting in the Cold Desert in Ladakh: An Introduction to Artificial Glacier, in: Mountain Hazards and Disaster Risk Reduction, edited by Nibanupudi, H. K. and Shaw, R., Disaster Risk Reduction, pp. 199–210, Springer Japan, Tokyo, 390 https://doi.org/10.1007/978-4-431-55242-0\_11, 2015.
- Nüsser, M. and Baghel, R.: Local Knowledge and Global Concerns: Artificial Glaciers as a Focus of Environmental Knowledge and Development Interventions, in: Ethnic and Cultural Dimensions of Knowledge, edited by Meusburger, P., Freytag, T., and Suarsana, L., Knowledge and Space, pp. 191–209, Springer International Publishing, Cham, https://doi.org/10.1007/978-3-319-21900-4\_9, 2016.
- 395 Nüsser, M., Dame, J., Kraus, B., Baghel, R., and Schmidt, S.: Socio-Hydrology of Artificial Glaciers in Ladakh, India: Assessing Adaptive Strategies in a Changing Cryosphere, *Regional Environmental Change*, https://doi.org/10.1007/s10113-018-1372-0, 2019.
- Oerlemans, J. and Knap, W. H.: A 1 Year Record of Global Radiation and Albedo in the Ablation Zone of Morteratschgletscher, Switzerland, *Journal of Glaciology*, 44, 231–238, https://doi.org/10.3189/S002214300002574, 1998.
- Oerlemans, J., Balasubramanian, S., Clavuot, C., and Keller, F.: Brief Communication: Growth and Decay of an Ice Stupa in Alpine 400 Conditions – a Simple Model Driven by Energy-Flux Observations over a Glacier Surface, *The Cryosphere*, 15, 3007–3012, https://doi.org/10.5194/tc-15-3007-2021, 2021.
- Palmer, L.: Storing Frozen Water to Adapt to Climate Change, *Nature Climate Change*, 12, 115–117, https://doi.org/10.1038/s41558-021-01260-x, 2022.
- Reuters: Conservationists in Chile Aim to Freeze Water in Man-Made Glaciers, Reuters, 2021.
- 405 Schmidt, L. S., Aðalgeirsdóttir, G., Guðmundsson, S., Langen, P. L., Pálsson, F., Mottram, R., Gascoin, S., and Björnsson, H.: The Importance of Accurate Glacier Albedo for Estimates of Surface Mass Balance on Vatnajökull: Evaluating the Surface Energy Budget in a Regional Climate Model with Automatic Weather Station Observations, *The Cryosphere*, 11, 1665–1684, https://doi.org/10.5194/tc-11-1665-2017, 2017.
- ShiChang, TanGuang, G., ShiQiao, Z. G. Z., and Kang: Response of Zhadang Glacier Runoff in Nam Co Basin, Tibet, to Changes in Air 410 Temperature and Precipitation Form, *Chinese Science Bulletin*, 55, 2103–2110, https://doi.org/10.1007/s11434-010-3290-5, 2010.
- Steiner, J. F., Pellicciotti, F., Buri, P., Miles, E. S., W, T. D. I. W., and Reid: Modelling Ice-Cliff Backwasting on a Debris-Covered Glacier in the Nepalese Himalaya, *Journal of Glaciology*, 61, 889–907, https://doi.org/10.3189/2015JoG14J194, 2015.
- Tveiten, I.: Glacier Growing - A Local Response to Water Scarcity in Baltistan and Gilgit, Pakistan, Ph.D. thesis, 2007.
- Vince, G.: Glacier Man, *Science*, 326, 659–661, https://doi.org/10.1126/science.326\_659, 2009.
- 415 Vincent, S.: Energy and Climate Change in Cold Regions of Asia, 2009.
- Wangchuk, S.: Ice Stupa Competition, https://tribal.nic.in/IceStupa.aspx, 2020.
- Zolles, T., Maussion, F., Galos, S. P., Gurgiser, W., and Nicholson, L.: Robust Uncertainty Assessment of the Spatio-Temporal Transferability of Glacier Mass and Energy Balance Models, *The Cryosphere*, 13, 469–489, https://doi.org/10.5194/tc-13-469-2019, 2019.

# Symbols

$a$  distance m  
 $P$  power W ( $\text{Js}^{-1}$ )

$\omega$  angular frequency rads $^{-1}$

# List of Figures

1.1	Seasonal variation in the availability of irrigation water. The graph highlights the crucial role of AIRs in bridging the critical gap in water availability. Adapted from: [1] . . . . .	2
1.2	(a) Schematic overview of the position of artificial ice reservoirs. These constructions are located at altitudes between the glaciers and the irrigation networks in the cultivated areas. (b) Ice terraces at 3900 m, located above the village of Nang, Ladakh. The cascade is composed of a series of loose masonry walls ranging in height from 2 to 3 m, which help freeze water for storage. (c) Ice stupas at 3600 m, located above the village of Phyang, Ladakh. They are made using fountain systems. Adapted from: [1] . . . . .	3
3.1	The Swiss and Indian AIRs were 5 m and 13 m tall on January 9 and March 3, 2021 respectively. Picture credits: Daniel Buerki (left) and Thinles Norboo (right) . . . . .	9
3.2	Model schematic showing the workflow used in the model at every time step. . . . .	12
3.3	Shape variables of the AIR. $r_{cone}$ is the radius, $h_{cone}$ is the height, $j_{cone}$ is the thickness change and $s_{cone}$ is the slope of the ice cone. $r_F$ is the spray radius of the fountain. . . . .	14
3.4	. . . . .	24
4.1	AIRs show significant variation in volume evolution depending on the choice of construction location. . . . .	26
5.1	Adapted from: [11] . . . . .	29
5.2	The process of ice accumulation for ice terraces Adapted from: [11]	29
5.3	Ice terrace of Phuktse, viewpoint 4430 m. (a) February 2014 (b) October 2014 Adapted from: [11] . . . . .	30
5.4	The process of ice accumulation for ice stupas. Diagram by: Francesco Muzzi . . . . .	31
5.5	Ice terrace of Phuktse, viewpoint 4430 m. (a) February 2014 (b) October 2014 Adapted from: [11] . . . . .	32

# List of Tables

3.1	Summary of the weather observations for AIRs built during the 2020-21 winter season. The expiry date refers to the date when all of the ice of the AIR completely disappeared and only the dome volume remains. The weather measurements are shown using their mean ( $\mu$ ) and standard deviation ( $\sigma$ ) during the study period as $\mu \pm \sigma$ . . . . .	10
3.2	List of all the studied AIRs . . . . .	11
3.3	Assumptions for the parametrisation introduced to simplify the model. . . . .	22

# Abbreviations

<b>AIR</b>	Artificial Ice Reservoirs
<b>SIR</b>	Seasonal Ice Reservoirs
<b>PIR</b>	Perpetual Ice Reservoirs
<b>HIR</b>	Horizontal Ice Reservoirs
<b>VIR</b>	Vertical Ice Reservoirs

# Physical Constants

Speed of Light  $c = 2.997\ 924\ 58 \times 10^8\ \text{ms}^{-1}$  (exact)

## *Acknowledgements*

The acknowledgements and the people to thank go here, don't forget to include your project advisor...

# Bibliography

- [1] Marcus Nüsser and Ravi Baghel. Local Knowledge and Global Concerns: Artificial Glaciers as a Focus of Environmental Knowledge and Development Interventions. In Peter Meusburger, Tim Freytag, and Laura Suarsana, editors, *Ethnic and Cultural Dimensions of Knowledge*, Knowledge and Space, pages 191–209. Springer International Publishing, Cham, 2016. ISBN 978-3-319-21900-4. doi: 10.1007/978-3-319-21900-4\_9.
- [2] W. W. Immerzeel, A. F. Lutz, M. Andrade, A. Bahl, H. Biemans, T. Bolch, S. Hyde, S. Brumby, B. J. Davies, A. C. Elmore, A. Emmer, M. Feng, A. Fernández, U. Haritashya, J. S. Kargel, M. Koppes, P. D. A. Kraaijenbrink, A. V. Kulkarni, P. A. Mayewski, S. Nepal, P. Pacheco, T. H. Painter, F. Pellicciotti, H. Rajaram, S. Rupper, A. Sinisalo, A. B. Shrestha, D. Vivioli, Y. Wada, C. Xiao, T. Yao, and J. E. M. Baillie. Importance and vulnerability of the world’s water towers. *Nature*, 577(7790):364–369, January 2020. ISSN 1476-4687. doi: 10.1038/s41586-019-1822-y.
- [3] Suhaib Bin Farhan, Yinsheng Zhang, Yingzhao Ma, Yanhong Guo, and Ning Ma. Hydrological regimes under the conjunction of westerly and monsoon climates: A case investigation in the Astore Basin, Northwestern Himalaya. *Climate Dynamics*, 44(11):3015–3032, June 2015. ISSN 1432-0894. doi: 10.1007/s00382-014-2409-9.
- [4] Ingvar Tveiten. *Glacier Growing - A Local Response to Water Scarcity in Baltistan and Gilgit, Pakistan*. PhD thesis, 2007.
- [5] Chewang Norphel and Padma Tashi. Snow Water Harvesting in the Cold Desert in Ladakh: An Introduction to Artificial Glacier. In Hari Krishna

- Nibanupudi and Rajib Shaw, editors, *Mountain Hazards and Disaster Risk Reduction*, Disaster Risk Reduction, pages 199–210. Springer Japan, Tokyo, 2015. ISBN 978-4-431-55242-0. doi: 10.1007/978-4-431-55242-0\_11.
- [6] Biswajit Mukhopadhyay and Asif Khan. A reevaluation of the snowmelt and glacial melt in river flows within Upper Indus Basin and its significance in a changing climate. *Journal of Hydrology*, 527:119–132, August 2015. ISSN 0022-1694. doi: 10.1016/j.jhydrol.2015.04.045.
- [7] Stauffer Vincent. *Energy and Climate Change in Cold Regions of Asia*. August 2009.
- [8] IPCC. Chapter 2: High Mountain Areas — Special Report on the Ocean and Cryosphere in a Changing Climate. *IPCC Special Report on the Ocean and Cryosphere in a Changing Climate*, 2019.
- [9] Gaia Vince. Glacier Man. *Science*, 326(5953):659–661, October 2009. doi: 10.1126/science.326\_659.
- [10] Carey Clouse, Naomi Anderson, and Taylor Shippling. Ladakh’s artificial glaciers: Climate-adaptive design for water scarcity. *Climate and Development*, 9(5):428–438, 2017. doi: 10.1080/17565529.2016.1167664.
- [11] M. Nüsser, Juliane Dame, Benjamin Kraus, Ravi Baghel, and Susanne Schmidt. Socio-hydrology of artificial glaciers in Ladakh, India: Assessing adaptive strategies in a changing cryosphere. *Regional Environmental Change*, 2019. doi: 10.1007/s10113-018-1372-0.
- [12] Sonam Wangchuk. Ice Stupa Competition. <https://tribal.nic.in/IceStupa.aspx>, December 2020.
- [13] Lisa Palmer. Storing frozen water to adapt to climate change. *Nature Climate Change*, 12(2):115–117, February 2022. ISSN 1758-6798. doi: 10.1038/s41558-021-01260-x.
- [14] Anubha Aggarwal, Holger Frey, Graham McDowell, Fabian Drenkhan, Marcus Nüsser, Adina Racoviteanu, and Martin Hoelzle. Adaptation to climate

- change induced water stress in major glacierized mountain regions. *Climate and Development*, 0(0):1–13, September 2021. ISSN 1756-5529. doi: 10.1080/17565529.2021.1971059.
- [15] BBC News. Bright artificial glacier in Naryn - BBC Kyrgyz. <https://www.youtube.com/watch?v=TpeSQf75bFQ>, February 2020.
- [16] Reuters. Conservationists in Chile aim to freeze water in man-made glaciers. *Reuters*, October 2021.
- [17] Pallava Bagla. Artificial Glaciers to Help Farmers. *Science*, 282(5389):619–619, October 1998. doi: 10.1126/science.282.5389.619a.
- [18] Meteoblue. Climate Guttannen. <https://www.meteoblue.com/en/weather/historyclimate/climate-guttannen>, February 2021.
- [19] Marcus Nüsser, Susanne Schmidt, and Juliane Dame. Irrigation and Development in the Upper Indus Basin: Characteristics and Recent Changes of a Socio-hydrological System in Central Ladakh, India. *Mountain Research and Development*, 32(1):51–61, 2012. doi: 10.1659/MRD-JOURNAL-D-11-00091.1.
- [20] Suryanarayanan Balasubramanian, Martin Hoelzle, Michael Lehning, Jordi Bolíbar, Sonam Wangchuk, Johannes Oerlemans, and Felix Keller. Influence of Meteorological Conditions on Artificial Ice Reservoir (Icestupa) Evolution. *Frontiers in Earth Science*, 9:771342, February 2022. ISSN 2296-6463. doi: 10.3389/feart.2021.771342.
- [21] Kurt M. Cuffey and W. S. B. Paterson. *The Physics Of Glaciers*. Elsevier, 2010.
- [22] J. Oerlemans and W. H. Knap. A 1 year record of global radiation and albedo in the ablation zone of Morteratschgletscher, Switzerland. *Journal of Glaciology*, 44(147):231–238, 1998. doi: 10.3189/S0022143000002574.
- [23] Harold M. Woolf. *On the Computation of Solar Elevation Angles and the Determination of Sunrise and Sunset Times*. National Aeronautics and Space Administration, 1968.

- [24] W. Brutsaert. *Evaporation into the Atmosphere. Theory, History and Application.* Kluwer Academic Publishers, 1982.
- [25] W. Brutsaert. On a derivable formula for long-wave radiation from clear skies. *Water Resources Research*, 11(1-4):742–744, 1975. doi: 10.1029/WR011i005p00742.
- [26] J. R. Garratt. *The Atmospheric Boundary Layer.* Cambridge University Press, 1992.
- [27] Jianhua Huang. A Simple Accurate Formula for Calculating Saturation Vapor Pressure of Water and Ice. *AMETSOC*, 57, June 2018. doi: 10.1175/JAMC-D-17-0334.1.
- [28] J. Oerlemans, S. Balasubramanian, C. Clavuot, and F. Keller. Brief communication: Growth and decay of an ice stupa in alpine conditions – a simple model driven by energy-flux observations over a glacier surface. *The Cryosphere*, 15 (6):3007–3012, 2021. doi: 10.5194/tc-15-3007-2021.
- [29] Tobias Sauter, Anselm Arndt, and Christoph Schneider. COSIPY v1.3 – an open-source coupled snowpack and ice surface energy and mass balance model. *Geoscientific Model Development*, 13(11):5645–5662, November 2020. doi: 10.5194/GMD-13-5645-2020.
- [30] Chewang Norphel. Artificial glacier: A high altitude cold desert water conservation technique. (Energy and Climate Change in cold regions of Asia: Proceedings of the Seminar, Ladakh, India):62–64, 2009.
- [31] D. Grossman. As Himalayan Glaciers Melt, Two Towns Face the Fallout. [https://e360.yale.edu/features/as\\_himalayan\\_glaciers\\_melt\\_two\\_towns\\_face\\_the\\_fallout](https://e360.yale.edu/features/as_himalayan_glaciers_melt_two_towns_face_the_fallout), 2015.